NOVEL TECHNIQUES REGARDING SPECIFIC ABSORPTION RATE AND FIELD OF VIEW REDUCTION IN MAGNETIC RESONANCE IMAGING

A DISSERTATION SUBMITTED TO
THE DEPARTMENT OF ELECTRICAL AND ELECTRONICS ENGINEERING
AND THE GRADUATE SCHOOL OF ENGINEERING AND SCIENCE
OF BILKENT UNIVERSITY
IN PARTIAL FULFILLMENT OF THE REQUIREMENTS
FOR THE DEGREE OF
DOCTOR OF PHILOSOPHY

By
Emre Kopanoglu
September, 2012

I certify that I have read this thesis and that in my opinion it is fully adequate, in scope and in quality, as a dissertation for the degree of Doctor of Philosophy.

Prof. Dr. Ergin Atalar(Supervisor)

I certify that I have read this thesis and that in my opinion it is fully adequate, in scope and in quality, as a dissertation for the degree of Doctor of Philosophy.

Assoc. Prof. Dr. Vakur B. Ertürk(Co-supervisor)

I certify that I have read this thesis and that in my opinion it is fully adequate, in scope and in quality, as a dissertation for the degree of Doctor of Philosophy.

Prof. Dr. Yusuf Ziya İder

I certify that I have read this thesis and that in my opinion it is fully adequate, in scope and in quality, as a dissertation for the degree of Doctor of Philosophy.

Prof. Dr. Levent Gürel

I certify that I have read this thesis and that in my opinion it is fully adequate, in scope and in quality, as a dissertation for the degree of Doctor of Philosophy.

Prof. Dr. Murat Eyüboğlu

I certify that I have read this thesis and that in my opinion it is fully adequate, in scope and in quality, as a dissertation for the degree of Doctor of Philosophy.

Prof. Dr. Cengizhan Öztürk

Approved for the Graduate School of Engineering and Science:

Prof. Dr. Levent Onural
Director of the Graduate School

ABSTRACT

NOVEL TECHNIQUES REGARDING SPECIFIC ABSORPTION RATE AND FIELD OF VIEW REDUCTION IN MAGNETIC RESONANCE IMAGING

Emre Kopanoglu
Ph.D. in Electrical and Electronics Engineering
Supervisors: Prof. Dr. Ergin Atalar
Assoc. Prof. Dr. Vakur B. Ertürk

September, 2012

In this dissertation, novel strategies regarding the reduction of the specific absorption rate (SAR) and the reduction of the total scan time, and analytic calculation methods for the lower limit on the specific absorption rate and the upper limit on the signal-to-noise ratio (SNR) are proposed. The first contribution of this dissertation is on the ultimate intrinsic signal-to-noise ratio (UISNR) and the ultimate intrinsic specific absorption rate (UISAR). Analytic expressions that are valid for arbitrarily shaped subjects are derived for these two parameters at the quasi-static limit. By comparing the UISNR expression to a previously published semi-analytic method for a cylindrical subject, it is shown that the maximum error is below 10%. In the primary contribution of this dissertation, gradient fields with nonlinear variation in space are used for radio-frequency (RF) excitation pulse design. When such fields are used for a pulse design, the relation between the excitation profile and the RF pulse is altered, which leads to a different RF envelope and hence, a different SAR value. Using simulations and experiments, SAR reductions between 15% - 54% are demonstrated, in three case studies. Another topic of this dissertation is on the reduction of the total scan time using nonlinear gradient fields. It is demonstrated that, when nonlinear gradient fields are used for excitation, the excitation region can be focused along more than a single direction. Furthermore, with a careful selection of readout encoding direction, reduced field-of-view imaging can be made without changing the SAR or the echo time. In a volunteer experiment, 60% reduction in the total scan time is obtained. The last topic of this dissertation is on curved slice imaging. It is shown using simulations that RF encoding can be used for imaging a curved field-of-view with non-rectangular and nonuniform voxels that may conform to

the region-of-interest better. It is proposed that when the method is used with multi-dimensional excitation pulses, curved regions may be imaged in a shorter time.

Keywords: nonlinear gradient fields, high-order gradient fields, ultimate intrinsic, signal to noise ratio, specific absorption rate, reduced FOV imaging, radio-frequency (RF) encoding.

ÖZET

MANYETİK REZONANSLA GÖRÜNTÜLEMEDE ÖZGÜL SOĞURUM HIZINI DÜŞÜRMEK VE GÖRÜNTÜLEME ALANINI KÜÇÜLTMEK İÇİN YENİ YÖNTEMLER

Emre Kopanoglu
Elektrik ve Elektronik Mühendisligi Bölümü, Doktora
Tez Yöneticileri: Prof. Dr. Ergin Atalar
Assoc. Prof. Dr. Vakur B. Ertürk

Eylül, 2012

Bu tezde, özgül soğurum hızının düşürülmesi ve toplam görüntüleme zamanının azaltılması için kullanılabilecek yeni yöntemler ile en yüksek sinyal-gürültü oranını (SGO) ve en düşük özgül soğurum hızını (ÖSH) bulmak için kullanılabilecek analitik denklemler önerilmiştir. Bu tezin katkılarından ilki, nihai içsel sinyal gürültü oranı (NİSGO) ve nihai içsel özgül soğurum hızı (NİÖSH) üzerinedir. Bu iki değişken için, yarı-durağan sistemlerde herhangi bir şekle sahip cisimlerde kullanılabilecek analitik denklemler türetilmiştir. Elde edilen NİSGO denklemi, silindirik bir cisim için daha önce yayınlanmış yarı analitik bir metodla kıyaslanarak, denklemdeki hatanın %10'dan az olduğu gösterilmiştir. Bu tezin birincil katkısı ise, doğrusal olmayan gradyan manyetik alanların (DOGMA) radyo-frekansı uyarım dalgaları tasarlarken kullanılmasıdır. Bu tür manyetik alanlar uyarım dalgası tasarımında kullanıldığında, uyarı profili ile uyarım dalgası arasındaki bağıntı değişmekte; bu değişim farklı bir uyarım dalgası ve buna bağlı olarak farklı bir ÖSH değeri elde edilmesine olanak sağlamaktadır. Yapılan bilgisayar benzetimleri ve deneyler ile, %15 ile %54 arasında değişen ÖSH azaltımları gösterilmiştir. Bu tezdeki bir başka çalışma konusu, DOGMA kullanılarak toplam görüntüleme zamanının kısaltılması üzerinedir. DOGMA kullanıldığında, uyarı profilinin birden fazla yönde birden odaklanabildiği gösterilmiştir. Buna ek olarak, frekans kodlama yönünün uyumlu seçimi ile, ÖSH'yi ya da yankı zamanını arttırmadan düşük görüş alanlı görüntüleme yapılabileceği kanıtlanmıştır. Yapılan gönüllü deneyinde, önerilen teknik kullanılarak görüntüleme zamanı %60 düşürülmüştür. Bu tezin son konusu ise, eğimli kesitlerin görüntülenmesi üzerinedir. Bilgisayar benzetimleri ile, radyo-frekansı kodlaması kullanılarak

eğimli görüş alanlarının, ilgi alanına daha uyumlu olan eğimli ve birbirinden farklı vokseller kullanılarak görüntülenebileceği gösterilmiştir. Bu tekniğin çok boyutlu uyarı dalgaları ile birleştirilerek eğimli bölgeleri daha kısa zamanda görüntülemek için kullanılabileceği önerilmiştir.

Anahtar sözcükler: doğrusal olmayan gradyan manyetik alanlar, yüksek dereceli gradyan manyetik alanlar, nihai içsel, sinyal gürültü oranı, özgül soğurum hızı, küçültülmüş görüntüleme alanı, radyo-frekansında kodlama teknikleri.

Acknowledgement

Although a dissertation reflects the name of a single person on the cover, the journey towards the dissertation lasts several years and includes lots of people; family, friends, colleagues and mentors. Therefore I would like to thank everybody who has stuck by me along this journey.

I would like to express my deepest to **Prof. Ergin Atalar**. He has been a remarkable mentor; he has shown me great patience and support and his guidance has been invaluable. His vast knowledge on science and his never-ending passion for research has inspired me deeply. It has been a great pleasure to work with him and I am greatly indebted to him for introducing me to the field that I am passionate about.

I would also like to thank **Assoc. Prof. Vakur B. Ertürk**. He has made electromagnetics enjoyable and has always been a great mentor. I owe him profoundly for his humanity and all the wisdom he has shared with me that extends well beyond my Ph.D. studies.

I want to thank my jury members, whose comments have increased the scientific quality of my dissertation; **Prof. Yusuf Ziya İder** for always being there whenever I needed advice throughout my undergraduate and graduate studies; **Prof. Murat Eyüboğlu** for all his comments on my work throughout my graduate studies; **Prof. Cengizhan Öztürk** and **Prof. Levent Gürel** for reading and commenting on this dissertation. I also want to thank **Prof. Ayhan Altıntaş** for sharing his immense knowledge on electromagnetics through various discussions. All their comments have been invaluable and deeply appreciated.

I want to acknowledge The Scientific and Technological Research Council of Turkey (TUBİTAK) for supporting the work done in this dissertation.

I would like to thank my friends **Elif Aydoğdu**, **Can Kerse**, and *Darth* **Niyazi Şenlik** and especially **Can Uran**, who can *always look on the bright side of life*. I would like to express my gratitude to **Yiğitcan Eryaman** and **Haydar**

Çelik for sharing their valuable experiences on being a Ph.D. candidate, **Volkan Açıkel** for helping me scientifically even only by listening, **Esra Abacı Türk**, **Taner Demir**, **Uğur Yılmaz**, **Burak Akın**, and **Yıldıray Gökhalk** for all the scientific collaborations and last but not the least, **Aydan Ercingöz** for all the small talk and listening to my gibber jabber, and **Mürüvet Parlakay** for all her help throughout my years at Bilkent. I also want to thank my friends from **UMRAM** and **Bilkent University** as well. *May the force be with you.*

I want to thank my family **Hale** and **Cevat Kopanoğlu** and **Orçun**, **Duygu**, **Serap** and **Orhan Açıkgöz** and my grandfather **Ethem Erköse** for their unconditional love and never ending support. You have always treated me with understanding and indulgence, and managed to cheer me up even at my most distressed moments. This dissertation would not be possible without you or my dear wife **Teksin Açıkgöz Kopanoğlu**, to whom I am the most grateful for all the things that would take much longer than this dissertation to tell. You have always made me aim for the best and have shared all the burden. You are the best thing in my life and you have made me as happy as a little kid can be ever since I met you.

I have been blessed with the valuable love, support and friendship of many people, and even though I have limited the list here to the people that have affected my work and to my immediate family, I am also thankful to my other family members and friends for all the good times.

Teksin'ime. . .

Contents

List of Figures

List of Tables

Chapter 1

Introduction

Magnetic resonance imaging (MRI) is one of the most widely used imaging modalities for both clinical and research purposes. The popularity of MRI arises from its superior soft tissue contrast and its non-ionizing radiation. However, MRI experiments last longer than alternatives such as computed tomography. Furthermore, an inevitable side effect is radio-frequency power absorption in the subject, which leads to tissue heating. In order to keep the heating at a minimum level, strict limitations are imposed on imaging approaches, which may increase the imaging time further. In MRI, the goal is to obtain the best image in the shortest duration possible, with minimum tissue heating. Therefore, this dissertation introduces novel techniques towards several goals: reduction of power absorption in the body of interest; reduction of total imaging time; and finding the upper limit on image quality and the lower limit on power absorption.

The first contribution of this dissertation is finding an analytic expression on the maximum image quality. In MRI, the image quality is quantified using the signal-to-noise ratio. However, the signal-to-noise ratio depends on many factors including the subject, the location of the region-of-interest inside the subject, the coil used for imaging, the static magnetic field strength and the imaging parameters. In order to evaluate coil performance and uncover any room for improvement in the coil design, the intrinsic SNR (ISNR) was defined by removing the imaging parameter-dependent components [2]. As a final step towards

setting a benchmark for coil performance evaluation, the ISNR of the coil that is ideal for imaging the region-of-interest inside the subject was obtained in [3], and referred to as the ultimate-ISNR (UISNR). Although many studies exist that provide semi-analytic UISNR expressions [3–13], analytic solutions exist only for semi-infinite planar [14], spherical [15] and cylindrical samples [16, 17]; the former expressions need to be computationally implemented, and the latter are valid for only specific sample shapes. Therefore, there is no method in the literature that provides intuitive information (i.e., shows explicitly the dependence of UISNR on the sample parameters and other variables) about the UISNR for an arbitrarily shaped sample. Hence, in this study, such an expression is derived that explicitly shows the dependence of UISNR on the aforementioned variables; the expression is valid for homogeneous samples at the quasi-static limit. The proposed expression is compared to a previously published semi-analytic method for a cylindrical sample.

In a similar manner to the derivation of the analytic expression on UISNR, the lower limit on the power absorption in the subject is also studied in this dissertation. One of the main safety parameters in MRI regulations is the specific absorption rate [18, 19]. When an excitation RF pulse in the form of a magnetic field is applied to the subject, an undesired and inevitable side effect is the exposure of the subject to the electric field of the transmission RF coil as well. Because subjects are usually conductive for in-vivo experiments, the electric field of the coil causes RF power absorption inside the subject. The ratio of this power to the mass of the absorbing tissue is related to heating in the tissue, which is approximated in the Bioheat equation [20]. Therefore, minimization of this ratio, which is referred to as the specific absorption rate (SAR), is fundamental in decreasing the adverse effects on patients. Recently, a relative measure of the lowest possible SAR was defined in [21], and referred to as the ultimate intrinsic specific absorption rate (UISAR). Similarly, the optimum SAR distribution for a given flip-angle distribution was investigated in [22]. However, these two studies used semi-analytic methods to calculate the UISAR. Therefore, similar to the UISNR case, the explicit dependence of UISAR on the geometrical and electromagnetic properties of the subject, which could provide intuitive information about the

variation of UISAR with these parameters, has not been shown previously. Furthermore, the intrinsic SAR, which is a measure of coil performance in terms of SAR, has not been defined. Therefore, ISAR is defined and an analytic expression on UISAR that explicitly demonstrates how UISAR changes with aforementioned parameters is obtained. The UISAR expression is obtained for arbitrarily shaped homogeneous samples, at the quasi-static regime, similar to the UISNR case.

The second contribution of this dissertation is on reduction of the specific absorption rate using nonlinear gradient fields. In MRI, gradient fields are used during excitation in order to localize the excitation to a specific region. The shape of this region is related to the RF excitation pulse through the gradient fields. In conventional excitation methods, linear gradient fields are employed and well-known RF pulse design algorithms exist [23, 24]. The SAR is generally not a limiting factor at low field strengths, and therefore, it is not a key parameter in pulse design at such field strengths. However, the SAR restrictions imposed on imaging sequences become more severe with the increasing field strength because of the quadratic dependence of the SAR on the field strength. Furthermore, the homogeneity of the RF field inside the sample degrades with the increasing field strength, due to wavelength effects. Even though this inhomogeneity can be mitigated through the use of multiple transmit coils [25] or multi-dimensional RF excitation pulses, [26–30], such methods increase the SAR further. The SAR depends on the RF pulse envelope and the field distribution of the RF coil, whereas the excitation profile depends not only on these two elements of excitation, but also on the temporal and the spatial variation of the gradient field as well. Hence, the variable rate selective excitation (VERSE) algorithm, which alters the RF pulse envelope by modifying the temporal dependence of the gradient field has become the benchmark in SAR reduction [31]. However, the effect of altering the spatial variations of the gradient fields on the RF pulse design algorithms and hence, on SAR, has not been investigated. In this dissertation, it is shown that by using nonlinear gradient fields, significant SAR reductions can be obtained. The proposed method is compared and combined with the VERSE approach as well.

The third topic of this dissertation is on using nonlinear gradient fields for

reducing the total scan time in MRI. With the conventional approach of using a linear gradient field to localize the excitation region, the localization takes place along only one direction, and hence, the excitation region is bounded in the transverse plane by the extent of the subject. However, the region-of-interest (ROI) is much smaller than the whole cross-section of the subject for many applications. In order to reduce the imaging volume with the goal of reducing the total scan time, various approaches have been used to reduce the field-of-view (FOV) or the excitation region. When the FOV is smaller than the excitation region, aliasing artifacts occur, and corrupt the image. Although RF coils with spatially varying sensitivities can be used to image a specific region, coil sensitivities vary smoothly in space. Therefore, this approach is generally inefficient unless the ROI is close to the surface. Alternatively, refocusing, saturation, or multi-dimensional excitation pulses [32, 33] have been widely used for localizing the excitation. However, such pulses increase the SAR, and in certain cases, the echo time. Instead of using additional RF pulses, nonlinear gradient fields have been demonstrated to localize the excitation region [34–36], or to reduce the FOV by dephasing the spins in the outer volumes [37]. However, the latter method also suffers from increased echo-time due to the extra gradient signal applied after excitation, and for the former method, the extent of the excitation region is reduced only in the transverse plane [34], unless it is combined with refocusing pulses [35, 36]. In this dissertation, the effect of nonlinear gradient fields on the aliasing artifacts is investigated. It is demonstrated that, with proper selection of encoding and FOV-reduction directions, artifacts can be eliminated by band-pass filtering at the post-processing stage. With the proposed approach, the total scan time can be reduced without any additional RF or gradient pulses and therefore, the SAR and the echo time can be kept unaltered. The method is demonstrated using volunteer experiments.

The final topic of this dissertation is on imaging curved regions using nonuniform and non-rectangular voxels, in order to reduce the total scan time. Similar to excitation, encoding is also performed using linear gradient fields in conventional MRI methods. In this case, the voxels are identical and rectangular. Furthermore, the FOV has to be a rectangular region that encloses the ROI. However, the

(ROI) is non-rectangular for various MRI applications. It has been shown that, nonuniform and non-rectangular voxels can be obtained using nonlinear gradient fields [38–42] or RF encoding [43, 44]. With such approaches, not only the voxels conform to the ROI much better, but also the FOV can be non-rectangular, fitting closely to the ROI. Because the outer regions are not imaged in this case, reductions in the total scan time may be obtained, when nonlinear gradient fields or RF encoding techniques are used instead of linear gradient fields. In MRI, the wavelength at the operation frequency of RF fields is much smaller compared to that at the operation frequency of gradient fields. Therefore, more rapid spatial variations can be obtained using RF fields. Hence, RF encoding is studied in this dissertation as a means for obtaining non-rectangular and nonuniform voxels to image curved regions. The method is combined with multi-dimensional excitation pulses [33] in order to localize the excitation region to the ROI. The method is demonstrated using simulations.

The chapter-by-chapter structure of the dissertation is as follows. In the second chapter of this dissertation, the derivations on ultimate intrinsic specific absorption rate and ultimate specific absorption rate are given. The third chapter presents the SAR reduction method that employs nonlinear gradient fields for RF pulse design. In chapter 4, the field-of-view reduction method that employs nonlinear gradient fields for excitation is summarized. Finally, Chapter 5 studies the RF encoding method for the purpose of curved slice imaging.

Chapter 2

Signal-to-Noise Ratio and Specific Absorption Rate

Preface

The content of this chapter was presented in part at the Scientific Meetings of International Society of Magnetic Resonance in Medicine [45] and European Society of Magnetic Resonance in Medicine and Biology [46] and it was published in Magnetic Resonance in Medicine [47]. The text and the figures of this chapter are based on the journal publication [47].

2.1 Introduction

In MRI, increasing signal-to-noise ratio (SNR) improves the quality of acquired images, resulting in an easier diagnosis. Therefore, numerous studies have been conducted to maximize SNR in the form of understanding the main noise sources in MRI experiments and minimizing their contributions. The main noise sources in an MRI experiment can be classified as the preamplifier, the coil and the sample [48]. Preamplifier noise is small when ultra-low-noise amplifiers (ULNA)

are utilized [49]. Coil noise is also small in most applications [2]. Although it becomes dominant when low-field imaging and/or small coils are used, its effect can be minimized using superconductor or low temperature wires [50–52]. Consequently, in the majority of MRI applications, sample noise becomes the dominant factor in the determination of the SNR of images.

Because the SNR of images depends on many factors, it may not serve as a good measure of coil performance. As an alternative, intrinsic SNR (ISNR) has been defined by removing the imaging parameter-dependent components and making it dependent only on the coil structure and the geometric and electromagnetic properties of the sample of interest. Therefore, the lowest upper bound on ISNR, which is called ultimate-ISNR (UISNR) [3], provides a solid reference for coil performance evaluations.

On the other hand, minimization of the specific absorption rate (SAR) is fundamental in decreasing the adverse effects on patients, and similar to UISNR, a relative measure of the lowest possible SAR, the ultimate intrinsic SAR (UISAR) is defined [21]. Furthermore, UISNR and UISAR are related due to two reasons: first, the transmission field and receiver sensitivity of a coil are related through the reciprocity principle [53, 54]; second, the absorbed power in the sample that is used for SAR calculations is a function of the same loss mechanism that is responsible for the thermal noise in the UISNR calculations. This topic will be explained in more detail in the following section.

The semi-analytic and analytic methods (the former methods require computational implementation whereas for the latter, such an implementation is not needed) in the literature for the calculation of UISNR and UISAR are limited to semi-infinite planar, spherical and cylindrical sample geometries [3]-[21], [4]-[17]. The main reason behind this limitation is the lack of appropriate basis functions that are used to express the electromagnetic field inside a sample. It is known that the choice of basis functions affects the computation time and the numerical error [4, 21]. The use of basis functions whose functional form resemble the exact field decreases the necessary number of modes and, hence, the computation time.

However, such basis functions are hard to find when the sample shape is arbitrary. Nevertheless, plane waves and cylindrical and spherical harmonics can still be employed for arbitrary geometries. However the required number of modes and consequently the computation time increase significantly for such basis functions. Furthermore, these methods will be more prone to error (which will be referred to in Section 2.8). Thus, finding an appropriate set of basis functions for an arbitrary geometry is difficult.

Throughout the years, numerous studies have been conducted in the literature about UISNR and UISAR. Ocali et al. concentrated on elliptical cylinders [3], whereas, in other work, the sample geometry was a cylinder with a circular cross section [5]. A cylindrical geometry was also investigated by Vesselle [6]. Ohliger et al. adapted the UISNR theory to parallel imaging to investigate the effect of acceleration for an elliptical cylindrical sample [7]. Wiesinger et al. studied a spherical geometry [8, 9] when parallel MRI was used and showed that UISNR could be approached using loop coils [9]. Coil performance maps, which measure the performance of actual coil arrays with respect to UISNR, were shown in [4] for the case of a cylindrical sample with a circular cross section for parallel MRI. Schnell et al. investigated the performance of various practical geometries for infinite half-space and cylinder cases [10]. UISNR was investigated for spherical and cylindrical geometries [11]-[13]. UISAR was recently studied by Lattanzi et al. in [21]. Optimum SAR distribution for a given flip-angle distribution was found [22]. All of these studies used semi-analytic methods to calculate UISNR and UISAR. In the obtained expressions, various mathematical functions such as Bessel functions or operations such as integrations or matrix multiplications exist. As the static magnetic field strength and sample-related parameters are used as arguments of these functions and operations, the effect of these parameters on UISNR and UISAR is not explicit in these studies.

On the other hand, there are analytic studies in the literature that show explicitly the dependence of UISNR and UISAR on sample-related parameters and the static magnetic field strength. In analytic studies, Hoult and Lauterbur obtained the SNR limits for a spherical geometry [15], and Wang et al. and Reykowski found the ultimate SNR limits of circular and square loop coils when the sample

was a dielectric half-space [14] or a dielectric cylinder [16, 17], respectively. However, all of these studies (analytic and semi-analytic) were restricted to spherical, cylindrical and semi-infinite planar samples only. As a result, there is no method in the literature that provides intuitive information (i.e., shows explicitly the dependence of UISNR and UISAR on the sample parameters and other variables) about the UISNR and UISAR for an arbitrarily shaped sample.

Motivated by this, we present analytic expressions to approximate UISNR and UISAR values for arbitrary sample geometries. To derive the analytic expressions, we define a shape and a size factor that are specific to the MRI experiment. The shape factor depends on the coil configuration, the shape of the sample and the relative position of the point of interest in the sample. However, it is independent of sample parameters, including the size, permittivity, permeability, conductivity, temperature, nucleus of interest and the static magnetic field strength. The shape factor can be calculated either using numerical methods, or CAD tools, or analytic methods. The expressions for UISNR and UISAR are derived by finding the maximum value of the shape factor, which is for the optimal coil configuration. Our expressions explicitly show how UISNR and UISAR depend on the main magnetic field and on the sample-related parameters mentioned above. It is also shown that UISNR and UISAR are independent of the permeability of the sample. These expressions are valid when the distance between the coil and the point of interest (POI) is smaller than the wavelength, which is referred to as the quasi-static limit throughout the dissertation. As a practical case and a solution example, UISNR and UISAR expressions are presented for a uniform and electrically small sample in the shape of a circular cylinder. Using this example solution, it is shown that the error is below 1%, 10% and 25%, when the coil-POI distance is smaller than one-tenth, one-fifth and one-third of the wavelength, respectively.

2.2 Theory

In this section, rotating magnetic field, rotating frame, flip-angle and absorbed power definitions will be presented. Then, these expressions will be employed in the SNR and SAR calculations.

2.2.1 Rotating Magnetic field

2.2.1.1 Phasor Domain

Assuming that the static magnetic field is along the z-axis, a general expression for the transverse magnetic field is

$$\overline{\mathbf{H}}(t) = \hat{x}\sqrt{2}\,|H_x|\cos(\omega_0 t - \psi_x) + \hat{y}\sqrt{2}\,|H_y|\cos(\omega_0 t - \psi_y) \tag{2.1}$$

where $H_x = |H_x|\,e^{-i\psi_x}$ and $H_y = |H_y|\,e^{-i\psi_y}$ are the root-mean-squared (rms) phasors of the magnetic field components along the x- and y-axes, respectively, with $|H_x|$ and $|H_y|$ being the magnitudes and ψ_x and ψ_y being the phases of the x- and y-components. Note that the hat symbol denotes a unit vector. With respect to the z-axis, this magnetic field can be separated into its left-hand and right-hand rotating components. During an RF magnetic field transmission, the right-hand-polarized component does not affect the spins, and only the left-hand component is of interest, which can be written as the following:

$$\overline{\mathbf{H}}^{\mathrm{t}}_{\mathrm{f}}(t) = |H_x|\frac{\hat{x}\cos(\omega_0 t - \psi_x) - \hat{y}\sin(\omega_0 t - \psi_x)}{\sqrt{2}} \tag{2.2}$$

$$+|H_y|\frac{\hat{y}\cos(\omega_0 t - \psi_y) + \hat{x}\sin(\omega_0 t - \psi_y)}{\sqrt{2}} \tag{2.3}$$

where the subscript $_{\mathrm{f}}$ and the superscript $^{\mathrm{t}}$ denote forward and transmission, respectively, meaning that this field excites the spins when used in transmission mode [55]. This magnetic field is widely referred to as the B_1^+-field ($B_1^+ = \mu H^{\mathrm{t}}_{\mathrm{f}}$) in the literature as well [28–30]. It should be noted that, throughout this dissertation, the operating frequency is ω_0, which is the Larmor frequency, and is related to the static magnetic field strength, B_0, via $\omega_0 = \gamma B_0$ where γ is

the gyromagnetic ratio. In the phasor domain, the vector for the rms forward-polarized magnetic field can be written as $\mathbf{H}_{\mathrm{f}}^{\mathrm{t}} = \hat{a}_{\mathrm{f}}^{\mathrm{t}} H_{\mathrm{f}}^{\mathrm{t}}$ where $\hat{a}_{\mathrm{f}}^{\mathrm{t}} = (\hat{x} + j\hat{y})/\sqrt{2}$ is the forward-polarized unit vector [56], and the peak scalar forward-polarized transmission field $H_{\mathrm{f}}^{\mathrm{t}}$ is given by $H_{\mathrm{f}}^{\mathrm{t}} = H_x - jH_y$. The rms field is given by the following:

$$H_{\mathrm{f}}^{\mathrm{t}} = \frac{H_x - jH_y}{\sqrt{2}} = \frac{H_\rho - jH_\phi}{\sqrt{2}}\, e^{-j\phi} \tag{2.4}$$

In Eq. (2.4), H_ρ and H_ϕ are the magnetic field components along ρ- and ϕ-axes of the cylindrical coordinate system, which are related to the Cartesian coordinate counterparts by $H_\rho = H_x \cos(\phi) + H_y \sin(\phi)$ and $H_\phi = -H_x \sin(\phi) + H_y \cos(\phi)$. Similarly, the right-hand-polarized magnetic field during transmission is denoted by $H_{\mathrm{r}}^{\mathrm{t}}$ where the subscript $_{\mathrm{r}}$ denotes reverse-polarization. The reverse-polarized rms magnetic field and the associated unit vector are given by the following equation:

$$H_{\mathrm{r}}^{\mathrm{t}} = \frac{H_x + jH_y}{\sqrt{2}} = \frac{H_\rho + jH_\phi}{\sqrt{2}}\, e^{+j\phi}$$

and $\hat{a}_{\mathrm{r}}^{\mathrm{t}} = (\hat{x} - j\hat{y})/\sqrt{2}$. However, in signal reception, the forward-polarized unit vector is given by $\hat{a}_{\mathrm{f}}^{\mathrm{r}} = [\hat{x}\cos(\omega_0 t) + \hat{y}\sin(\omega_0 t)]/\sqrt{2}$ for correct signal demodulation. Hence, in the phasor domain, the forward- and reverse-polarized unit vectors for reception are given by $\hat{a}_{\mathrm{f}}^{\mathrm{r}} = (\hat{x} - j\hat{y})/\sqrt{2}$ and $\hat{a}_{\mathrm{r}}^{\mathrm{r}} = (\hat{x} + j\hat{y})/\sqrt{2}$. Therefore, the corresponding field expressions become the following:

$$\begin{aligned} H_{\mathrm{f}}^{\mathrm{r}} &= \frac{H_x + jH_y}{\sqrt{2}} = \frac{H_\rho + jH_\phi}{\sqrt{2}} e^{+j\phi} \\ H_{\mathrm{r}}^{\mathrm{r}} &= \frac{H_x - jH_y}{\sqrt{2}} = \frac{H_\rho - jH_\phi}{\sqrt{2}} e^{-j\phi}. \end{aligned} \tag{2.5}$$

2.2.1.2 Rotating Frame

In order to simplify the analysis of excitation in MRI, rotating frame is commonly used. Note that, the formulation in the previous section is for the phasor domain. However, the envelope of the RF pulses play an important role in excitation. Therefore, in this section, the time-dependence of the RF envelope will be incorporated into the magnetic field expressions as well.

Letting $g(t)$ represent the envelopes of the transmitted RF signal, the transmitted forward-polarized magnetic field can be expressed as the following:

$$\begin{aligned}\overline{\mathbf{H}}_{\mathrm{f}}^{\mathrm{t}}(t) &= |H_x|g(t)\frac{\hat{x}\cos(\omega_0 t-\psi_x)-\hat{y}\sin(\omega_0 t-\psi_x)}{\sqrt{2}} \\ &\quad +|H_y|g(t)\frac{\hat{y}\cos(\omega_0 t-\psi_y)+\hat{x}\sin(\omega_0 t-\psi_y)}{\sqrt{2}} \end{aligned} \tag{2.6}$$

It is common practice to call the x-axis the real axis, and the y-axis the imaginary axis, as suggested by the Argand diagram. Then by letting $t = 0$ to transform the lab frame to the rotating frame, the magnetic field in the rotating frame can be expressed as follows:

$$\begin{aligned}{}_{\mathrm{rot}}\overline{H}_{\mathrm{f}}^{\mathrm{t}}(t) &= \frac{|H_x|\,e^{i\psi_x}+j\,|H_y|\,e^{i\psi_y}}{\sqrt{2}}g(t) && (2.7)\\ &= \frac{H_x^*+jH_y^*}{\sqrt{2}}g(t) && (2.8)\\ &= \left(H_{\mathrm{f}}^{\mathrm{t}}\right)^* g(t) && (2.9)\end{aligned}$$

In MRI, the spins rotate around a magnetic field, obeying the left hand rule. Therefore, when the projection of the vector magnetic field onto the Argand diagram is obtained, the resulting expression is the complex conjugate of the projection of the same field onto the left-hand rotating unit-vector in the phasor domain.

2.2.2 Flip Angle and Absorbed Power

When a radio-frequency magnetic field is transmitted to the body of interest, the spins are rotated around the applied magnetic field. The angular rotation of the spins with respect to the longitudinal axis, z, is called the flip-angle, or equivalently, the tip-angle.

Using the definitions given in [48] and the magnetic field expression in the rotating frame given in Eq. (2.9), the flip-angle can be defined in terms of the phasor domain rms magnetic field as Eq. (2.10):

$$\alpha(\mathbf{x},t) = \gamma\mu|H_{\mathrm{f}}^{\mathrm{t}}|\int_{\tau} g(t)\,\mathrm{d}t \tag{2.10}$$

where $\mathbf{x} = [x \;\; y \;\; z]$ is the three-dimensional position vector, μ is the permeability and τ is the duration of the RF pulse.

When a medium with finite conductivity is exposed to electromagnetic fields, it absorbs power from the fields. For a linear medium with conductivity σ, the instantaneous absorbed power can be expressed as [57]:

$$\begin{aligned} P(t) &= \sigma \int_V \left|\mathbf{E}\left(\mathbf{x}\right) g(t)\right|^2 \, \mathrm{d}v & (2.11)\\ &= \sigma \int_V \left|\mathbf{E}\left(\mathbf{x}\right)\right|^2 \, \mathrm{d}v \;\; |g(t)|^2 & (2.12)\\ &= P \;\; |g(t)|^2 \, . & (2.13) \end{aligned}$$

where $\mathbf{E}\left(\mathbf{x}\right)$ is the RF electric field. Note that, the absorbed power given in Eq. (2.13) scales quadratically with the strength of the electromagnetic fields. Therefore, it is useful to define "normalized absorbed power" for SNR and SAR analysis. Let us assume that at an arbitrary position $\mathbf{x}_0$, the magnetic field strength is $H_{\mathrm{f}}^{\mathrm{r}}(\mathbf{x}_0)$. Then, the power required to generate 1 A/m magnetic field strength is:

$$\frac{1}{\xi_0^2} \;\; \triangleq \;\; \frac{1}{\left|H_{\mathrm{f}}^{\mathrm{r}}(\mathbf{x}_0)\right|^2} \, \sigma \int_V \left|\mathbf{E}\left(\mathbf{x}\right)\right|^2 \, \mathrm{d}v \;\; |g(t)|^2 \, . \qquad (2.14)$$

where $\xi_0 = \xi(\mathbf{x}_0)$ and ξ is the magnetic field generated per square-root of total absorbed power (will be referred to as "field-per-square-root-power").

Note that, the power definition given in Eq. (2.13) is the instantaneous power. In MRI, RF pulses are repeated with a repetition-time denoted by T_R. Therefore, in order to compare the absorbed power with the safety regulations given in [18, 19], time-averaged power, which is averaged over one repetition-time T_R, is defined as follows:

$$\begin{aligned} P^{\mathrm{av}} &= \frac{1}{T_R} \int_0^{T_R} \iiint_V \sigma \left|\mathbf{E}\left(\mathbf{x}\right) g(t)\right|^2 \, \mathrm{d}v \, \mathrm{d}t & (2.15)\\ &= \frac{1}{T_R} \; P \; \int_0^{T_R} |g(t)|^2 \, \mathrm{d}t. & (2.16) \end{aligned}$$

2.2.2.1 Normalized Pulses

It should be kept in mind that the duration of the RF pulses can be much shorter than T_R. By changing the duration of the RF pulse and adjusting the gradient waveforms and the RF pulse amplitude accordingly, the power can be altered while keeping the flip-angle and T_R unchanged. In order to demonstrate the relation between the duration and amplitude of the RF pulse, normalized pulses will now be defined. Let us assume that the total duration of the RF pulse envelope, $g(t)$, is $\tau \leq T_R$. Then, the normalized RF pulse $g_n(s)$ can be defined as follows:

$$g_n(s) \triangleq \frac{1}{\tau} g\left(\frac{t}{\tau}\right), \tag{2.17}$$

in which case, the time-averaged absorbed power can be reformulated as:

$$P^{\text{av}} = \frac{1}{\tau\ T_R}\ P\ \int_0^1 |g_n(s)|^2\ \mathrm{d}s. \tag{2.18}$$

Note that, s is the normalized time, and is unitless. By incorporating Eqs. (2.10) - (2.14) in to Eq. (2.18), the total absorbed power in order to obtain a flip-angle $\alpha_0 = \alpha(\mathbf{x}_0)$ at $\mathbf{x}_0$ can be obtained as follows:

$$P^{\text{av}} = \frac{1}{\tau\ T_R}\ \frac{1}{\xi_0^2}\ |H_{\text{f}}^{\text{r}}(\mathbf{x}_0)|^2\ \int_0^1 |g_n(s)|^2\ \mathrm{d}s \tag{2.19}$$

$$= \frac{1}{\tau\ T_R}\ \frac{1}{\xi_0^2}\ \left|\frac{\alpha_0}{\gamma\mu \int_0^1 g_n(s)\,\mathrm{d}s}\right|^2\ \int_0^1 |g_n(s)|^2\ \mathrm{d}s \tag{2.20}$$

$$= \frac{1}{(\gamma\mu\xi)^2}\ \frac{\int_0^1 |g_n(s)|^2\ \mathrm{d}s}{\left|\int_0^1 g_n(s)\,\mathrm{d}s\right|^2}\ \frac{\alpha^2}{\tau\ T_R} \tag{2.21}$$

$$= \frac{1}{(\gamma\mu\xi)^2}\ e_{\text{RF}}\ \frac{\alpha^2}{\tau\ T_R}. \tag{2.22}$$

Note that, the location of the point $\mathbf{x}_0$ can be altered without changing Eq. (2.22). Therefore, in arriving at Eq. (2.22), $\alpha_0/\xi_0 = \alpha(\mathbf{x})/\xi(\mathbf{x}) = \alpha/\xi$ is used, and e_{RF} is defined as:

$$e_{\text{RF}} \triangleq \frac{\int_0^1 |g_n(s)|^2\ \mathrm{d}s}{\left|\int_0^1 g_n(s)\,\mathrm{d}s\right|^2} \tag{2.23}$$

In Eq. (2.22), the dependence of the absorbed power on the imaging parameters $\left(\alpha^2/\left(\tau T_R\right)\right)$ and the RF pulse shape (e_{RF}) is separated from the parameters that depend on the coil, the field strength and the subject $\left(1/\left(\gamma\mu\xi\right)^2\right)$. Note that, e_{RF} is the normalized energy of the RF pulse shape, and is unitless since s is unitless. Minimum of e_{RF} is one, and it holds for the rectangular pulse.

Note that, although the RF pulse envelope is normalized to unit duration, its amplitude depends on the flip-angle. Because the flip-angle is an experiment dependent variable, the RF envelope can be normalized to unit flip-angle, or unit integral, for demonstration purposes. In this dissertation, the RF pulses will be normalized to unit integral as follows:

$$g_{n1}(s) \triangleq \frac{1}{\tau}\frac{g\left(\frac{t}{\tau}\right)}{\int_0^\tau g\left(t'\right)\,\mathrm{d}t'}, \tag{2.24}$$

It should be noted that the normalized energy of the RF pulse and the SAR formulation remain unaltered in either case.

In the following sections, the definitions given for flip-angle and absorbed power will be used for deriving the signal-to-noise ratio and specific absorption rate expressions.

2.3 Signal-to-Noise Ratio

The SNR of an image is defined point-by-point in [2, 3] as the following:

$$\mathrm{SNR} = \Psi\Upsilon \tag{2.25}$$

where

$$\Upsilon = \frac{\mathcal{V}\sqrt{N_x N_y N_{\mathrm{rep}}}}{\sqrt{F2BW}} w(T_1, T_2, T_2^*, \alpha) \tag{2.26}$$

and

$$\Psi = \frac{\sqrt{2}\omega_0\mu M_0}{\sqrt{4k_{\mathrm{B}}TP}}\left|H_{\mathrm{f}}^{\mathrm{r}}\right|. \tag{2.27}$$

In Eq. (2.26), Υ contains the imaging parameters, where F is the overall system noise figure (in terms of power), $\mathcal{V}$ is the voxel volume in cubic meters, N_{rep} is the number of image repetitions, N_x is the number of readout points, N_y is the number of phase encoding steps, BW is the baseband receiver bandwidth and the weight function $w(T_1, T_2, T_2^*, \alpha)$ contains the effects of the flip-angle α and the relaxation time constants T_1, T_2, and T_2^* (please refer to [48] for detailed explanations). In Eq. (2.27), Ψ is the ISNR of the coil at hand [2, 3, 5], where M_0 is the magnetization density per voxel after an RF pulse with a flip-angle of 90°, k_{B} is the Boltzmann constant and T is the sample temperature. Finally, H_{f}^{r} and P are the forward-polarized received magnetic field and the total noise power, respectively, where both are in root-mean-squared (rms) units. It should be kept in mind that for SNR calculations, the magnitude of the received forward-polarized magnetic field, defined in Section 2.2.1.1, is used. Note that ISNR is defined point-by-point, and the ISNR of a POI at $\mathbf{x}_0$ is independent of the imaging parameters. The static magnetic field B_0 is assumed to be along the z-axis without loss of generality. Although the noise generated by the imaged subject is due to the thermal energy of the body which is independent of the receive coil, the noise that is reflected onto the images depends on how much the thermal energy is picked up by the coil. The sensitivity of the receive coil to thermal energy depends on its electric field distribution $\left(\mathbf{E}\left(\mathbf{x}\right)\right)$ when it is used in transmit mode. Therefore, P can be defined as the power absorbed by the sample, when the coil is used as a transmit coil in order to generate H_{f}^{r} at point $\mathbf{x}_0$. Then, using the field-per-square-root-power definition given in Section 2.2.2, ISNR can be expressed as:

$$\Psi = \frac{\sqrt{2}\omega_0 \mu M_0}{\sqrt{4k_{\text{B}}T}} \xi(\mathbf{x}_0). \tag{2.28}$$

2.4 Specific Absorption Rate

SAR is defined as the ratio of the power absorbed by the sample to the mass of the sample. Regulatory limits are defined for 1-gram, 10-gram and whole-body-averaged and organ-averaged absorbed power for the head, torso and extremities

[18, 19]. Note that, the power absorbed by the subject when the receive coil is employed as a transmit coil, is used for SNR analysis in Section 2.3. Hence, a similar analysis can be conducted for SAR. However, there are two fundamental differences that should be taken into account, although these two differences do not prevent a relation between SAR and SNR. First, the transmitted pulse may have a time dependent envelope. Second, the received forward-polarized magnetic field is used for SNR calculations, whereas the transmitted forward-polarized magnetic field should be used for SAR. However, it is well known that a coil's forward transmission field is equal to its forward reception field when the direction of the static magnetic field is flipped from the positive to the negative z-direction. Hence, the mirrored version of a transmission coil with respect to the z-axis is a receiver coil. As a result, the forward transmission magnetic field can be replaced by the forward reception magnetic field without any inconvenience. Neglecting the field transients, the transmitted RF pulse (in the rotating frame, denoted by $_{\mathrm{rot}}$) and the electric field can be expressed by the following equations:

$$
\begin{aligned}
{}_{\mathrm{rot}}\overline{H}_{\mathrm{f}}^{\mathrm{t}}\left(\mathbf{x},t\right) &= \left[H_{\mathrm{f}}^{\mathrm{t}}\left(\mathbf{x}\right)\right]^{*} g(t) && (2.29)\\
\overline{\mathbf{E}}\left(\mathbf{x},t\right) &= \mathbf{E}\left(\mathbf{x}\right) g(t) && (2.30)
\end{aligned}
$$

Note that the envelope function is assumed to generate a small bandwidth when compared to the Larmor frequency. Using Eq. (2.22), SAR can be expressed as:

$$
\begin{aligned}
\mathrm{SAR} &= \frac{P^{av}}{m_{sample}} && (2.31)\\
&= \frac{1}{\left(\gamma\mu\xi\right)^{2}\ m_{sample}}\ e_{\mathrm{RF}}\ \frac{\alpha^{2}}{\tau\ T_{R}} && (2.32)
\end{aligned}
$$

The SAR can be separated into two parts, the one that contains the imaging parameters and the one that is independent of the imaging parameters, which is the Intrinsic SAR:

$$
\mathrm{SAR} = \mathrm{ISAR}\ \ \Phi \tag{2.33}
$$

where

$$
\Phi = e_{\mathrm{RF}}\frac{\alpha^{2}}{\tau T_{R}} \tag{2.34}
$$

and

$$\text{ISAR} \triangleq \frac{1}{\xi^2 \gamma^2 \mu^2 m_{\text{sample}}}. \tag{2.35}$$

The physical interpretation of the ISAR definition given by Eq. (2.35) is as follows: The envelope of the transmitted signal and the flip-angle are imaging parameters that affect the SAR. ISAR, on the other hand, is the total absorbed power per total sample mass for unit flip-angle at a specific position $\mathbf{x}_0$ when the integral of the RF envelope and its square are equal to one. Hence, it is independent of the imaging parameters α, T_R, τ and e_{RF}. Note that, ISAR is dependent on the position $\mathbf{x}_0$ because unit flip-angle is assumed at $\mathbf{x}_0$. Because the location of the unit flip-angle is known, SAR and ultimate-SAR can be calculated from ISAR and UISAR, respectively. Although, choosing an alternative unit flip-angle position scales the ISAR and UISAR; values of SAR and ultimate-SAR do not change. Similar to the ISNR, ISAR depends on the coil and the sample. Therefore, it can be used for comparing coil performances.

Although the concept of ultimate-ISAR was previously studied in [21], a proportional expression was given for UISAR instead of an exact formulation. Hence, this is the first time ISAR is defined.

2.5 Quasi-Static Limit

In this dissertation, the "quasi-static limit" means that, the distance, r_s, between the source and observation points is electrically small (i.e., with respect to the wavelength, λ) such that the phase and amplitude variations of the electromagnetic field due to the wavelength and the conductivity are negligible along this distance. This condition corresponds to $|kr_s| \ll 1$ (i.e., $r_s \ll 1/|k|$), where $k = \omega_0\sqrt{\mu\epsilon}\sqrt{1 - j\ tan\delta}$ is the complex wavenumber, $tan\delta = \sigma/(\omega_0\epsilon)$ is the loss tangent, and ϵ, μ and σ are the permittivity, permeability, and conductivity of the sample, respectively.

A collection of two opposite charges that lie close to each other in space is called an electric dipole, whereas a small loop coil is called a magnetic dipole [58],

and they are the most basic radiating elements in electromagnetics. Hence, any current distribution can be expressed as a collection of either electric or magnetic dipoles, or both. When their field expressions are used without any simplifications, an electric dipole can be replaced by a group of magnetic dipoles, and vice versa [10]. However, in the quasi-static limit, the expressions can be simplified by retaining only the terms that contribute the most, which then requires the utilization of both types of dipoles to form a complete set of basis functions. Note that in the quasi-static limit, the electric and magnetic fields of an electric dipole vary with $1/r_s^3$ and $1/r_s^2$, whereas the variations are $1/r_s^2$ and $1/r_s^3$, respectively, for the magnetic dipole. Because the magnetic field affects the source signal and the electric field contributes to noise in MRI, the ratio of $|H/E|$ should be maximized for maximum SNR. At the quasi-static limit, $|H/E|$ varies with r_s for electric dipoles and with $1/r_s$ for magnetic dipoles and, therefore, approaches 0 for the former and ∞ for the latter as the sample size becomes smaller. As a consequence, magnetic dipoles are the meaningful choice of radiating elements (without any need for electric dipoles). Furthermore, it was previously shown for spherical and semi-infinite planar subjects that magnetic dipoles can be employed to approach UISNR [8, 14]. Hence, magnetic dipoles will be used as coil elements for UISNR and UISAR calculations in the following sections.

A special case that should be considered here is when the sample size is comparable to the wavelength but the distance between the POI and the surface is much smaller than the wavelength. In such a case, it is well known that the optimum coil structure will be a group of coils that are as close to the POI as possible. Due to two reasons, namely, the decay of the field of magnetic dipoles with the distance and the conductivity of the sample, the RF power will decay to negligible levels away from the POI into the sample. This decay distance will be in or close to the quasi-static regime. Hence, this behavior renders our formulation that will follow to be valid for this special case. This argument will be supported with simulation results in the Results section.

2.5.1 Electromagnetic Field Expressions at the Quasi-Static Limit

The forward-polarized received magnetic field and the electric field inside a homogeneous sample, generated by a group of small loop coils (magnetic dipoles) that are on the boundary of the sample, can be expressed at the quasi-static limit:

$$H_{\mathrm{f}}^{\mathrm{r}}(\mathbf{x}) = \sum_{m} \frac{a^2}{r_m^3} I_m f_m^{\mathrm{h}}(\theta,\phi)\, e^{-jkr_m} \tag{2.36}$$

$$\mathbf{E}(\mathbf{x}) = \sum_{m} \omega_0 \mu \frac{a^2}{r_m^2} I_m \left[\hat{x} f_m^{\mathrm{x}}(\theta,\phi) + \hat{y} f_m^{\mathrm{y}}(\theta,\phi) + \hat{z} f_m^{\mathrm{z}}(\theta,\phi)\right] e^{-jkr_m} \tag{2.37}$$

where the field expressions of a single loop coil are taken from [58]. In Eqs. (2.36) - (2.37), a is the radii of the loop coils, m is the loop coil index, r_m is the distance between the m^{th} loop's center and the POI, and I_m is the current passing through the m^{th} coil. In Eqs. (2.36)-(2.37), $f_m^{\mathrm{h}}(\theta,\phi)$, $f_m^{\mathrm{x}}(\theta,\phi)$, $f_m^{\mathrm{y}}(\theta,\phi)$ and $f_m^{\mathrm{z}}(\theta,\phi)$ are functions of the spherical variables, θ and ϕ. These functions, which represent the angular weights due to the position of the POI as well as the location and orientation of the m^{th} coil, are not given here because this is a general solution, and exact forms of such functions require well-defined geometries. It should be kept in mind that any electromagnetic field distribution should satisfy the boundary conditions. For our formulation, as the sources lay on the surface of the sample, the boundary conditions are satisfied through the sources. Although putting coils on the surface of the sample is not feasible, equivalent sources that are away from the sample can be found anytime using the Equivalence Principle [58]. Because $kr_m \ll 1$ in the quasi-static limit, the exponential terms e^{-jkr_m} can be neglected.

The instantaneous total absorbed power $\big($Eq. (2.13)$\big)$ can be expressed in the quasi-static limit as:

$$P = \sigma \omega_0^2 \mu^2 a^4 r^{-1} p \tag{2.38}$$

where

$$p = \sum_{i=\{x,y,z\}} \int_V \left(\sum_m I_m f_m^i (\theta, \phi) \right)^* \left(\sum_n I_n f_n^i (\theta, \phi) \right) \times \frac{1}{(r_m/r)^2 (r_n/r)^2} \frac{\mathrm{d}v}{r^3} \tag{2.39}$$

and the symbol * denotes the complex conjugate. Note that in Eq. (2.39), all coil-to-POI distance terms (r_n and r_m) are normalized with r. Here r is the size factor of the sample and can be chosen as a fundamental dimension of the sample. For example, if the sample is a cylinder, r may represent its radius; if the sample is a cube, then r may represent the length of one of its edges. As the coil-to-POI distance terms (r_n and r_m) are also dependent on the size of the sample, r_m/r and r_n/r are normalized distances. Hence, the integral is over the volume of the unit-sized object that has the same shape as the sample, and as a result, the parameter p has units of current squared and is independent of the sample size. Then, the magnetic field-per-square-root-power $\big($Eq. (2.14)$\big)$ becomes:

$$\xi = \frac{1}{\omega_0 \mu \sqrt{\sigma r^{-1}}} \frac{1}{\sqrt{p}} \sum_m I_m r^{-3} \frac{1}{(r_m/r)^3} f_m^{\mathrm{h}} (\theta, \phi) . \tag{2.40}$$

$$= \mathcal{S} \frac{1}{\omega_0 \mu \sqrt{\sigma}} \, r^{-2.5} \tag{2.41}$$

where

$$\mathcal{S} = \frac{1}{\sqrt{p}} \sum_m I_m \frac{1}{(r_m/r)^3} f_m^{\mathrm{h}} (\theta, \phi) \tag{2.42}$$

is a unitless function that depends on the POI, the shape of the sample and the coil structure. Note that $\mathcal{S}$ is independent of the size and electrical parameters of the sample, and it will be called the shape factor throughout the dissertation. Note that choosing different fundamental dimensions for the shape size factor affects the normalization in Eqs. (2.39) and (2.42). However, the value of the shape factor is also scaled, which is canceled in Eq. (2.41) by the scaling of the size factor. Hence, the value of ξ, which will be used for UISNR and UISAR calculations, remains the same. For some coil structures, the shape factor may also include electric dipole terms; however, towards reaching UISNR and UISAR at the quasi-static limit, these terms should be avoided as explained previously.

For an arbitrary sample shape, finding the maximum value of $\mathcal{S}$ can be carried out either analytically, by CAD tools or by using optimization methods that have been previously shown [3, 21]. The importance of the shape factor is that it is independent of the static magnetic field strength, the imaging parameters and the parameters of the sample such as the permittivity, permeability, conductivity, size and temperature. Hence, the dependence of UISNR and UISAR on these parameters can be shown analytically, as will be done in the following sections. Furthermore, the maximum value of the shape factor, which will be denoted by $\mathcal{S}_{\max}$, is for the coil geometry that is optimal for the subject to be imaged, and the location of the POI inside the subject. Therefore, it does not include any coil specific weighting. Hence, the effect of the inefficiency of non-optimal coil structures can be reported with respect to the optimal coil as follows:

$$e_{\text{coil}} \triangleq \frac{\mathcal{S}}{\mathcal{S}_{\max}} \tag{2.43}$$

which separates the coil and subject dependencies in the magnetic field-per-square-root-power expression:

$$\xi \;=\; e_{\text{coil}}\, \mathcal{S}_{\max}\, \frac{1}{\omega_0 \mu \sqrt{\sigma}}\, r^{-2.5} \tag{2.44}$$

The rotating magnetic field is the signal that is used to reconstruct the images, and the total absorbed power is related to both the noise in acquired images and the heating in the sample; hence, ξ can be converted to UISNR and UISAR as will be shown in the succeeding sections.

2.6 Signal-to-Noise Ratio at the Quasi-Static Limit

Using Eqs. (2.14) and (2.44) in Eq. (2.28), the intrinsic SNR can be defined at the quasi-static limit as:

$$\text{ISNR} \;=\; \frac{\sqrt{2} M_0}{\sqrt{4 k_{\text{B}} T \sigma}}\, \mathcal{S}\, r^{-2.5}. \tag{2.45}$$

Employing the definition of M_0 as given in reference [15] to show explicitly the dependence on the static magnetic field yields:

$$\text{ISNR} \;=\; \frac{N\gamma^2\hbar^2 I_z\,(I_z+1)}{\sqrt{18k_B^3}}\; e_{\text{coil}}\; \mathcal{S}_{\max}\; B_0 T^{-1.5}\sigma^{-0.5} r^{-2.5}. \tag{2.46}$$

where N is the number of nuclear spins per unit volume, $\hbar$ is the reduced Planck constant, and I_z is the quantum spin number for the nucleus of interest. Note that although the terms of the fraction are nucleus-dependent (ex: H^+, Na^+, etc.), they are independent of the sample and the coil. Furthermore, $e_{\text{coil}}\;\mathcal{S}_{\max}$ is the only term in Eq. (2.46) that depends on the coil geometry, the POI and the shape of the sample. For the coil geometry that is optimal for the subject, $e_{\text{coil}} = 1$ and hence an analytic expression for the UISNR can be obtained as the following:

$$\text{UISNR} \;=\; cN\gamma^2 I_z\,(I_z+1)\;\mathcal{S}_{\max}\; B_0 T^{-1.5}\sigma^{-0.5} r^{-2.5}. \tag{2.47}$$

where $c = 5.11\times10^{-35}$ is a constant with units $J^{0.5}K^{1.5}s^2$. When searching for the optimum coil structure, the optimization can be made either for a specific magnetic field value at a certain POI or for a field distribution in a certain region. Note that the coil factor e_{coil} is the only different term in Eqs. (2.46) and (2.47), and these two cases will most probably yield different coil structures and different $\mathcal{S}_{\max}$ values. However, the other terms in Eqs. (2.46) and (2.47) will be unaffected. Hence, Eq. (2.47) is valid for both optimization cases. Eq. (2.47) provides intuitive information about how the UISNR and therefore the SNR depend on the size, permittivity, conductivity and temperature of the sample, and the static magnetic field strength. Furthermore, the dependence on the gyromagnetic ratio of the imaged nucleus and the available spin density (N) are explicitly given, and it is shown that SNR and UISNR are independent of the permeability of the sample.

By grouping the constants together as $c' = cN\gamma^2 I_z\,(I_z+1)$, the simplified expressions for ISNR and UISNR can be obtained as:

$$\text{ISNR} \;=\; c'\; e_{\text{coil}}\; \mathcal{S}_{\max}\; B_0 T^{-1.5}\sigma^{-0.5} r^{-2.5}. \tag{2.48}$$

$$\text{UISNR} \;=\; c'\; \mathcal{S}_{\max}\; B_0 T^{-1.5}\sigma^{-0.5} r^{-2.5}. \tag{2.49}$$

Using these expressions, the SNR of an experiment that can be expected with the coil at hand, and the ultimate SNR that could be achieved with an optimal coil geometry can be obtained by multiplying ISNR and UISNR with Υ, respectively.

Assuming that the number of voxels is unchanged, it can be easily shown that the dependence of the imaging parameters on the size of the sample is $\Upsilon \propto r^3$, as the voxel volume is the only size-dependent term in Υ. Hence, $\text{SNR} = \Upsilon\Psi \propto r^{0.5}\sqrt{N_{\text{rep}}}$, and to obtain the same SNR level from two identical samples that only differ in size, the required total imaging time (which is proportional to N_{rep}) is given by $T_{total} \propto 1/r$.

When the size of the imaged sample becomes smaller, a very small coil is sufficient to image the sample, in which case, the total absorbed power will be limited to very low levels. As a result, the UISNR approaches infinity, which can be seen from Eq. (2.47) by taking the size term (i.e., r) to zero. However, a single voxel would simultaneously approach zero more rapidly (i.e., $\mathcal{V} \propto r^3$), making the SNR limit finite.

2.7 Specific Absorption Rate at the Quasi-Static Limit

At the quasi-static limit, by using Eq. (2.44), ISAR can be expressed as follows:

$$\text{ISAR} = \frac{\sigma B_0^2 r^5}{m_{\text{sample}}\ e_{\text{coil}}^2\ \mathcal{S}_{\text{max}}^2} \tag{2.50}$$

The only parameter in Eq. (2.50) that depends on the POI location, the shape of the sample and the coil structure is the shape factor $\mathcal{S} = e_{\text{coil}}\ \mathcal{S}_{\text{max}}$. Hence, finding the UISAR corresponds to maximizing the shape factor (i.e., finding the ideal coil, $e_{\text{coil}} = 1$), which leads to the expression:

$$\text{UISAR} \quad = \quad \frac{\sigma B_0^2 r^5}{m_{\text{sample}} \mathcal{S}_{\text{max}}^2}. \tag{2.51}$$

Maximization of the shape factor is an optimization process, similar to obtaining UISNR from ISNR. Hence, some constraints should be set. This can be

accomplished by aiming at a certain flip-angle at a specific position or for a flip-angle distribution among many points inside the sample. Methods for minimizing the SAR for a flip-angle distribution or magnetic field distribution among many points have been shown previously [21, 22]. Note that the constraints should be normalized with the flip-angle value used for ISAR definition, $\gamma\mu|H_{\mathrm{f}}^{\mathrm{t}}(\mathbf{x}_0)|$, to be consistent.

An important point is that as long as the specified field and SAR distributions are consistent with each other, the $\mathcal{S}_{\max}$ values of UISNR and UISAR will be the same. Eq. (2.51) provides intuitive information about the dependence of UISAR on the static magnetic field strength and the sample parameters including permittivity, conductivity and size. Furthermore, it is shown that UISAR and therefore SAR are independent of the permeability of the sample.

2.8 Example Case: Cylindrical Sample

In various MRI applications, such as small animal, human extremity and phantom imaging, the sample that will be imaged can be modeled by a circular cylinder (Fig. 2.1). Therefore, a uniform, electrically small and conductive cylindrical sample is studied as a practical case. To arrive at the UISNR and UISAR equations of the cylindrical sample, two different cases are considered: when the POI is on the axis of the cylinder and when the POI is very close to the surface. Note that single point optimizations are made for both cases. For the POI at the center, an analytic solution is obtained similar to [45]. When the POI is very close to the surface, the problem is equivalent to a semi-infinite planar sample case and is replaced with the latter to find two equations for the semi-infinite planar case. Then the two cases are combined using asymptotic methods into two equations for UISNR and UISAR of the cylindrical sample. For all of these cases, the resulting UISNR and UISAR expressions are in the same form as Eqs. (2.47) and (2.51).

Analytic expressions for UISNR and UISAR in a cylindrical sample when the

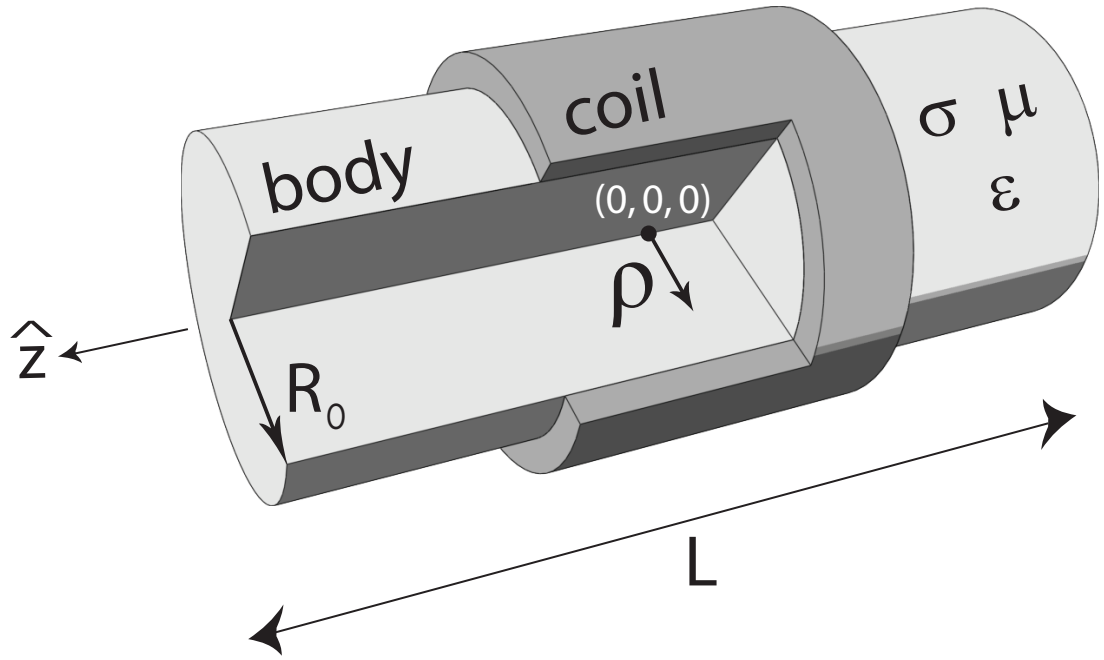

Figure 2.1: Geometrical structure of the studied practical sample. R_0, L, σ, ϵ and μ are the radius, length, conductivity, permittivity and permeability of the sample, respectively. ρ is the radial distance from the axis of the cylinder to the point of interest. The region titled "coil" shows a possible location of the RF coil for better visualization of the structure, not the exact shape or position. d is defined as $d = 1 - \rho/R_0$. $d = 1$ corresponds to the axis of the sample, whereas $d = 0$ and $d = 0.5$ correspond to the surface and the half-way point between the surface and the axis of the cylinder, respectively.

POI is on the axis are found as follows: For a cylindrical sample aligned with the z-axis, the electric and magnetic field components along the z-axis are expressed using the cylindrical wave expansion as given in reference [59] and in Eqs. (A.1) and (A.2). Then the transverse components of the electric and magnetic fields are derived from the z-components $\big($electric field components given in Eq (A.3)$\big)$ with the aid of Maxwell's Equations [60]. The received forward-polarized magnetic field is defined in Eq. (A.5), and the total absorbed power is given in Eq. (A.9). The minimum noise power for a preset signal strength is obtained using the Lagrange Multipliers Method [61] in Appendix A.2 $\big($Eq. (A.22)$\big)$. By substituting Eq. (A.23) into Eq. (2.45), an analytic UISNR expression can be obtained for the cylindrical sample when the POI is on the axis of the cylinder. Similarly, by using Eqs. (2.35) and (A.23) together, an analytic UISAR expression can be

achieved. The shape and size factors, (i.e., $\mathcal{S}$ and r) are obtained as $\mathcal{S} = 1.035$ and $r = R_0$, where R_0 is the radius of the cylinder. In [16], Reykowski found a similar expression with $\mathcal{S}$=0.9545 and $r = R_0$.

When the POI approaches the surface, an extremely confined field distribution created by a minute coil close to the POI is sufficient to create a signal at the POI. In that case, the effective sample seen by the coil will be a semi-infinite plane. By employing the semi-analytic method given in reference [5], the size factor r is found to be equal to the distance between the POI and the surface, and the shape factor $\mathcal{S}$ is obtained as 0.466 for a semi-infinite planar sample. However, as mentioned in the introduction, the choice of basis functions affects the numerical error, and therefore the results, significantly. Because we performed a cylindrical wave expansion for a planar structure, the required number of modes is very high, and the shape factor has a numerical error of approximately 10%. In reference [14], this sample shape was also studied and the analytical result presented [14] corresponds to a shape factor value of $\mathcal{S} = 0.423$. For the rest of our derivations, this shape factor will be used.

By employing asymptotic methods, the results for the semi-infinite planar and cylindrical samples can be combined into two equations given by the following:

$$\text{UISNR} = c' \, \mathcal{S}_{\max}^{\text{cyl}} B_0 T^{-1.5} \sigma^{-0.5} R_0^{-2.5} \tag{2.52}$$

$$\text{UISAR} = \frac{\sigma B_0^2 R_0^5}{m_{\text{sample}} \left(\mathcal{S}_{\max}^{\text{cyl}} \right)^2}. \tag{2.53}$$

where $\mathcal{S}_{\max}^{\text{cyl}} = 0.953\sqrt{1 + (0.723/d)^5}$. Note that the above equations are in the same form as Eqs. (2.47) and (2.51). $d = 1 - r_0/R_0$ is defined as the normalized distance between the POI and the surface of the sample (which is normalized with respect to the radius of the sample), and r_0 is the radial distance between the POI and the axis of the cylinder. Note that d is a parameter between 0 and 1, and it is independent of the size of the sample.

2.8.1 Results

The analytic UISNR expression is compared with the semi-analytic method presented by Celik et al. [5]. The percentage error in the analytic expression is defined as the following:

$$error\ \% = 100\ \frac{\mathrm{UISNR_a} - \mathrm{UISNR_{s.a.}}}{\mathrm{UISNR_{s.a.}}} \tag{2.54}$$

where $\mathrm{UISNR_{s.a.}}$ denotes the solution of Celik's semi-analytic method, and $\mathrm{UISNR_a}$ denotes the analytic expression given in Eq. (2.52). For arriving at the analytic expressions, it was assumed in Section 2.5 that the distance between the surface and the POI is smaller than $1/\left|k\right|$. To observe the effect of this assumption on the error, the error curves in Figures 2.3 and 2.4 are plotted with respect to the normalized distance between the POI and the surface with respect to the wavelength. The wavelength and the wavenumber are related by the following equation:

$$\lambda = \frac{2\pi}{\Re\{k\}} = \frac{1}{\omega_0\sqrt{\mu\epsilon}\ \Re\{\sqrt{1 - j\ tan\delta}\ \}}. \tag{2.55}$$

Figure 2.2 shows the behavior of UISNR when the location of the POI is varied radially. Note that the vertical axis is in logarithmic scale for better understanding, and the UISNR values are normalized with respect to the UISNR value on the axis of the sample. The first important point is that the triangles, which show the data points obtained with Celik's method [5] stop at $d = 0.15$. This is because the semi-analytic method is vulnerable to numerical errors when the POI approaches the surface. Note that because this method is used as the reference with which the error rates are calculated, the range of d values for this and the succeeding plots are limited. Similarly, Reykowski did not calculate UISNR for $d < 0.15$ due to numerical errors [17]. Instead, an analytic expression was obtained using asymptotic methods [17] that is employed here. Although the semi-analytic methods fail, Reykowski's and our analytic expressions yield robust calculations for any POI location. The advantage of our analytic expression over Reykowski's method is that the dependence of UISNR on the geometrical and electrical properties of the sample are given explicitly for any POI location,

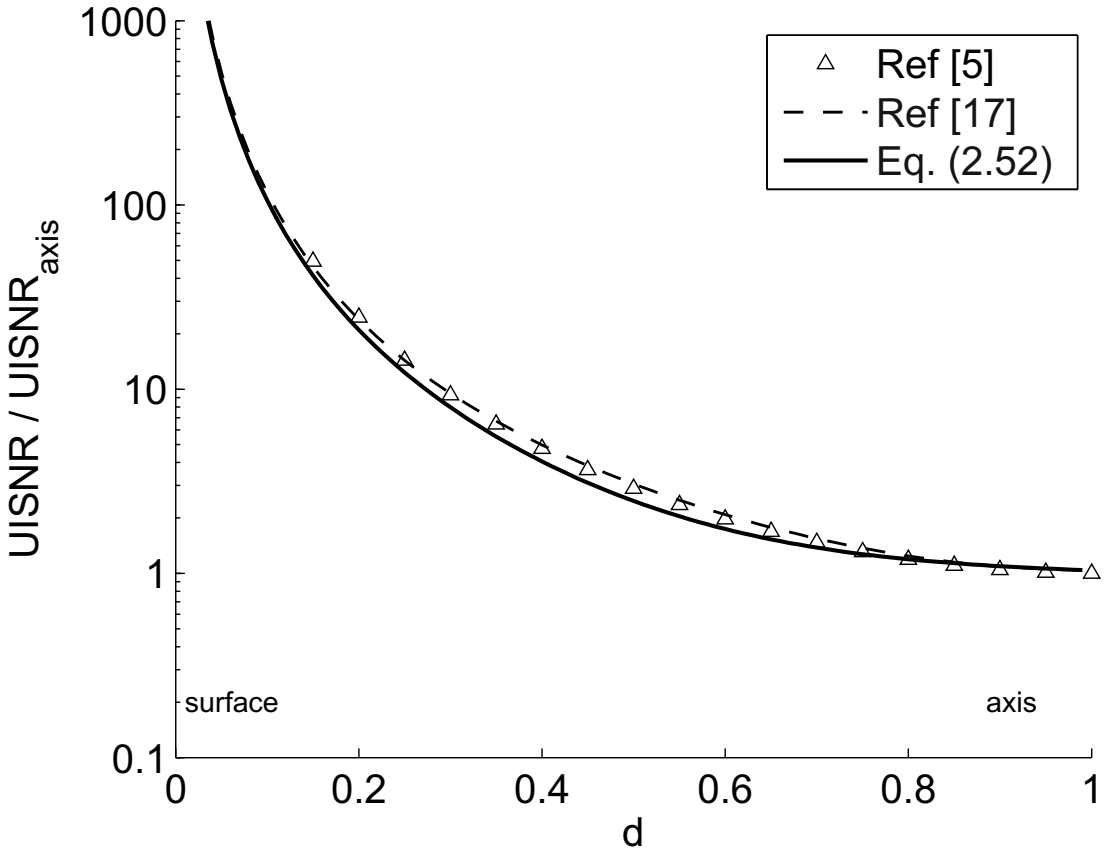

Figure 2.2: UISNR values normalized with respect to the UISNR on the axis of the cylinder. The horizontal axis shows the distance between the POI and the surface normalized with respect to the radius of the cylinder, i.e., $d = 1 - \rho/R_0$. The distributions are valid for any sample parameter and field strength, as long as the distance between the POI and the surface is smaller than the wavelength, i.e., $dR_0 \ll \lambda$.

whereas in Reykowski's method [16, 17], the dependence on the sample properties is given only when the POI is at the center. Although our expression has some error when the POI is at the middle region (between the center and the surface) of the sample, the error drops to negligible levels towards the axis and the surface of the sample. The maximum error in our formulation was calculated to be less than 10%.

Another important point for Fig. 2.2 is that the UISNR increases steeply towards the surface of the sample, approaching infinity at the surface. This is expected because when the POI is very close to the surface, a minute coil is

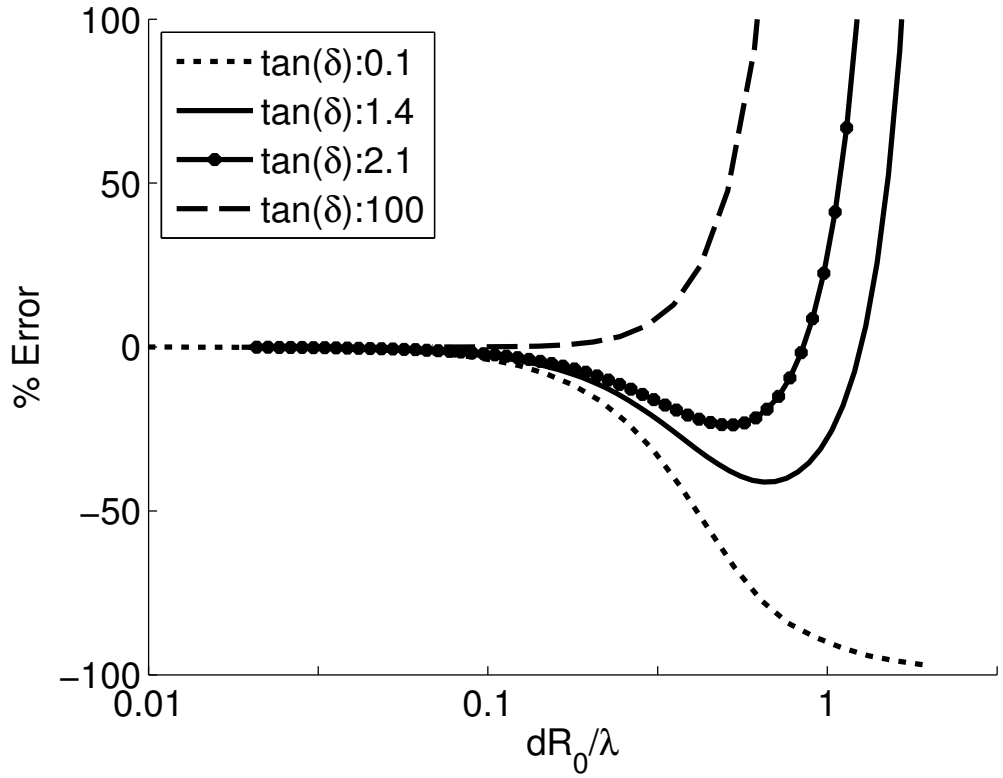

Figure 2.3: The error in the analytic UISNR expression (Eq. (2.54)) for various loss tangent values. $tan(\delta) = 0.1$ and $tan(\delta) = 100$ curves are the approximate limits although they do not correspond to any tissue parameters at MRI frequencies. Although $tan(\delta) = 1.4$ and $tan(\delta) = 2.1$ curves can represent an infinite number of permittivity, conductivity and frequency combinations, two examples are $\sigma = 0.4$ S/m and $\sigma = 0.6$ S/m, respectively, for $\epsilon_r = 80$ and $B_0 = 1.5$ T. The horizontal axis is the distance between the POI and the surface in terms of the wavelength (i.e., a value of 0.1 means the distance is one-tenth of the wavelength); hence, the curves represent the error behavior regardless of the field strength.

sufficient to image the POI. With such a coil, the absorbed power is confined to an extremely small region around the POI, increasing the SNR significantly.

Figure 2.3 shows the error in the analytic expression given in Eq. (2.52) for various loss tangent values. It should be noted that loss tangent can be converted to conductivity using the formulation given in Section 2.5. Although they do not correspond to any tissues at MRI frequencies, $tan(\delta) = 0.1$ and $tan(\delta) = 100$ values are employed to illustrate the limits of the error curves.

Increasing or decreasing the loss tangent beyond these values does not alter the curves significantly, and leads to numerical error in the semi-analytic method given in reference [5]. The error curves are independent of the main magnet strength and the electrical parameters of the sample, but depend on the loss tangent, which is a combination of these parameters; as long as the loss tangent is the same, the error behavior is the same. Hence, any curve can correspond to an infinite number of permittivity, conductivity and frequency combinations. One of these combinations for the $tan(\delta) = 1.4$ curve is a static magnetic field strength of 1.5 T, a conductivity of 0.4 S/m and a relative permittivity of 80, which are average human body parameters at 64 MHz [1, 62]. For these parameters and an error margin of 20% the obtained UISNR expression is valid as long as $dR_0 < \lambda/4$, which corresponds to a POI depth of approximately 15 cm. For this plot, the POI is assumed to be on the axis of the cylinder; however, the effect of the location of the POI is insignificant, as will be discussed in the succeeding paragraph.

For various sample sizes and POI locations, the error in the analytic UISNR expression is shown in Figure 2.4, where the horizontal axis is the ratio of the distance between the POI and the surface to the wavelength (i.e., electrical length). It can be seen that the error is only slightly affected when the POI location varies. Evaluating this slight change with the behavior of the error given in Figure 2.3, it can be concluded that the effect of the loss tangent is much higher than the POI location, and the electrical length, rather than the metric distance between the POI and the surface, is a determining factor. Another important point is that if the POI is at the center, i.e., $d = 1$, a sample with radius $R_0 = \lambda/2$ has 50% error when the analytic expression is used. For the same sample, when $d = 0.15$ however, $dR_0/\lambda = 0.075$, and the error is negligible. This supports the argument that the obtained expressions are valid for samples that are comparable to the wavelength if the distance between the POI and the surface is much smaller than the wavelength.

In Table 1, the error in Eq. (2.52) is given for human brain, muscle and liver tissue parameters [1]. Note that a cylindrical sample that is composed of only one type of tissue is assumed for the calculations. It is known from Figures 2.3 and 2.4 that when the distance between the surface and the POI is smaller than $\lambda/10$, the

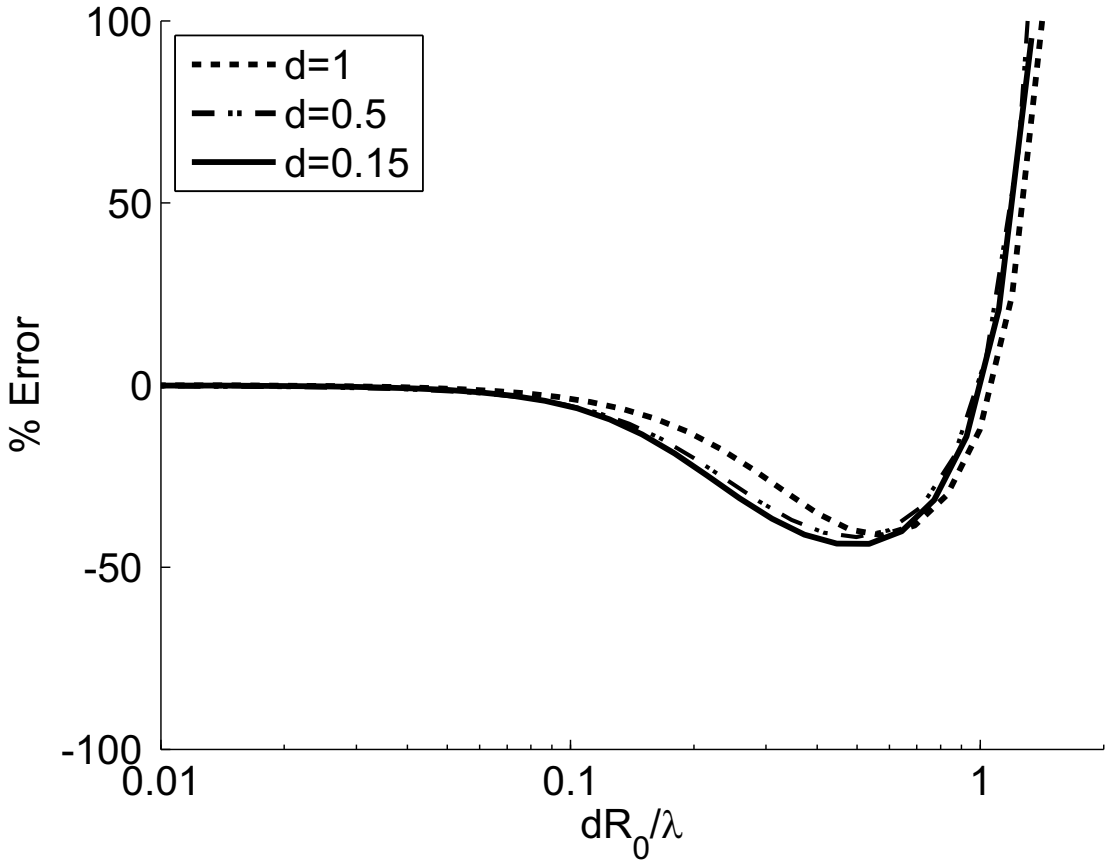

Figure 2.4: The error in the analytic UISNR expression (Eq. (2.54)) for various point of interest locations inside the sample. The horizontal axis is the distance between the POI and the surface in terms of the wavelength (i.e., a value of 0.1 means the distance is one-tenth of the wavelength); hence, the curves represent the error behavior regardless of the field strength.

error is negligible. However, for SNR calculations in MRI, larger error margins such as 10% or 25% can be employed. When the distance between the surface and the POI is close to $\lambda/5$, the error becomes 10%. When the error margin is 25%, the expressions can be used at distances up to slightly above $\lambda/3$, as shown in Table 1. As an example, when a cylindrical sample with liver parameters is imaged, UISNR of a point at a depth of 15 cm can be calculated with less than 25% error. When a similar sample with muscle properties is imaged, the expressions yield less than 25% error even at a distance of one wavelength. However, it should be kept in mind that these are example calculations. In real-life, the human body is neither cylindrical nor homogeneous, and the tissue parameters may differ from person to person; hence, these error rates may be different.

ϵ_r [F/m]	σ [S/m]	B_0 [T]	λ [cm]	1% error distance [cm]	10% error distance [cm]	25% error distance [cm]
80	0.4	1.5	40.4	2.7	8.9	15.5
60	0.5	3.0	23.9	1.6	5.0	8.5
110	0.5	1.5	34.9	2.3	7.7	13.0
70	0.7	3.0	21.6	1.5	4.7	8.1
80	0.6	1.5	37.5	2.7	9.2	38.0
60	0.8	3.0	22.2	1.6	5.2	10.5

Table 2.1: Parameters for some tissues in the human body for 1.5T and 3T static magnetic field strengths [1]. The first two rows are for liver tissue, the third and fourth rows are for brain tissue and the last two rows are for muscle tissue. The columns are for relative permittivity, conductivity, static magnetic field strength, wavelength and the distances at which the error of Eq. (2.52) is 1%, 10% and 25%, respectively. When calculating the error, a cylindrical sample composed of only one type of tissue is assumed.

2.9 Discussion and Conclusions

In this study, analytic expressions for the ultimate intrinsic signal-to-noise ratio (UISNR) and ultimate intrinsic specific absorption rate (UISAR) are derived. The expressions are valid as long as the distance between the surface and the point of interest is smaller than the wavelength, which is referred to as the quasi-static limit. The expressions are independent of the shape of the sample that is to be imaged.

In the course of arriving at the analytic expressions, size and shape factors of a sample's shape and coil geometry are defined. The shape factor depends on the geometrical shape of the sample and the coil structure. Hence, it is specific to the coil and sample combination. Finding the maximum value of the shape factor for all theoretically possible coil structures yields the UISNR and UISAR of the sample of interest. The size factor explicitly shows the scaling of ISNR and ISAR (hence UISNR and UISAR) with any variations in the size of the sample. The shape factor is defined for the first time to the best of our knowledge. Although the dependence on the size factor was previously shown for specific geometries, it is defined for an arbitrarily shaped sample for the first time.

The derived expressions explicitly show the dependence of UISNR and UISAR on the static magnetic field strength and the sample properties including the size, permittivity, conductivity and temperature. Furthermore, it is shown that UISNR and UISAR are independent of the permeability of the sample.

Using the relations between SNR and ISNR and those between SAR and ISAR that are given in this study, the dependence of SNR and ultimate-SNR and that of SAR and ultimate-SAR on the shape and size factors and any of the other affecting parameters can be obtained easily.

The strongest aspect of the expressions given in this study comes into picture when there is a known value for SNR, SAR, UISNR or UISAR that is obtained by experiment or by simulation. Then, these parameters can easily be calculated for a similar sample shape when any affecting parameter is altered.

Previous studies of UISNR and UISAR in the literature use optimization methods to find the UISNR and/or UISAR for either certain field/SAR distributions in the sample or certain field/SAR values at specific points. The given expressions in this dissertation are valid for both cases. Furthermore, UISNR and UISAR were defined in the literature to form coil performance maps to evaluate coil performances and determine room for improvement. The proposed expressions can be employed for this purpose as well.

For specific geometries of interest, the dependence of UISNR on the size of the sample, i.e., $r^{-2.5}$, was previously shown. Hoult and Lauterbur show the same dependence for a spherical sample [15] for low frequencies, in which the size factor is the radius of the sphere. For a semi-infinite planar sample at the quasi-static limit, Wang et al. show that UISNR has the same dependence in which the size factor is the distance of the POI to the surface of the sample [14]. For a cylindrical sample, Macovski has shown that the noise generated is proportional to $r_0^2\sqrt{l}$, where r_0 is the radius, and l is the length of the cylinder [63]. This corresponds to the ISNR part of the SNR formulation scaling with -2.5^{th} power of the size of the cylinder. Furthermore, the ultimate SNR was shown to vary with the -2.5^{th} power of the radius of a cylindrical sample when the POI is at the center [16, 45]. These four articles show the same dependence on the size of

the sample with our formulation but for specific geometries of interest.

The main limitation of the expressions given in this study is that the samples are assumed to be homogeneous during the derivations. It should be kept in mind that in real-life scenarios, samples are generally not homogeneous. Furthermore, if the distance between the POI and the surface is not in the quasi-static limit, the method introduces some error.

Chapter 3

SAR Reduction using Nonlinear Gradient Fields

Preface

The content of this chapter was presented in part at the Scientific Meetings of International Society of Magnetic Resonance in Medicine [64, 65], European Society of Magnetic Resonance in Medicine and Biology [66] and Turkish Society of Magnetic Resonance [67] and it was published in Magnetic Resonance in Medicine [68]. The text and the figures of this chapter are based on the journal publication [68].

3.1 Introduction

This study introduces a novel method for reducing the specific absorption rate (SAR) that uses gradient fields with nonlinear variations in space.

To prevent patient hyperthermia or other adverse effects during a magnetic resonance imaging (MRI) examination, the maximum SAR applied to patients

has been regulated [18, 19]. However, reducing the SAR below a certain level may impose restrictions on certain sequence parameters such as the maximum flip-angle, the minimum repetition time and the minimum pulse duration. The SAR varies quadratically with the field strength (Section 2.7, [47]); therefore, restrictions on the sequence parameters become more pronounced as the field strength increases. Although homogeneous B_1^+-fields ($B_1^+ = \mu H_f^t$, unit: tesla) are important in obtaining diagnostic-quality images, homogeneous fields can only be obtained with additional increases in the SAR. Because the restrictions imposed on the SAR hamper the imaging performance, reduction of the SAR while maintaining the levels of other imaging parameters has become an active research area in the field.

There is a trade-off between B_1^+-homogeneity and the SAR at all field strengths. In the high-field regime, B_1^+-inhomogeneities are more severe because of the increasing interference effects due to the wavelength and field attenuation caused by tissue conductivity. Therefore, various techniques have been devised to mitigate B_1^+-inhomogeneities. Examples of such techniques include B_1^+-shimming and multi-dimensional excitation pulses. The B_1^+-shimming methods [25] use coils with distinct spatial field variations and increase the homogeneity through separate adjustment of the signal amplitude and the phase for each coil. However, such methods increase whole-body and local (especially in regions close to the individual transmit coil elements) SAR values. Multi-dimensional pulses [26–30] increase the homogeneity by specifying the variation of the excitation profile in three dimensions. However, because such pulses are more condensed than the conventional excitation pulses, obtaining the same flip-angle without increasing the pulse duration requires a higher SAR. In contrast, the effects of inhomogeneity are less severe in the low-field regime; therefore, approaches designed to reduce inhomogeneity in this regime are mostly limited to coil design. Although the "stubby" birdcage coil [69] was designed to optimize the signal-to-noise ratio (SNR) along its axis, the coil generates a nonhomogeneous B_1^+-field. Hence, longer birdcage coils are used instead. However, these longer coils expose a larger volume of the subject to electromagnetic waves; increasing the whole-body SAR (but not necessarily the local SAR). The trade-off between B_1^+-homogeneity and

the SAR is not a problem limited to the high-field regime but represents a major problem at all field strengths.

Arguably, the most well-known approach for decreasing the SAR is the variable-rate selective excitation (VERSE) algorithm [31]. With time-varying gradient waveforms instead of the conventional trapezoidal waveforms, the VERSE algorithm modifies the amplitude of the (RF) pulse to decrease the whole-body SAR while keeping the spatial variations of the SAR and the flip-angle unaltered. Although this approach can significantly reduce the SAR, the performance of this method is limited when the gradient waveforms are already restricted by the limitations on the slew-rate or the gradient amplitude. Furthermore, the off-resonance performance of the VERSE technique is rather poor because the time-varying gradient waveforms cause blurring rather than shifting.

It is known that the gradient fields are not perfectly linear and that these nonlinearities cause curved slices and warped images. To correct for such effects, many recent studies have focused on measuring these nonlinearities using field probes [70] or preceding measurement scans [71]. As an alternative, several investigators have exploited the nonlinearity of the gradients to their advantage by obtaining curved slices [34–36, 72] and non-uniform resolution [38–42]. It has been shown that when nonlinear gradient fields are used, the adiabatic condition in flow-driven arterial spin labeling measurements could be achieved with smaller RF pulse amplitudes and as a result, lower SAR values [73]. However, to the best of our knowledge, no research has been conducted that demonstrates the effect of nonlinear gradient fields on the RF pulse shape toward reducing the SAR.

In this study, we propose using gradient fields with nonlinear variations in space to reduce the whole-body SAR without changing the spatial distribution of the SAR [64]. To reduce the complexity of the problem, we first demonstrate the technique on two one-dimensional excitation cases. In a third example, we study the effect of a nonlinear gradient field on the SAR in a multi-dimensional excitation scheme. Furthermore, we compare and combine the proposed technique with the VERSE algorithm.

3.2 Theory

Conventional MRI methods employ fields that vary linearly in space for excitation and encoding, also known as gradient fields. In contrast, the higher-order fields, which are used for shimming the static magnetic field, are widely called shim fields. In this text, we will refer to the former as "linear gradient fields" (LGFs) and to the latter as "nonlinear gradient fields" (NLGFs), to signify their respective roles in the encoding process.

The SAR depends on many factors, including the RF coil, the flip-angle, the pulse duration and the pulse shape. This study focuses on altering the pulse shape using nonlinear gradient fields. To emphasize this effect on the SAR, we define the normalized SAR (nSAR) as follows:

$$\text{nSAR} \triangleq \int_{-1/2}^{1/2} |b(s)|^2 \; ds \tag{3.1}$$

where $b(s)$ denotes the normalized RF pulse, which is defined using the unit duration and unit integral approach $\big($Eq. (2.24)$\big)$ as follows:

$$b(t/\tau) \triangleq \frac{\gamma\tau}{\alpha} B_1(t) \tag{3.2}$$

where γ denotes the gyromagnetic ratio and $B_1(t)$, τ and α denote the envelope, the duration and the flip-angle of the RF pulse, respectively. Note that, the normalized SAR is equal to the energy of the normalized RF pulse envelope e_{RF}, and hence it is unitless. The RF pulse is normalized using the unit integral approach $\big($Eq. (2.24)$\big)$ so that the RF pulses that will be designed are easier to demonstrate (please refer to Section 2.2.2.1 for the definition). In the pulse shape design process, the aim is to minimize the normalized SAR (nSAR) while achieving the desired excitation profile. The minimum value for the nSAR is one, which is the value that holds for the rectangular pulse.

First, the relationship between the nSAR and the excitation profile will be formulated for one-dimensional gradient fields and objects for simplicity. We define the excitation profile as the transverse component of the magnetization normalized by the magnetization density and denote this unitless quantity as $m(z)$. It

is known that at the small-tip-angle regime, the RF pulse that approximately excites the desired excitation profile can be expressed by the following equation [23]:

$$B_1(t) = -i\frac{G}{2\pi}M\left(\frac{\gamma}{2\pi}Gt\right) \tag{3.3}$$

where G denotes the amplitude of the LGF and $M(k)$ denotes the Fourier transform of the excitation profile (i.e., the excitation k-space) where $k = \frac{\gamma}{2\pi}Gt$ and i is the imaginary unit; in this equation, a complete refocusing is assumed. In practice, the RF pulses are limited in time using apodization functions. Because such a function complicates the discussion, in this study we simply truncate the RF pulses to a duration of length τ. In this case, the normalized RF pulse can be expressed by the following equation:

$$b(s) = \frac{M\left(\frac{\gamma}{2\pi}G\tau s\right)}{\left|\int_{-1/2}^{1/2} M\left(\frac{\gamma}{2\pi}G\tau s'\right)ds'\right|} \tag{3.4}$$

It can be observed from Eqs. (3.1) and (3.4) that the normalized SAR depends on the excitation profile.

When an NLGF is used, the dependence of the SAR on the excitation profile is altered. Instead of the gradient field Gz, let us assume a nonlinear field $G_w w$ where $w = f(z)$ denotes the variation of the field in space is used, and w is defined as a nonlinear coordinate variable. When the transformation from z to w is bijective, the inverse function, $f^{-1}(w)$, exists. In this case, the excitation profile can be expressed in terms of the nonlinear coordinate: $m(z) = m\big(f^{-1}(w)\big) = m_{\mathrm{n}}(w)$, and the normalized RF pulse can be expressed in terms of the Fourier transform of $m_{\mathrm{n}}(w)$, $M_{\mathrm{n}}(\cdot)$ as shown in the following formula:

$$b_{\mathrm{n}}(s) = \frac{M_{\mathrm{n}}\left(\frac{\gamma}{2\pi}G_w\tau s\right)}{\left|\int_{-1/2}^{1/2} M_{\mathrm{n}}\left(\frac{\gamma}{2\pi}G_w\tau s'\right)ds'\right|} \tag{3.5}$$

Fig. 3.1 demonstrates how the RF pulse changes for an NLGF with $f(z) = z - 10^{-3}sin(2\pi z/0.032)$ variation (all distances are in meters) is used. It is known that the slope of the gradient field affects the thickness of the excitation profile. For NLGFs, because the slope varies with position, the excitation profile is distorted. To correct this distortion, the excitation k-space needs to be distorted in

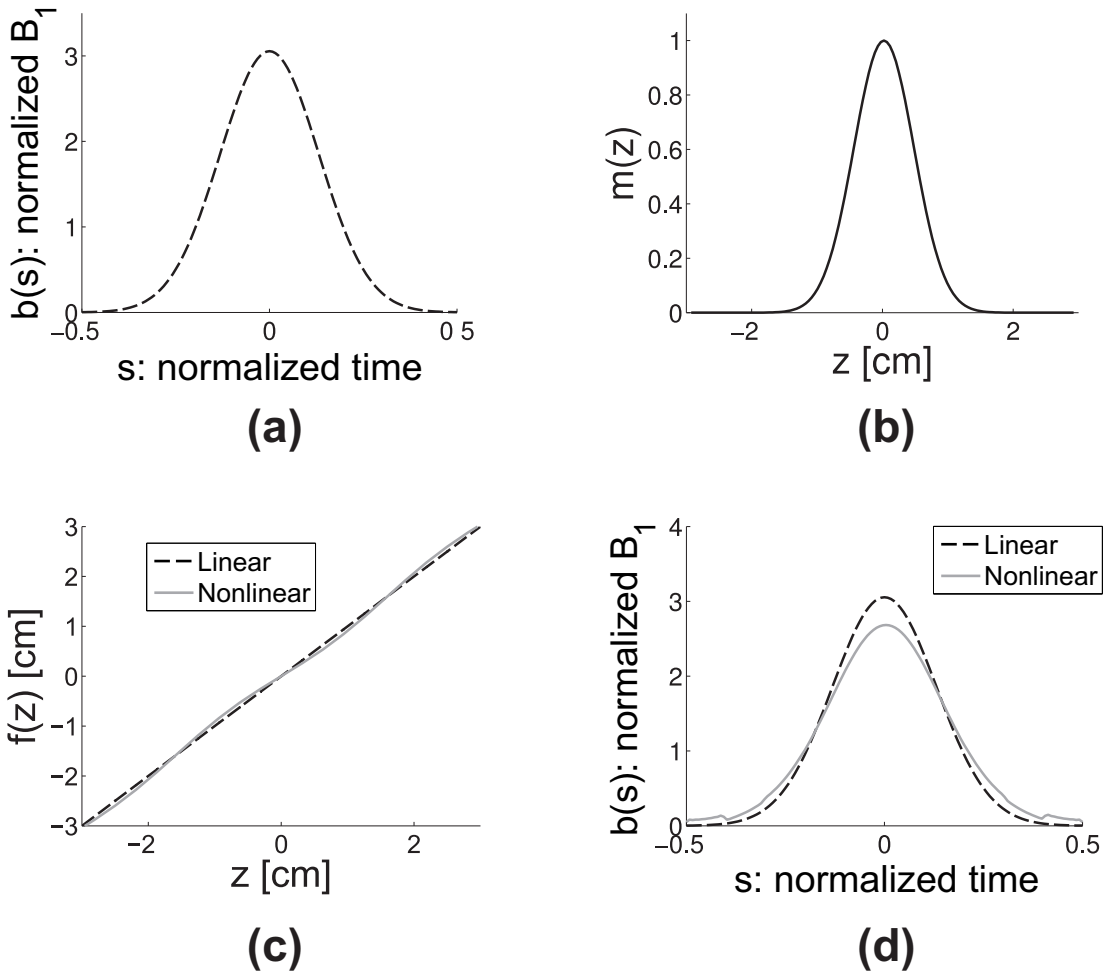

Figure 3.1: One-dimensional example demonstrating the effect of using a nonlinear gradient field on a normalized RF pulse. **a:** An apodized sinc pulse with a time-bandwidth product of 2 is selected as the reference solution. **b:** The excitation profile of the apodized sinc pulse in the presence of a perfectly linear gradient field. **c:** The variation of the NLGF in space compared with the LGF. **d:** The RF pulse that obtains the desired profile in the presence of the NLGF is compared with the apodized sinc pulse.

a compensatory fashion that corresponds to another RF pulse shape (Fig. 3.1), and a different SAR value; for this example, the nSAR is reduced from 2.16 to 1.85. As a result, the SAR changes when a nonlinear gradient field is used.

It is known that unless the region-of-interest (ROI) is not extremely narrow in at least one direction, a one-dimensional NLGF is not realizable; such a field would display a similar variation along at least one other direction. Therefore,

the above formulation will be expanded to three-dimensional objects and multi-dimensional RF excitation pulses. Although the multi-spoke approach [30] is used in this study, these formulations can be trivially modified to fit other schemes.

As in the one-dimensional case, the transformation from the linear coordinate system, $\mathbf{x}$ (with spatial variables x, y, and z) to the nonlinear coordinate system, $\mathbf{u}$ (with spatial variables u, v, and w) can be written as $\mathbf{u} = \mathbf{f}(\mathbf{x})$, where $\mathbf{f}(\mathbf{x})$ denotes the spatial variation of the NLGFs. If the NLGFs are bijective, then the desired excitation profile, $m(\mathbf{x})$, can be expressed as $m_{\mathrm{n}}(\mathbf{u}) = m\big(\mathbf{f}^{-1}(\mathbf{u})\big)$. Hence, the p^{th}-spoke of the normalized RF pulse can be expressed as

$$b_{\mathrm{n}p}(s) = \frac{M_{\mathrm{n}}\left(k_{up}, k_{vp}, \frac{\gamma}{2\pi} G_w \tau s\right)}{\left|\sum_{p=1}^{P} \int_{-\tau_p/2\tau}^{\tau_p/2\tau} M_{\mathrm{n}}\left(k_{up}, k_{vp}, \frac{\gamma}{2\pi} G_w \tau s'\right) ds'\right|} \tag{3.6}$$

where $M_{\mathrm{n}}(\mathbf{k}_{\mathrm{n}})$ is the Fourier transform of $m_{\mathrm{n}}(\mathbf{u})$ and $\mathbf{k}_{\mathrm{n}} = [k_u \quad k_v \quad k_w]$. In Eq. (3.6), p is the spoke index, P is the total number of spokes, τ_p is the duration of the p^{th}-spoke and $\tau = \sum_{p=1}^{P} \tau_p$ is the total pulse duration. It should be noted that, because this is a spoke excitation scheme, multiple RF segments that are in the k_w-direction, positioned at (k_{up}, k_{vp}) locations are used. Finally, the normalized SAR can be calculated by normalizing the total RF waveform by τ. When $\mathbf{u}$, G_w and $M_{\mathrm{n}}(\cdot)$ are replaced with $\mathbf{x}$, G_z and $M(\cdot)$, Eq. (3.6) reduces to the linear case, resulting in $b_p(s)$. Although the general formulations of these equations are similar, the excitation k-space is affected by the gradient nonlinearity when $M(\mathbf{k})$ is replaced by $M_{\mathrm{n}}(\mathbf{k}_{\mathrm{n}})$. Hence, the SAR is altered when an NLGF is used.

When the nonlinear field is non-bijective, special care must be taken when applying the above formulation. In this case, the same field values are observed at multiple locations in space, meaning that the amount of excitation (i.e., the flip-angle) will be the same at those positions. Therefore, whether the above formulation can be used directly depends on the desired excitation profile. We will now investigate such cases and provide simple one-dimensional examples for each case:

i. In special cases, the desired excitation profile can be compatible with the non-bijective NLGF. For example, an excitation profile symmetric around $z = 0$ can be obtained using a z^2 field. In this case, no special treatment is

necessary.

ii. In other cases, the field can be made compatible with the desired profile by combining it with other gradient fields. For example, a symmetric profile around $z = z_0$ where $z_0 \neq 0$ cannot be realized with a z^2 field. However, a $z^2 - 2zz_0$ field is compatible with the profile and can be obtained with the simultaneous use of an LGF with the NLGF.

iii. If no combination of the available fields yields a compatible field distribution, then the excitation profile can only be approximately generated using non-bijective fields. However, in such a case, the residual part of the profile can be realized using a set of bijective gradient fields. For example, a profile that is not symmetric can be decomposed into symmetric and anti-symmetric components; the former can be obtained using the z^2 field, whereas the latter can be excited using an LGF.

As it can be observed, even non-bijective fields can be used to obtain the desired excitation profile when integrated with the proper combination of LGFs.

When NLGFs are used for excitation, the excitation k-space, and hence the SAR, are modified. Depending on the nonlinearity of the field and the excitation profile, the SAR may decrease or increase. However, if LGFs are still available, the SAR-optimal solution will use the LGFs in the worst case. Therefore, when NLGFs are added to the set of available fields, the SAR may only be reduced.

3.3 Materials and Methods

The effect of NLGFs on excitation and the SAR is demonstrated with three examples. To highlight such effects, the first two examples are one-dimensional ones and the third one is three-dimensional example to demonstrate how a realistic case can be handled. The simulations are performed in Matlab (The Mathworks Inc., Natick, MA, USA), and the experiments are performed using a 3T scanner (MAGNETOM Trio a Tim System, Siemens Healthcare, Erlangen, Germany).

As a descriptor of excitation efficiency, the root-mean-squared error (RMSE) between the desired and obtained profiles is calculated [27]. The RMSE and nSAR values will be reported in section 3.4.

3.3.1 Case 1) 1-D: Pulse Design for a Given Nonlinear Field

In this example, the effect of a slight nonlinearity on the SAR is investigated using the field distribution given in Fig. 3.1. An apodized sinc pulse with no side lobes (time-bandwidth product: 2, the default RF pulse in the basic gradient echo pulse sequence obtained from Siemens Healthcare, Erlangen, Germany) is used as the reference solution. Using the excitation profile of the reference solution (Fig. 3.1), the RF pulse for the nonlinear gradient field case was designed.

To realize the desired NLGF experimentally, a coil with a 2.4 cm diameter is designed on a polyoxymethylene cylinder using the target-field method [74]. The required current distribution along the z-axis is sampled at intervals of 4 mm and truncated to a total length of 6.4 cm. The corresponding field is simulated and given in Fig. 3.2. Note that although truncation causes some deviations in the field, these deviations are outside the full-width-half-max (FWHM) of the desired excitation profile and therefore, only slight contractions are expected outside the FWHM.

In the experiments, a cylindrical water phantom with a 1.4 cm diameter is used. To observe the excitation profile, the readout is performed in the excitation direction. To drive the custom-made coil, the optically isolated x-gradient waveform generated by the scanner is amplified using an audio amplifier (TonyLee Dj 451, JCLEON, PRC; maximum power, 450W). The maximum required current was approximately 0.1A. To limit the waveform distortion to below 2%, 20Ω resistance is used in series with the amplifier. During the experiments, the amplifier of the x-channel was turned off to keep the excitation direction parallel to the

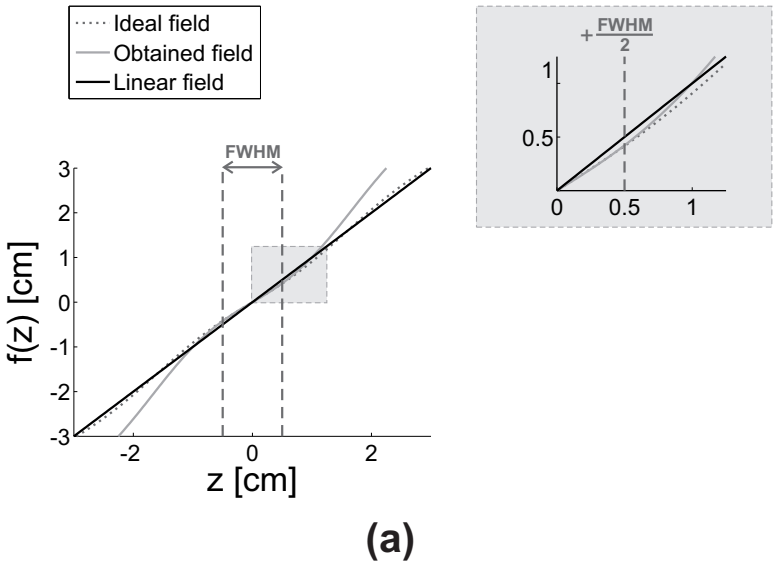

Figure 3.2: The effect of truncating the required current distribution on the resulting field, and the coil produced using the truncated distribution. **a:** The field realized when the current distribution is truncated to 6.4 cm is compared with the ideal and the linear fields: a close-up version of f(z), indicating the half of the FWHM shows that the deviation of the realized field from the ideal is negligible inside the FWHM (top-right corner). **b:** The gradient coil wound on a polyoxymethylene cylinder. Winding separation: 4 mm, winding diameter: 2.4 cm.

z-axis. Therefore, the B_0-shimming is compromised, which leads to a dephasing of the spins. Although this dephasing causes a signal dropout (intra-voxel signal cancelation), the level of dropout for the small phantom used in the experiments was acceptable. In the experiments, a gradient echo sequence is used with the following parameters: flip-angle, 15°; RF duration, 1.25 ms; T_R, 9.1 ms; T_E, 4.9ms; excitation gradient amplitude, 7.4 $^{\mathrm{mT}}/_{\mathrm{m}}$; FOV_y and FOV_z (FOV along

the y- and z-directions, respectively), 116 mm and acquisition matrix, 128 x 256. Note that, T_R is the repetition time of the sequence and T_E is the echo time, i.e., the time interval between the transmission of the center of the excitation k-space and the acquisition of center of the image k-space $\big($For definitions, please refer to [48]$\big)$.

3.3.2 Case 2) 1-D: Field Design for Optimal SAR Pulses

Although a rectangular pulse is optimal in terms of nSAR, its excitation profile is not sufficiently selective; this promotes the use of other RF envelopes that have better selectivity - such as apodized sinc pulses - at the expense of higher nSAR (Fig. 3.3). It is known that by changing the slope of the gradient field, the excitation profile can be contracted or expanded. Therefore, by designing a field with a low slope in the excitation region and high slopes at the boundaries, the main lobe of the excitation profile of a rectangular pulse can be expanded and the side lobes of the excitation profile can be contracted, yielding enhancement in selectivity. Although the optimal NLGF would have infinite slopes at the boundaries, a physically realizable field that approximates this ideal field with the following expression

$$f(z) \;=\; z + 0.47\frac{z}{1+(z/0.09)^{16}} - 1.47\frac{z}{1+(z/0.03)^{16}}, \tag{3.7}$$

where all distances are in meters, is designed using the target field method [74]. To realize the field experimentally, a coil is wound on a cylinder similar to that used in "Case 1" (Fig. 3.3). However, because the field magnitude in this case is higher, the realized field can be measured using MRI by feeding the coil with the phase-encoding signal during a gradient echo image and by extracting the field of the coil from the distortion in the image (Fig. 3.3). The measured field is used as $w = f(z)$ in the simulations. It should be noted that, the number of turns is increased without changing the required current to attain the higher field magnitudes. The same RMSE definition, experimental setup and sequence parameters are used as in "Case 1".

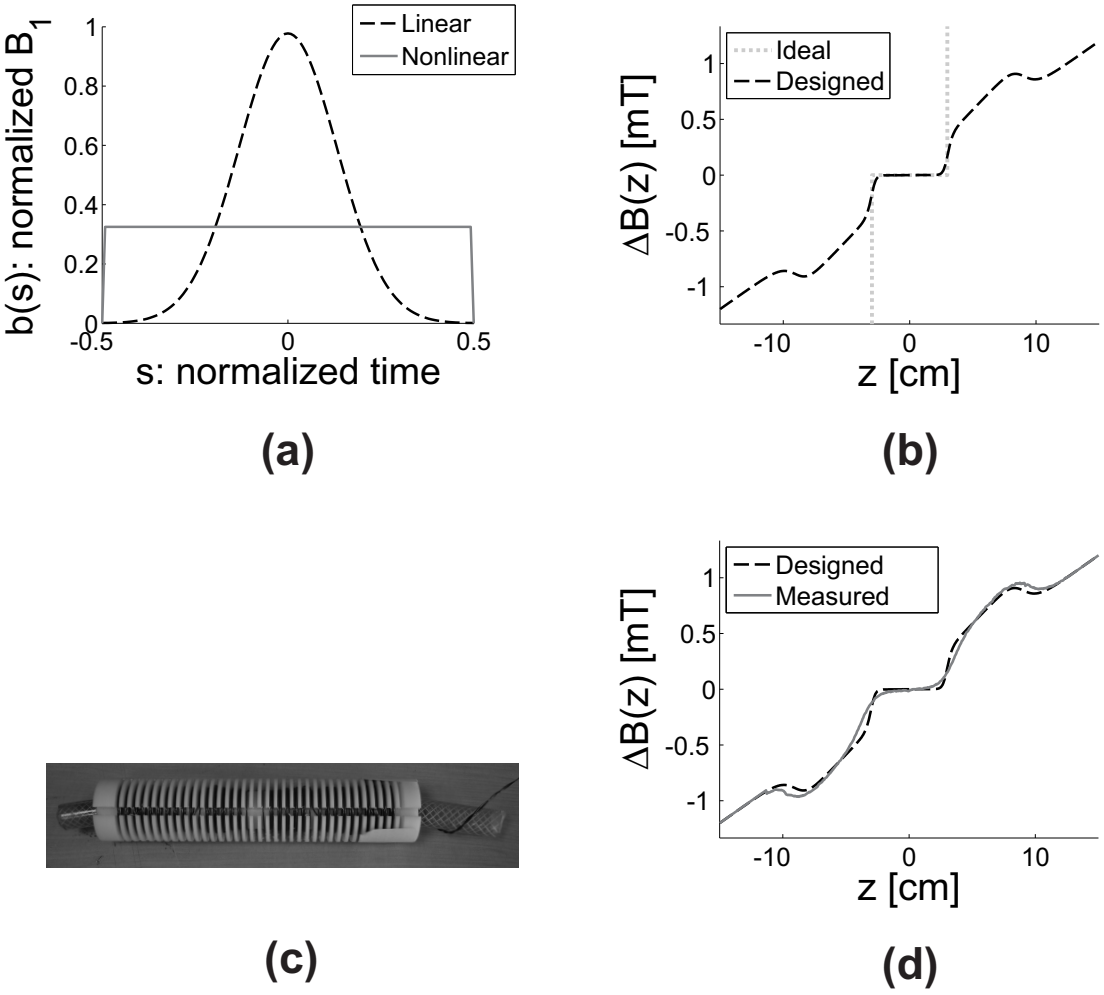

Figure 3.3: The nonlinear gradient field designed to obtain a selective excitation profile when a rectangular RF pulse is applied. **a:** The normalized apodized sinc (time-bandwidth product: 2) and rectangular pulses. **b:** The ideal and the designed fields to obtain a better selective excitation profile with the rectangular RF pulse. **c:** The gradient coil wound on a polyoxymethylene cylinder, and the thin tubular phantom used in the experiment. Coil length: 20 cm, winding separation: 5 mm, winding diameter: 2.4 cm. **d:** The generated field extracted from the distortion in the resulting gradient-echo image by feeding the coil with the phase-encoding signal, compared with the designed field.

3.3.3 Case 3) 3-D: Inhomogeneity Correction using Multi-Dimensional Pulses

In the third example, which is a three-dimensional example, the effect of NLGFs on the SAR is demonstrated in an SAR-intensive multi-spoke excitation scheme. Multi-dimensional pulses are commonly used for tailoring the excitation profile in three dimensions for B_1^+-inhomogeneity correction [27–29]. Although B_1^+-inhomogeneities due to wavelength effects become more pronounced in the ultra-high field regime, they are still evident even at 3T, because the wavelength is 27 cm (assuming a relative permittivity of 80). In this example, we set our desired excitation profile to be a slab with a thickness of 12 cm. However, when a conventional RF pulse is transmitted with the body coil, nearly 30% signal variation can be observed in a 12 cm FOV (Fig. 3.4). To mitigate this inhomogeneity effect, multi-spoke RF pulses are designed.

To demonstrate the effect of using NLGFs on the SAR, a slight nonlinearity is introduced to the z-gradient using a Maxwell pair (Fig. 3.5). Two multi-spoke pulses were designed using (*i.*) the three LGFs and (*ii.*) using the NLGF together with the x- and y-gradient fields. First, by dividing the ideal profile by the inhomogeneity (Fig. 3.4), the desired profile is obtained. It should be noted that the axial cross section of the ideal profile is slightly smaller than that of the phantom. For the regions outside the ideal profile, no correction is performed. Second, the excitation k-space of the desired profile is obtained using Fourier transform. The excitation k-space is sampled by retaining the regions that contain the highest power and discarding the rest. By tracing the sampled excitation k-space using the gradient waveforms, the RF pulse is obtained. Although the scanner used for the experiments can support a 40 $^{\mathrm{mT}}/_{\mathrm{m}}$ field strength, the spoke-gradient field strength was limited to 4.7 $^{\mathrm{mT}}/_{\mathrm{m}}$ to assure that the excitation k-space is sampled sufficiently dense. For all gradients, a 120 $^{\mathrm{mT}}/_{\mathrm{m\cdot msec}}$ slew-rate limit is used. Instead of limiting the total number of spokes, the total RF pulse duration is limited to 2.5 ms. For the NLGF case, the desired profile is first mapped to the nonlinear coordinate system, and the corresponding excitation k-space is subsequently obtained and sampled.

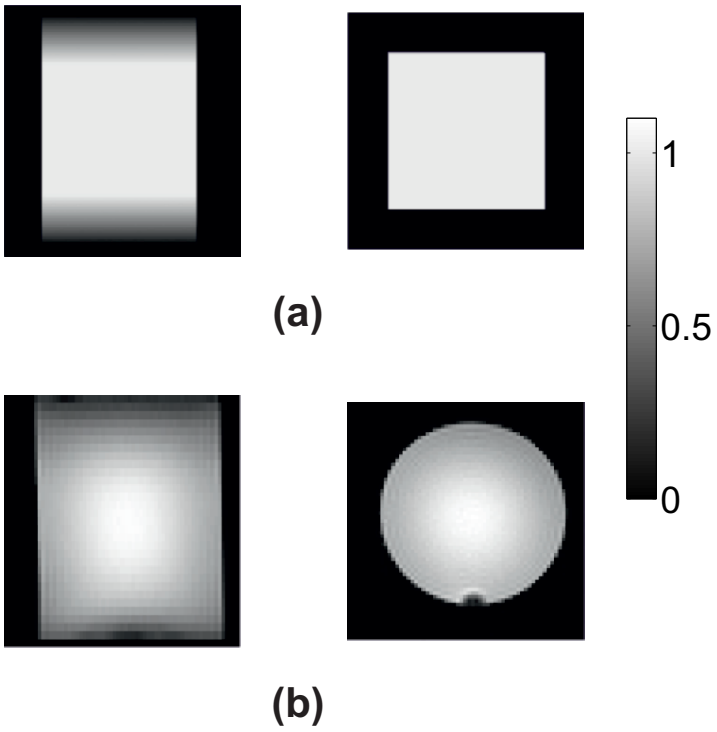

Figure 3.4: The desired and obtained excitation profiles when a conventional excitation pulse is applied. **a:** The desired excitation profile, a slab with a 9 cm long homogeneous region and 1.5 cm long transition regions along the z-direction; the simulation phantom, measuring 10 x 10 x 30 cm^3. **b:** The presence of central brightening effect in the resulting phantom (Model No: 8624186 K2285, Siemens Healthcare, Erlangen, Germany, diameter: 12cm, length: 25cm) images when a conventional excitation pulse is applied. Coronal images (left), FOV: 15 x 16 cm^2. Axial images (right), FOV: 15 x 15 cm^2.

To simulate the expected excitation profile, the inverse Fourier transform is applied to the sampled excitation k-space. Next, the effect of the inhomogeneity is applied to the resulting excitation profile. It should be noted that when the NLGF is used, the profile is mapped to Cartesian coordinates before applying the inhomogeneity. The flip-angle of the expected excitation profile is adjusted to minimize the RMSE in the FOV with respect to the ideal profile. Because the transition regions are encoded but discarded in slab imaging schemes, these regions are not included in the error calculations.

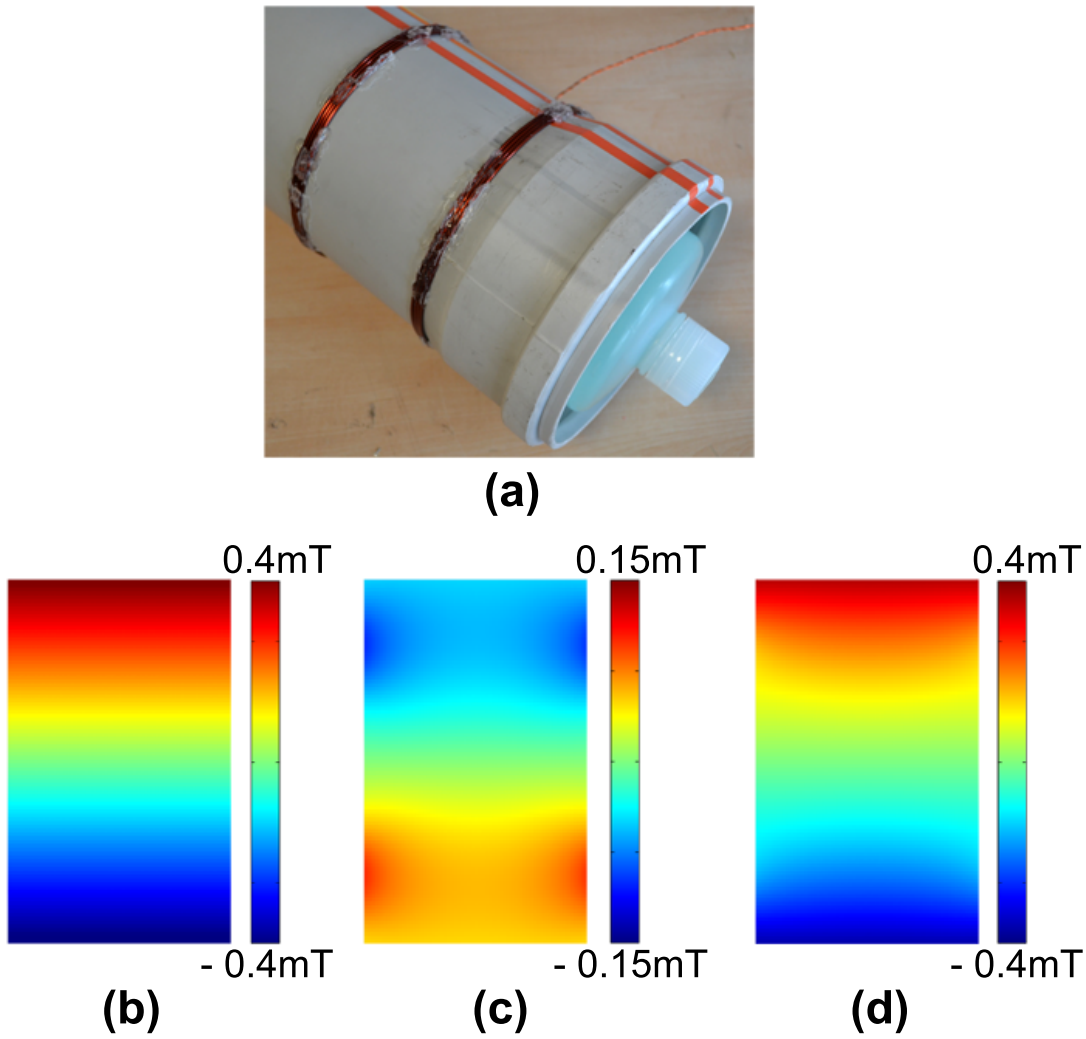

Figure 3.5: The produced Maxwell coil and the simulated linear and nonlinear gradient fields. All fields are given on the coronal plane with FOV: 10 x 16 cm^2 and cylindrical symmetry. **a:** The Maxwell coil, wound on a plastic cylinder with a diameter of 16 cm (two opposite windings of 4 turns each), and the Siemens phantom used in the experiments. **b:** The z-gradient field. **c:** The field generated by the Maxwell pair. **d:** The NLGF obtained by using the Maxwell pair together with the z-gradient.

In the experiments, three-dimensional encoding is performed with readout, phase and section encoding along the x-, y- and z-directions, respectively. The

experimental setup is similar to the previous two cases, but there are three differences: (*i.*) the maximum current required is approximately 1.25A; (*ii.*) because three-dimensional encoding is performed, the x-gradient cannot be disconnected; therefore, the z-gradient waveform is used for driving the custom coil; (*iii.*) because the custom coil distorts the field, it should be switched off during encoding; therefore, a mechanical relay is inserted before the audio amplifier. To account for the RF pulse duration and to facilitate proper switching of the relay, a T_E of 10 ms and a T_R of 100 ms are used. The other parameters are set to the following values: FOV_x x FOV_y x FOV_z, 15 x 15 x 16 cm^3; acquisition matrix, 64 x 64 x 32; flip-angle, 15°. For consistency, both the computational and the experimental results are resampled to 128 x 128 x 96 matrices using linear interpolation.

3.3.3.1 Implementation of VERSE

To observe the effect of the VERSE algorithm on the SAR, either the slew-rate, the maximum gradient amplitude, or the total pulse duration needs to be increased. In this study, we increased the gradient amplitude limit by 10%, 25% and 100% while keeping the slew-rate limit constant. It should be noted that, the last case is slew-rate limited rather than amplitude limited. An iterative approach is used for the VERSE algorithm by reducing the maximum RF threshold by 20% with each iteration and by increasing the number of iterations until the total RF duration is again 2.5 ms.

3.4 Results

3.4.1 Case 1) 1-D: Pulse Design for a Given Nonlinear Field

For the RF pulses shown in Fig. 3.1, the computational and experimental excitation profiles are given in Fig. 3.6. The normalized SAR of the linear case is 2.16 whereas the nSAR is reduced by 15% to 1.85 in the nonlinear case. The

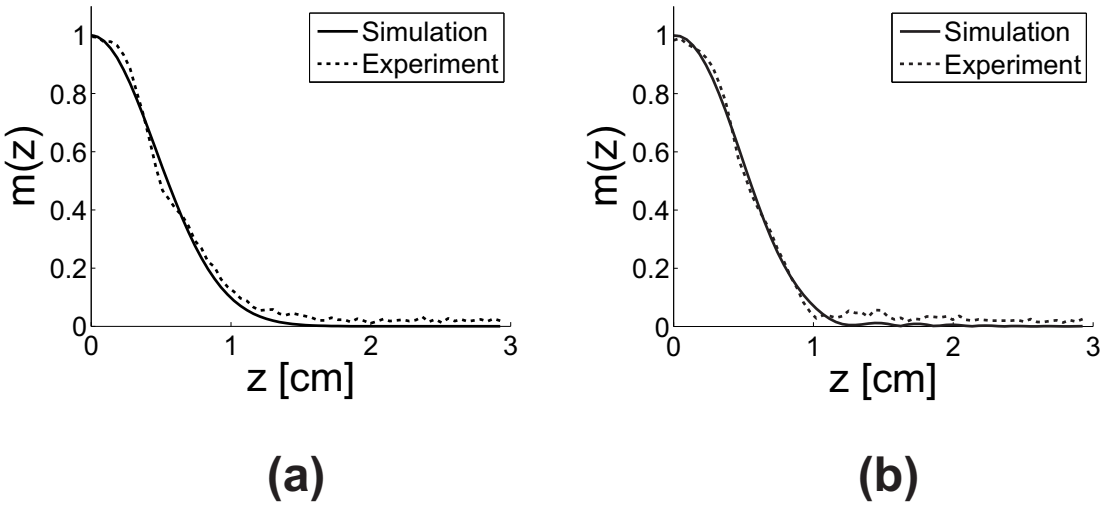

Figure 3.6: Comparison of the excitation profiles obtained using linear and nonlinear gradient fields, for Case 1. **a:** The profiles for the linear case. **b:** The profiles for the nonlinear case. (Due to the symmetry of the profiles, only $z > 0$ halves are given.)

excitation profile for the NLGF case has small oscillations outside the main lobe, which causes an RMSE of 0.5% in the simulations. As expected, slight contractions occur outside the FWHM due to the truncation of the current distribution to 6.4 cm, which increases the RMSE to 1.2%. In the experiments, the RMSE between the LGF and NLGF cases is 2.9%. The RMSEs between the simulations and the experiments are 3.1% (for the linear case) and 3.4% (for the nonlinear case). It can be observed that even with a slight nonlinearity, the SAR can be reduced without affecting the excitation profile.

3.4.2 Case 2) 1-D: Field Design for Optimal SAR Pulses

When the rectangular RF pulse is used (Fig. 3.3), the normalized SAR is reduced by 54% (from 2.16 to 1). The RMSEs between the computational and experimental profiles (Fig. 3.7) are 3.4% (for the linear case) and 4.9% (for the nonlinear case). When the profiles are compared with the ideal profile (Fig. 3.7), the error values for the linear case are 24.5% in the simulations and 25.6% in the experiments; for the nonlinear case, the error values are 13.2% in the simulations and 12.0% in the experiments. In this example, it is clear that the excitation

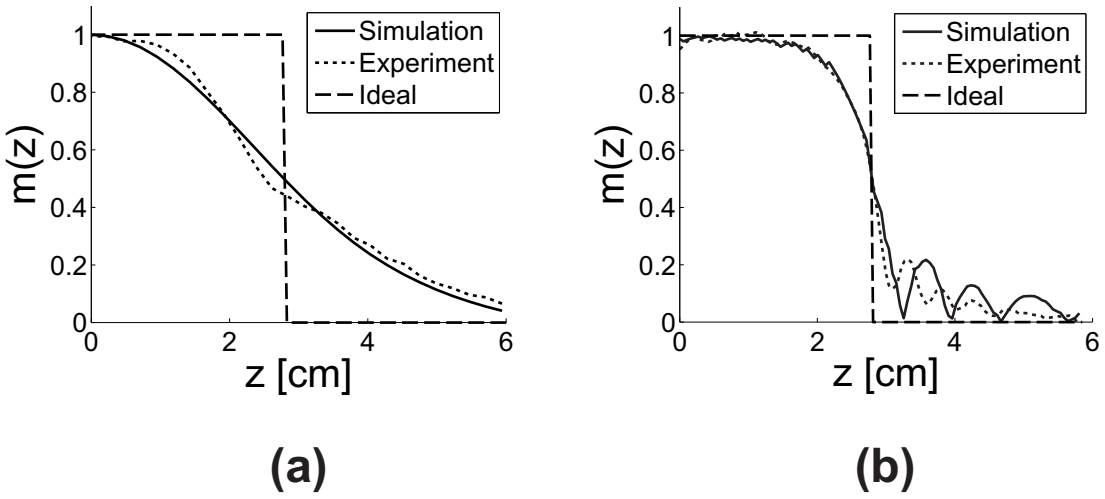

Figure 3.7: Comparison of the excitation profiles obtained using linear and nonlinear gradient fields, for Case 2. **a:** The profiles of the apodized sinc pulse in the presence of the LGF. **b:** The profiles of the rectangular pulse in the presence of the NLGF. In the simulations, the NLGF measured using MRI is used. (Due to the symmetry of the profiles, only $z > 0$ halves are given.)

profile obtained using the rectangular pulse more closely resembles the ideal profile, than the reference solution. To obtain better selective profiles in the linear case, the time-bandwidth (T-BW) product of the sinc pulse can be increased at the expense of higher nSAR. For T-BW values of 4, 6 and 8, the RMSE drops to 21.7%, 17.5% and 15.2%, respectively, while the nSAR increases to 3.1, 5.2 and 7.2, respectively. For a T-BW ≈ 11, the RMSE can be reduced to 13.2%, as in the nonlinear case. However, this T-BW value also results in an increase of the nSAR to 9.8. Therefore, in contrast to the LGFs, NLGFs can significantly reduce the nSAR while obtaining better selective excitation profiles.

3.4.3 Case 3) 3-D: Inhomogeneity Correction using Multi-Dimensional Pulses

Without any correction, although the nSAR is 9.3, the central brightening effect causes an RMSE of 16% in the excitation profile when compared with the ideal profile (Fig. 3.4). When the multi-spoke RF pulse designed for the linear case is used, the RMSE is reduced to 4% (Fig. 3.8); however, the nSAR of the RF pulse

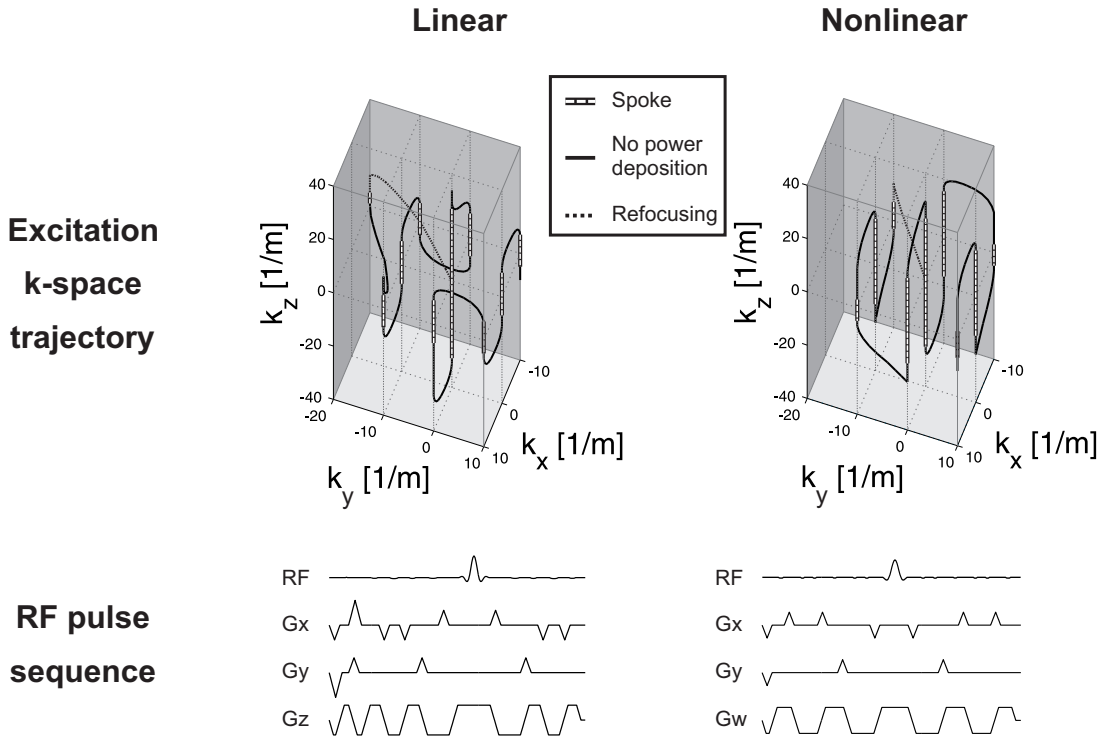

Figure 3.8: *First part of a continued figure.* Comparison of the excitation k-space trajectories, RF pulses and the corresponding excitation profiles obtained for the linear and nonlinear cases. Because of finite gradient slew-rate, the excitation k-space trajectories extend beyond the spokes along the k_z direction.

is 110.9. For the NLGF case, the nSAR is reduced by 26% to 82.6, although the RMSE is slightly increased to 5%.

When the VERSE algorithm is implemented by increasing the maximum gradient amplitude by 10%, 25% and 100%, the nSAR values are reduced to 70, 40 and 25.5, respectively, for the LGF case and 42.6, 24.2 and 15.3, respectively, for the NLGF case (Fig. 3.9). Hence, the nSAR is 39-40% lower for the NLGF case. It should be noted that, the VERSE algorithm is assumed not to affect the excitation profiles (i.e., it is assumed that no off-resonance effects exist) since such effects are not in the scope of this dissertation.

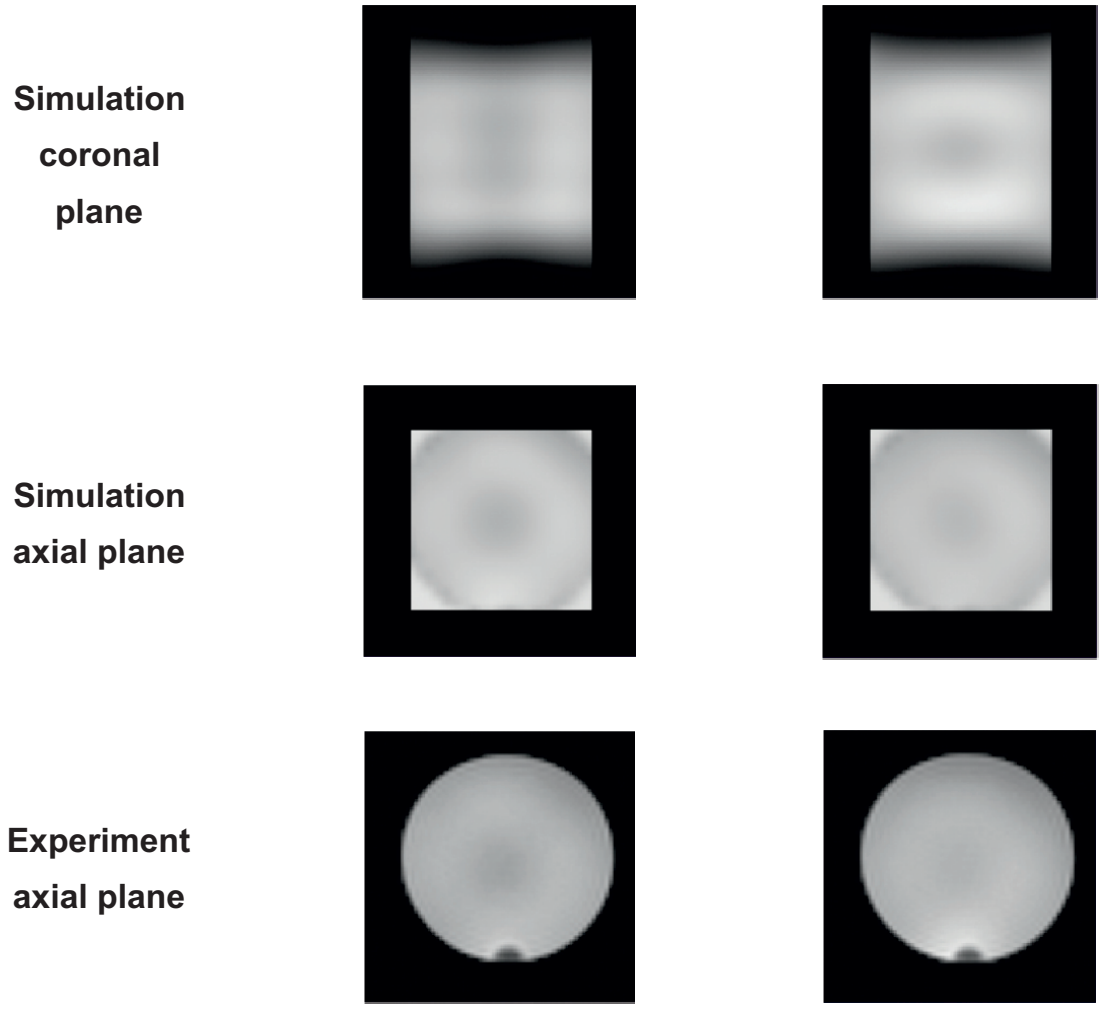

Figure 3.8: *Second part of a continued figure.* Comparison of the excitation k-space trajectories, RF pulses and the corresponding excitation profiles obtained for the linear and nonlinear cases. Because of finite gradient slew-rate, the excitation k-space trajectories extend beyond the spokes along the k_z direction.

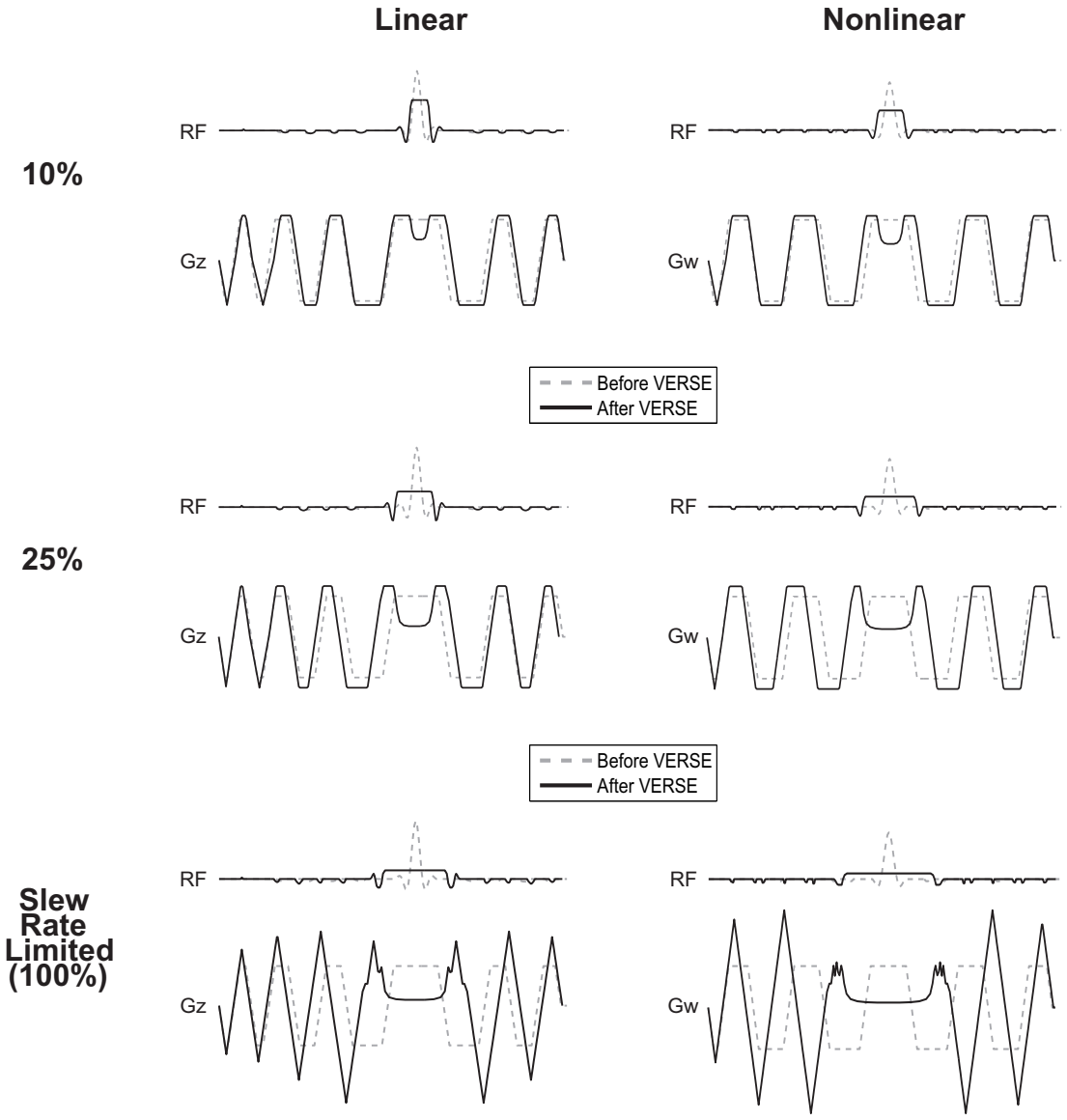

Figure 3.9: Comparison of the RF pulses for the linear and nonlinear cases when the VERSE algorithm is implemented. To implement the VERSE algorithm, 10%, 25% and 100% increases in the maximum gradient amplitude are allowed.

3.5 Discussion and Conclusion

In this dissertation, a new SAR reduction method is introduced that employs nonlinear gradient fields (NLGFs). To compare various RF pulses designed with linear and nonlinear gradient fields, the normalized SAR (nSAR) is defined. Using three example cases, SAR reductions between 15% and 54% are shown in both simulations and experiments.

Conventional MRI imaging strategies assume perfectly LGFs; therefore, the reduction of any imperfections in the LGFs has been studied extensively. However, some nonlinearities always exist. For this reason, many algorithms that correct the effects of such nonlinearities on the images are implemented in commercially available scanners. As demonstrated, such nonlinearities may be useful in terms of the SAR. In the first example case, a slight sinusoidal nonlinearity was assumed to exist with the LGF, and the SAR was reduced by 15%.

The commonly used selective excitation pulses, such as apodized sinc envelopes, are far from optimal in terms of the SAR. In fact, we demonstrate that such pulses may have more than twice the minimum SAR value, which holds for a rectangular pulse. However, the excitation profile of a rectangular pulse does not provide sufficient selectivity, limiting its use in MRI. With NLGFs, we demonstrate that the excitation profile of a rectangular pulse can be transformed into a selective profile that also yields the lowest possible SAR.

Multi-dimensional pulses significantly increase the SAR. The nSAR of the multi-spoke pulse designed with the LGFs was more than two orders of magnitude higher than that of a rectangular pulse. However, the SAR can be significantly decreased with NLGFs. In the third example, the SAR was reduced by approximately 26%, to 40%. It should be noted that the NLGF used for this example was selected for its simplicity, meaning that it does not imply a limit on the reduction in the SAR. A nonlinear gradient field that shows higher compatibility with the desired excitation profile than the field used in the example may yield a higher reduction in the SAR. With the implementation of the VERSE algorithm, the SAR of both the linear and nonlinear gradient field cases was reduced. However,

with VERSE implementation, the SAR of the nonlinear gradient case was nearly 40% lower than that of the linear case in all demonstrated cases.

In the third example, a gradient coil with a diameter of 16 cm was used with a maximum current of 5 amperes (4 turns $\times$ 1.25A). Although the size and the low-current requirement hint at the applicability of the proposed technique to extremity and head imaging with slightly larger dimensions, the extension of the approach to whole-body MRI needs further investigation because it is known that the power demands from the gradient amplifiers scale with the fifth power of the coil diameter [75]. However, in-vivo MRI applications of nonlinear gradient fields have previously been used for encoding during head MRI [76].

When NLGFs are used, the reduction in the SAR depends on the compatibility of the NLGFs and the desired excitation profile. Therefore, the optimal field may vary for different applications. However, sometimes the optimal NLGF may be too demanding from a hardware standpoint, or it may require impractical coil dimensions. Therefore, a trade-off exists between the SAR reduction and the feasibility of achieving that reduction.

Because the SAR depends on the compatibility of the shape, position, orientation and thickness of the excitation profile, certain NLGFs may increase the SAR, as well. In such a case, if the LGFs are still available along with the NLGFs, the SAR-optimal pulse would use only the LGFs, preventing any increase in SAR. Therefore, when NLGFs are available along with some linear counterparts, any excitation profile can be obtained, and the SAR may only be lower than the linear case.

The use of NLGFs alters the well-known Fourier transform relationship that exists between the excitation profile and the excitation k-space in the small-tip-angle regime. When NLGFs are used, the Larmor frequency of spins varies nonlinearly in space, and the kernel of the Fourier transform becomes a function of the nonlinear field distribution. In this case, RF pulses can be designed with NLGFs either with this nonlinear Fourier transform or by defining a nonlinear coordinate system to obtain the well-known linear form of the Fourier transform. Because the kernel changes (in the former approach) or the excitation profile changes (in

the latter approach), the excitation k-space and the RF pulse are altered, leading to the change in the SAR. It should be noted that similar approaches can be applied at the large-tip-angle regime, as well. For example, NLGFs can be used for designing large-tip-angle pulses with the Cayley-Klein parameterization algorithm [24] by expressing the excitation profile in a nonlinear coordinate system or incorporating the nonlinear field variation in the Cayley-Klein parameters. However, further investigation of the applicability of this method is needed.

The optimization of MRI and its applications is a complex problem with many design goals, including the reduction of the SAR, the reduction of the scan time, the increase of the resolution, the increase of the signal-to-noise ratio and the increase of the field homogeneity. We believe that by combining various approaches to solving this problem, such as B_1^+-shimming, multi-dimensional excitation pulses, variable-rate selective excitation, encoding using nonlinear gradient fields and coil design, significantly different imaging schemes can be designed that not only better suit the desired region-of-interest or the goal of examination but also increase the efficiency in terms of imaging time, global SAR and local SAR.

Chapter 4

Scan Time Reduction using Nonlinear Gradient Fields

Preface

The content of this chapter was presented in part at the Scientific Meetings of International Society of Magnetic Resonance in Medicine [77] and Turkish Society of Magnetic Resonance [78].

4.1 Introduction

A typical MRI experiment consists of three steps; excitation of the spins, encoding of the spatial information, and signal acquisition. In its simplest form, a three-dimensional imaging experiment includes successive application of these steps, with spatial encoding along three directions. However, because of the sequential nature of MRI, such an approach may become impractically long. Furthermore, the ROI is smaller than the whole-object for many applications. However, by performing the spatial encoding along one of the three directions simultaneously with the signal acquisition, total imaging time can be reduced; this encoding

step is called readout or frequency encoding. The FOV can be reduced along this direction by band-pass filtering during post-processing. On the other hand, applying spatial encoding simultaneously with excitation localizes the excitation region along the encoding direction; this is called selective excitation. Using this approach, the FOV can be reduced in the encoding direction to thick or thin regions; the former is called slab selection whereas the latter is called slice selection. Traditional MRI methods employ both selective excitation and frequency encoding in order to reduce the FOV and hence, slice imaging (2D-imaging) can be performed rapidly. However, the ROI is thicker than a single slice for many applications in MRI. Although such a sub-volume can be imaged using a series of slice images, slab imaging (3D-imaging) yields superior signal-to-noise ratio. Although slab imaging suffers from physical motion of the subject more since the effect of motion artifacts is blurring as opposed to misalignment between the images that is seen in slice imaging, both methods benefit from further reductions in total scan time. As a result, many studies have been proposed to reduce the FOV in MRI.

First of these techniques is based on RF hardware. By using RF coils with spatially varying sensitivity profiles, the FOV can be reduced. Although this approach may be useful for tissues close to the coil, its effectiveness drops for deep structures in the body. Furthermore, since coil sensitivities generally vary smoothly in space, sufficient selectivity may not be always possible to achieve. Therefore, efficiency of RF hardware base methods depends on the application.

The second approach is to use specifically designed RF pulses to reduce the FOV. For this purpose, refocusing or saturation pulses can be used for focusing the excitation along more than a single dimension [32, 79]. However, additional RF pulses are required in this approach, which in turn increase both the SAR and the excitation duration. Although the increase in SAR can be accommodated at lower field strengths, the SAR regulations become more restrictive at higher field strengths due to the quadratic dependence of SAR on the field strength (Section 2.7, [47]). On the other hand, the increase on the total excitation duration may increase the repetition-time for rapid imaging sequences such as the fast low-angle shot (FLASH) sequence. Furthermore, an increase in the pulse duration may

increase the echo-time or force the usage of spin-echo sequences. An alternative approach to refocusing and saturation pulses is to use multi-dimensional spatially selective excitation pulses (MD-pulses) [33]. Unlike refocusing and saturation pulses, MD-pulses can tailor the excitation profile to non-Cartesian regions as well. However, this method also suffers from the increased SAR and RF pulse duration, similar to refocusing and saturation pulses. Hence, RF pulse based FOV reduction methods may not be as effective, for the applications where the increases in the SAR and the echo-time cannot be accommodated.

The third approach is based on the gradient fields. As mentioned previously, conventional MRI techniques employ linear gradient fields (LGFs). When LGFs are used, the field varies in a single direction, thereby providing localization along only one direction. However, because of the field curvature at low frequencies, any nonlinear gradient field (NLGF) varies along at least two directions. Therefore, the excitation profile can be localized in two or three directions when a nonlinear gradient field is used. Researchers have suggested using NLGFs for excitation followed by a selective refocusing pulse [35, 36] and using LGFs for excitation followed by an NLGF for dephasing of outer volumes [37] as means of FOV reduction. While the former approach still has an additional RF pulse, and therefore higher SAR, the latter method does not increase the SAR. However, the additional RF pulse of the former method and the gradient pulse of the latter method still result in an increase in the echo-time. Therefore, NLGF methods in the literature may require at least longer echo times to be effective.

In this study, we propose a 3D imaging method that employs NLGFs for excitation of inner volumes, without changing the SAR or the echo-time. The method uses NLGFs during the excitation to yield an excitation region with curved boundaries. Then, reduced-FOV encoding is performed. In this case, the aliasing artifacts fold into the encoded-FOV (FOX) since the FOX is smaller than the excitation FOV. However, with a careful selection of the nonlinear gradient field, these artifacts fold into the outer sections of the FOX, thereby leaving the central portion of the image free from any artifacts. Furthermore, the artifacts are along the readout direction, which makes it possible to remove these artifacts from the image using band-pass filtering during either the acquisition or the

post-processing steps. The method is demonstrated using simulations and initial in-vivo volunteer experiments.

4.2 Theory

At the small-tip-angle regime, the transverse magnetization formed after an RF pulse with duration τ is given by the following:

$$\mathcal{M}(\mathbf{x}) = i\gamma M_0(\mathbf{x}) \int_{-\tau/2}^{\tau/2} B_1(t) e^{i\gamma \int_0^t \Delta B(s;\mathbf{x}) ds} dt \tag{4.1}$$

$$= i\gamma M_0(\mathbf{x}) m(\mathbf{x}) \tag{4.2}$$

where $M_0(\mathbf{x})$ is the magnetization density of the subject, $\Delta B(s;\mathbf{x})$ is the perturbation in the static magnetic field (caused by the gradient fields), and $m(\mathbf{x})$ is the excitation profile. Note that, complete refocusing is assumed in Eqs. (4.1)-(4.2). In conventional MRI methods, linear gradient fields that are driven using trapezoidal waveforms are used for excitation to localize the excitation along one direction. Therefore, during the RF pulse, the field perturbation is given by $\Delta B(s;\mathbf{x}) = sG_z z$ where, the localization direction is assumed to be along the z-axis without loss of generality. In such a case, the excitation profile becomes the following:

$$m(\mathbf{x}) = \int_{-\infty}^{\infty} B_1(t) e^{i2\pi f(z)t} dt \tag{4.3}$$

where $f(z) = \frac{\gamma}{2\pi} G_z z$. Note that in Eq. (4.3), the limits of the integral are extended to infinity using the fact that the RF pulse is zero outside its duration, τ. It can be seen from Eq. (4.3) that, the excitation profile depends only on z, i.e., $m(\mathbf{x}) = m(z)$. Hence, the extent of the transverse magnetization and therefore the FOV in the transverse plane is determined solely by the object size, when a linear gradient field is used.

When a nonlinear gradient field is used during excitation, the field perturbation depends on at least two directions. Therefore, the extent of the transverse magnetization, and therefore the FOV, is determined not only by $M_0(\mathbf{x})$, but also

by $m(\mathbf{x})$. As a consequence, the aliasing artifacts that occur when the FOX is smaller than the FOV, are affected by the field distribution.

4.3 Methods

In order to demonstrate the effect of field nonlinearity on the aliasing artifacts, two example cases will be presented in the following sections. In the first case, the effect of the field nonlinearity on the folding artifacts will be demonstrated for a loop coil, using simulations. In the second case, the A20 shim coil of the MRI scanner, which has a $z^2 - x^2/2 - y^2/2$ variation in space, will be used for excitation in volunteer scans. For these examples, the simulations are performed in Matlab (The Mathworks Inc., Natick, MA, USA) whereas the experiments are performed using a 3T MRI scanner (MAGNETOM Trio a Tim System, Siemens Healthcare, Erlangen, Germany). The volunteer experiments are performed after approval of the local ethics committee and informed consent of the volunteer.

4.3.1 Case 1: Reduced-FOV Imaging using a Loop Coil

The simplest coil structure that creates a linear magnetic field is the Maxwell pair, which consists of two loop coils. Although the gradient fields used in MRI require more complex structures to produce the high homogeneity needed, the loop coils are still the building blocks for the z-gradient coils. Therefore, we will demonstrate the effect of using a nonlinear gradient field on the aliasing artifacts for a loop coil in this section.

For this purpose, a loop gradient coil with a radius of 20 cm, which is driven with a current of 30 A is assumed. When an ideal sinc RF pulse with first zeros at ± 2.5 ms is used for excitation, the resulting excitation profile is as shown in Fig. 4.1a. It can be seen that, the varying field limits the excitation to a thickness of 12 cm in the plane of the coil (the transverse plane). However, the excitation region extends to a thickness of 36 cm along the horizontal direction, when the

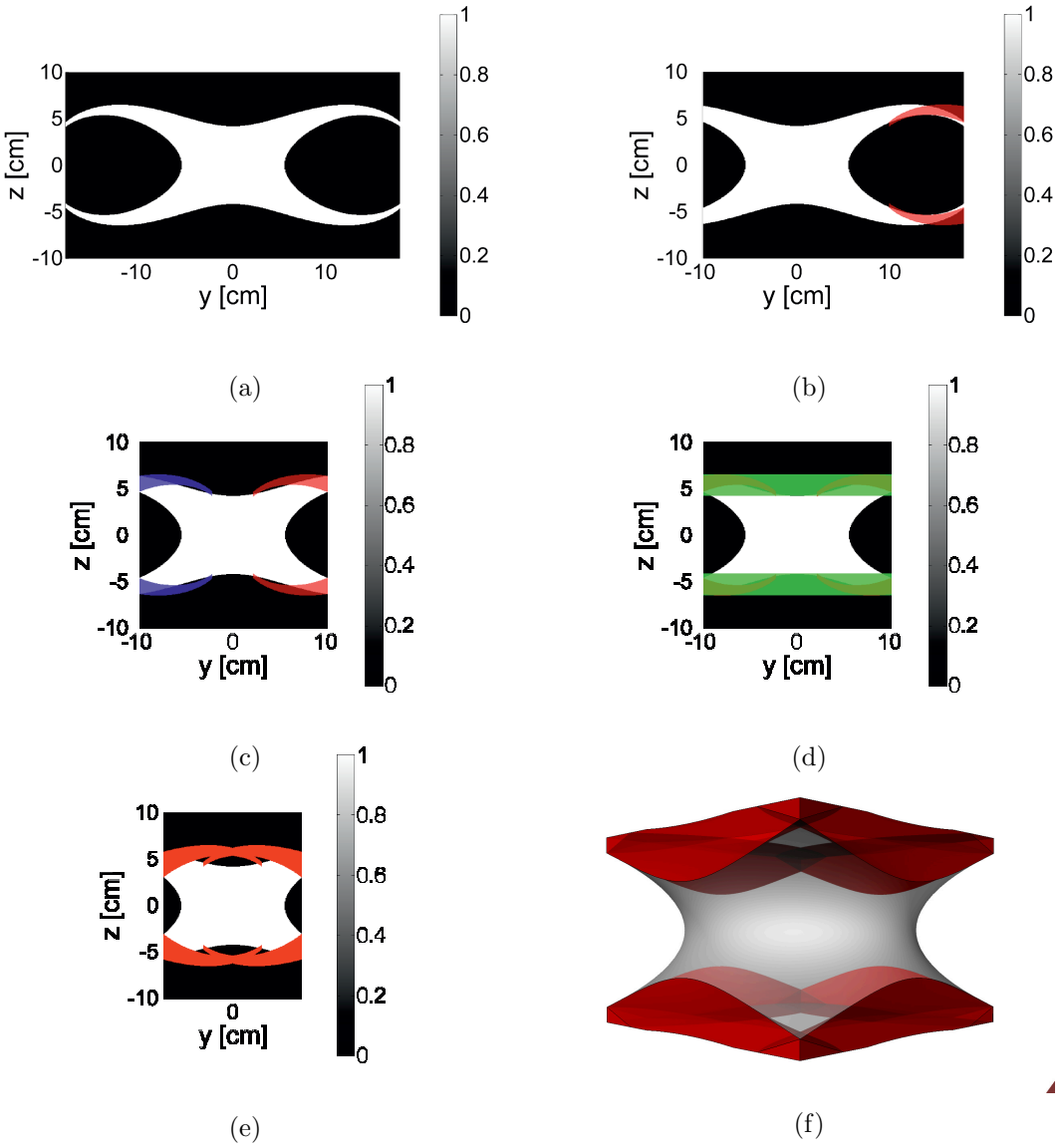

Figure 4.1: The excitation profile obtained with a *sinc* RF envelope in the presence of the field of the loop coil, for various FOXs. The loop coil lies at the transverse plane and has a radius of 20 cm. **a:** The excitation profile, when the FOX is $36 \times 36 \times 20$ cm^3. The excitation profile is cylindrically symmetric. **b:** When the FOX is reduced by 8 cm from the left of the image, aliasing occurs, as indicated by the red-shaded region. FOX: $28 \times 36 \times 20$ cm^3. **c:** When the FOX is reduced to 20 cm along the y-axis, aliasing artifacts enter the FOX from both left (blue shaded region) and right (red shaded region) sides of the image. FOX: $20 \times 36 \times 20$ cm^3. **d:** When the FOX is reduced to 20 cm along the y-axis, all aliasing artifacts are inside the green-shaded region, which holds when the FOX is reduced along the x-direction as well. **e:** The FOX can be further reduced; in this case the FOX is 15 cm along the y-axis and the aliasing artifacts are shaded red. **e:** The FOX can be reduced in both transverse directions. The aliasing artifacts (red regions) leave a region at the center that is free from any artifacts (gray shaded region).

whole FOV is considered. Because of the nonuniform extension of the excitation profile in the transverse plane, the FOX can be reduced without aliasing artifacts in certain regions. When the FOX is cropped by 8 cm from the left, the extension of the excitation region aliases into the right half of the image (Fig. 4.1b). Furthermore when the FOX is reduced to 20 cm, both of the extensions on the left and the right portions of the image alias towards the central region of the image (Fig. 4.2c). Since the aliasing artifacts occur only in the two bands indicated in Fig. 4.2d, the white shaded region at the center is free from any artifacts. The FOX can be further reduced as shown in Fig. 4.1e, in which case, the FOX is 15 cm. Furthermore, the same reduction of the FOX can be made in the orthogonal transverse direction simultaneously as well, in which case, the FOX is as shown in Fig. 4.1f. It can be seen that, the FOX can be reduced when a loop gradient coil is used, without any aliasing artifacts in the central region of the image.

4.3.2 Case 2: Reduced-FOV Imaging Using a Second Order Shim Coil

In this section, the effect of a nonlinear excitation gradient field on the aliasing artifacts is shown with a volunteer experiment. For this purpose, one of the shim coils of the scanner is used. The aim of the experiment is to image a $8 \times 8 \times 10$ cm^3 region around the cerebellum and the occipital lobe of the brain, with a resolution of $1.2 \times 1.2 \times 1.2$ mm^3. Note that, the numbers are arbitrarily defined for the proof-of-concept demonstration.

In commercially available MRI scanners, special gradient coils, which are called shim coils, are used to increase the homogeneity of the static magnetic field, B_0. However, these coils are continuously driven, and no real-time control of these coils is possible for most scanners. In this example, the current of one of the shim coils is altered in order to obtain a nonlinear magnetic field inside the scanner. For the scanner used in the experiments, the field of the A20 coil, which has a $z^2 - x^2/2 - y^2/2$ distribution in space, can be altered between ± 1300 $\mu\text{T/m}^2$. It is well known that for the same excitation profile, as the gradient field strength

increases, the bandwidth of the required RF envelope increases, and hence, the duration of the RF pulse decreases. In order to reduce the RF pulse duration as much as possible, the current of the shim coil is maximized. The default field value is approximately 6 μT/m^2, therefore, both 1300 μT/m^2 and -1300 μT/m^2 are possible choices. It should be noted that, when positive field values are used, the fat tissues that lie outside the region-of-interest in the transverse plane may be excited; this may prevent the reduction of the FOX. Hence, -1300 μT/m^2 value is chosen as the nonlinear magnetic field strength for the experiments.

In the experiments, a gradient echo sequence that was obtained from the manufacturer of the scanner is used (Siemens Healthcare, Erlangen, Germany). The default RF envelope of the sequence, which is a sinc pulse apodized with a Hanning window, is used without any modification, other than setting the time-bandwidth product of the pulse to 2. It should be noted that, the maximum field generated by the shim coil is lower than that of the linear gradient coils (40 mT/m). Therefore, the duration of the RF pulse is increased to 20 ms, in order to reduce the thickness of the excitation region along the head-foot direction to 10 cm. To accommodate the increase in the RF pulse duration, the echo-time was increased to 35 ms. In the experiments, a single k-space line is acquired at each repetition. Therefore, the repetition-time was reduced to 80 ms to keep the scan as short as possible, for the sake of the volunteer. Note that, when the shim field is used singlehandedly, the excitation profile is centered at the center of the scanner and hence, at the center of the brain. In order to shift the excitation profile to the posterior region of the brain, linear gradient fields, and proper frequency offsets are used. The flip-angle is set to 15°, and 3D encoding is used. The FOX is set to $10 \times 8 \times 21$ cm^3 and the readout is performed along the head-foot direction. When imaging the same region with linear gradient fields, the same RF pulse sequence is used, however, the shim settings are reset to the default values and the slab selection is performed with the z-gradient field. To prevent aliasing artifacts, the FOX is set to $18 \times 23 \times 10$ cm^3 and to make a fair comparison between the two methods, readout is performed along the longest dimension of the volunteer's head (anterior-posterior direction). The comparison between the two methods will be presented in the next section.

4.4 Results

For the loop coil example, the FOX was reduced by 58% in the right-left direction without any aliasing artifacts inside the central region. Furthermore, another 58% reduction in the direction not shown could be made because of the cylindrical symmetry of the excitation profile. However, the aliasing bands at the upper and lower portions of the image also need to be encoded along the readout direction, which increases the FOX along that direction by 55%. Therefore, the total imaging volume is reduced by 72%.

For the volunteer experiment, four section images are shown in Fig. 4.2. When the proposed method is used instead of the conventional linear gradient approach (images not shown), the total scan time is reduced by 60%.

4.5 Discussion

In this study, a new FOV reduction method, which uses nonlinear gradient fields for excitation, is proposed. It is demonstrated that, when nonlinear gradient fields are combined with conventional excitation pulses, the aliasing artifacts that occur when the encoded-FOV is smaller than the excitation-FOV, can be kept outside the region-of-interest. These artifacts, which fold into outer sections of the image along the readout direction, can be filtered out by simple band-pass filtering techniques at the post-processing stage. The advantage of the method, compared to other techniques that utilize multi-dimensional excitation, saturation or refocusing pulses such as the Local-Look technique [79] or that dephase outer volumes using NLGFs [37], is that no additional RF or gradient waveforms are required, and hence the echo-time and the SAR are kept unchanged. The method is demonstrated using volunteer experiments, in which case the total scan time is reduced by 60%.

In the volunteer experiments, one of the shim coils of the scanner is used. Because the maximum field that the coil generates is much smaller than the field

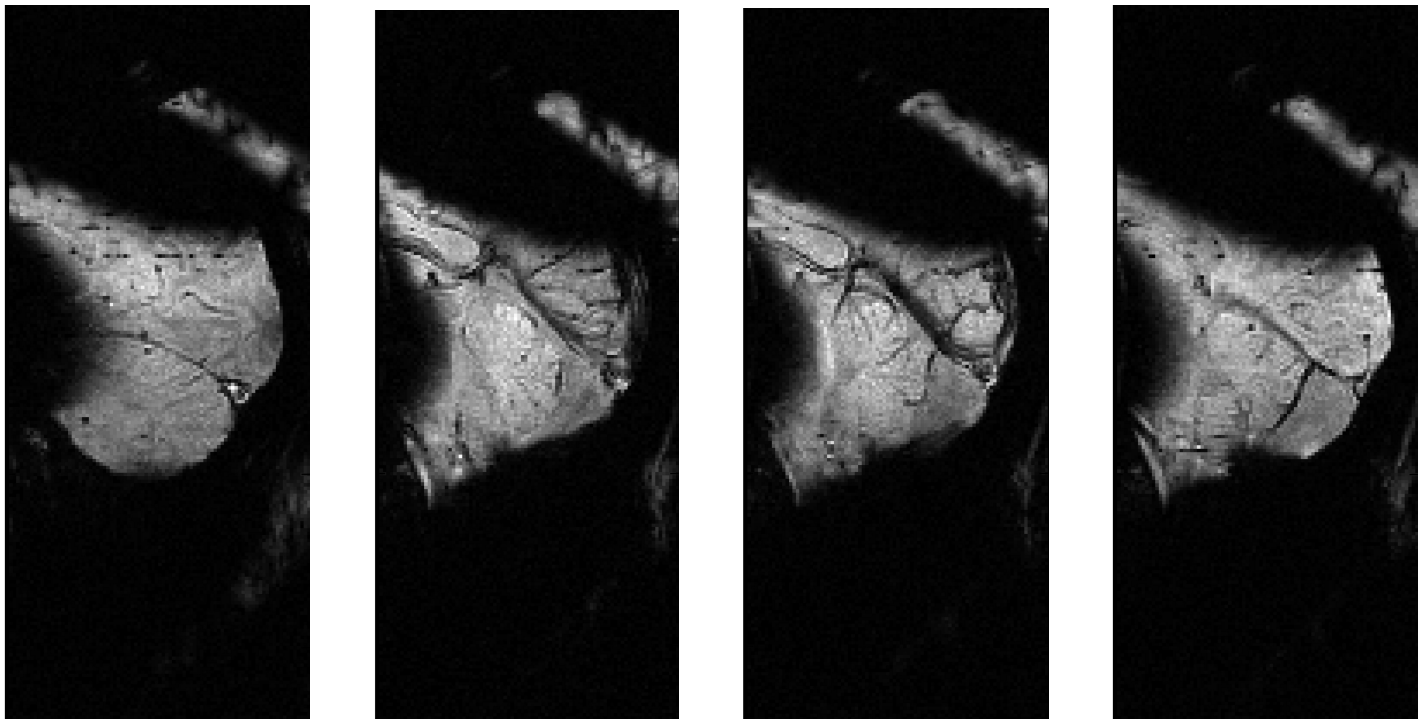

(a) (b) (c) (d)

Figure 4.2: Four different sagittal section images obtained in the volunteer experiment are shown.

generated by the LGF coils of the system, the RF pulse duration was increased to reduce the thickness of the excitation region. Therefore, the echo-time was also increased, which led to T_2^*-weighting (the weighting due to the dephasing of the transverse component of the magnetization, caused by spin-spin interactions and off-resonance effects, see Section 2.3 and reference [48]) in the images. Furthermore, because the current of the shim coil cannot be controlled in real time, the NLGF was always present, which caused dephasing of the spins (Section 3.3.1). However, by reducing the resolution, the effects of the dephasing was reduced. On the other hand, only a single line in the k-space was acquired with each T_R. In order to shorten the scan, the repetition-time was reduced, which caused T_1-weighting (the weighting due to imperfect recovery of the longitudinal component of the spin, see Section 2.3 and reference [48]) in the images. However, the increase in the echo-time, the dephasing, and the co-existing relaxation effects are not the restrictions of the method, but rather the limitations of the implementation. With a real-time controlled and high strength NLGF, and turbo-acquisition sequences as in conventional methods, these limitations can be lifted and the only change in the conventional scheme (sequence and hardware) would be to use the NLGF instead of the LGF, therefore leaving the echo-time and the SAR unchanged.

The effectiveness of the proposed method depends on the compatibility between the nonlinear gradient field, and the region-of-interest. In the given two examples, the method is proposed for a loop coil and a second-order field, and the field-of-view is reduced in the transverse plane. In this case, the central region of the excitation profile is free from aliasing artifacts. On the other hand, when the A20 field is used for excitation, and the FOX is reduced on the $z = \frac{x}{\sqrt{2}}$ plane, aliasing artifacts would fold into the central region, and therefore may inhibit reduced-FOV imaging. Alternatively, let us assume that a third order field with distribution $z^3 - 3zx^2/2 - 3zy^2/2$ is used for excitation, and the FOV is reduced in the transverse plane. In this case, the extension of the excitation profile in the transverse plane (i.e., $z = 0$) would fold into the FOX and cause a band of aliasing artifacts at the center. However, two sub-volumes of the central region of the excitation region, that are above and below the aliasing band along the

z-direction, would remain free from any artifacts. Therefore, the compatibility of the NLGF with the region-of-interest should be carefully evaluated. However, it should be noted that, the compatibility of the field with the ROI does not necessarily improve with increasing field complexity. As it can be seen from the comparison of the excitation profiles of the loop coil and the A20 harmonic, it can be seen that, the aliasing artifacts in the case of the loop coil extend less along the z-direction. Therefore, the longest dimension of the FOX is not necessarily the z-direction, which suggests that the readout encoding can be performed in another direction, which may reduce the total scan time.

When nonlinear gradient fields are used, the thickness, location and orientation of the excitation region are non-trivial to alter. For the field used in the volunteer experiment, since the field has an analytic distribution in space, i.e., $z^2 - x^2/2 - y^2/2$, the excitation region could be shifted using linear gradient fields and a proper Larmor frequency adjustment. Furthermore, the thickness of the excitation region can be altered without changing the shape of the excitation profile. However, changing the orientation of the excitation requires other second-order field distributions. On the other hand, for the loop coil, the thickness of the excitation region cannot be changed without changing the shape of the excitation region, unless the loop is scaled in the same ratio as the thickness. Furthermore, shifting the excitation region may require other field distributions. Although these non-trivial properties may hinder the applicability of nonlinear gradient fields, possible solutions exist such as having a number of basic coils, and generating the desired field distribution by driving these coils separately [80].

4.6 Conclusion

In this study, a new FOV reduction method is proposed. The method employs nonlinear gradient fields together with a conventional RF excitation pulse, in order to partially localize the excitation region along more than a single direction. As demonstrated, when this partial localization is combined with a proper selection of the readout encoding direction, the aliasing artifacts that occur when the

FOV is reduced fold into outer sections of the image, and hence, can be discarded with post-processing techniques. The significance of the method is that the FOV and hence the total scan time can be reduced without changing the SAR or the echo-time.

Chapter 5

Curved Slice Imaging using RF Encoding

Preface

The content of this chapter was presented in part at the Scientific Meeting of International Society of Magnetic Resonance in Medicine [81].

5.1 Introduction

In nearly all MRI applications, gradient coils are used for spatial encoding. Because the employed gradient fields have linear field distributions in space, excitation regions and the FOV are limited to rectangular regions. However, in a considerable fraction of MRI applications, the ROI is merely a portion of the selected slice, and has a non-rectangular shape. Furthermore, some regions may be better imaged, when the voxel shapes are non-rectangular and sizes are not uniform, which cannot be achieved with linear gradient fields. Therefore, a method that can image a non-rectangular region using nonuniform and non-rectangular voxels may increase the efficiency of imaging and thereby reduce the total scan

time.

Multi-dimensional excitation pulses [26–28, 30, 33] provide the ability to specify the excitation pattern in three-directions (Section 3.4.3). Therefore, a certain region can be excited and the FOV can be decreased, using multi-dimensional excitation pulses. However, due to the fact that the FOV still needs to be rectangular when linear gradient fields are used for encoding, this method is useful if the ROI is rectangular too. If the ROI is convex, or encloses a region which is not of interest, the efficiency of the method is still low.

When an RF coil is employed for flipping the spins inside the subject, the phase distribution of the RF coil is imposed on the spins. However, when the same coil is used for reception, the sign of the phase distribution is reversed. Therefore, the resulting images do not have any phase variations caused by the coil, when it is used for both transmission and reception. However, when different coils are used during transmission and reception, the resulting images will have the difference information of the phase distributions of the coils. By altering the phase distribution of the coils that are used for imaging, encoding can be accomplished without using gradient coils [43, 44, 82–85].

In this study we propose a novel encoding scheme that can excite and image curved slices, in order to reduce the requirement of encoding regions outside the ROI, with the purpose of enabling lower scan times. The proposed method uses multi-dimensional excitation pulses to excite a non-rectangular region and uses RF pulses to encode the data instead of gradient coils [43, 44], and hence the FOV is not limited to a rectangular region and the curved slice can be imaged using non-rectangular and nonuniform voxels.

5.2 Theory

It is known that at the small-tip-angle regime, the required RF pulse is the Fourier transform of the desired excitation profile. Therefore, *sinc* envelopes are widely used as RF pulses, for the excitation of slices or slabs. It has been shown that,

the same approach can be used for excitation regions that vary in more than a single direction as well, i.e., by tracing the three-dimensional excitation k-space, the excitation profile can be specified along all three directions [26–28, 30, 33]. Let us assume that, the region-of-interest is expressed in terms of the Cartesian coordinates by $f_{ROI}(\mathbf{x})$, where $\mathbf{x} = [x \;\; y \;\; z]$. Then, the excitation k-space that is required to excite the desired ROI is the Fourier Transform of this ROI function, which is denoted by $F_{ROI}(\mathbf{k})$, where $\mathbf{k} = [k_x \;\; k_y \;\; k_z]$ denotes the spatial frequency variables. In order to design the RF pulse, the excitation k-space, i.e., $F_{ROI}(\mathbf{k})$ should be sampled. Because the design process of a multi-dimensional excitation pulse is given in detail in Section 3.4.3, such an explanation is omitted from this section; it is assumed that the ROI is excited as desired.

The second stage in an MRI experiment is phase encoding. Assume the excited region is as given in Fig. 5.1. The curved axis passing through the ROI is denoted by ν (which will be referred to as the main axis of the ROI), and its spatial frequency by k_ν. For the RF encoding scheme to be effective, the required number of different RF field distributions is more than the number of encoding directions. Hence, at least two different magnetic field distributions are needed for a single phase encoding direction. Let us denote two RF fields by B_1^a and B_1^b and assume that these fields are fairly uniform in amplitude across the sample volume, but have different phase distributions, which are denoted by k_ϕ^a and k_ϕ^b (The phase distributions are defined along the ν-axis and with respect to the x-axis). When an RF pulse is applied from a transmit RF coil, the phase distribution of the coil is imposed on the spins, in case the flip angle is smaller than 180°. For simplicity, the flip-angle of the multi-dimensional excitation pulse will be assumed to be 90°, without loss of generality. In this case, the initial magnetization when the excitation pulse is transmitted from coil a becomes:

$$\begin{aligned} M_1(a) &= M_0 e^{j\pi/2} e^{jk_\phi^a} \\ &= jM_0 e^{jk_\phi^a} \end{aligned}$$

When the flip angle of the second pulse is large enough such that the longitudinal axis lies between the initial and final positions of the magnetization, i.e., the flip

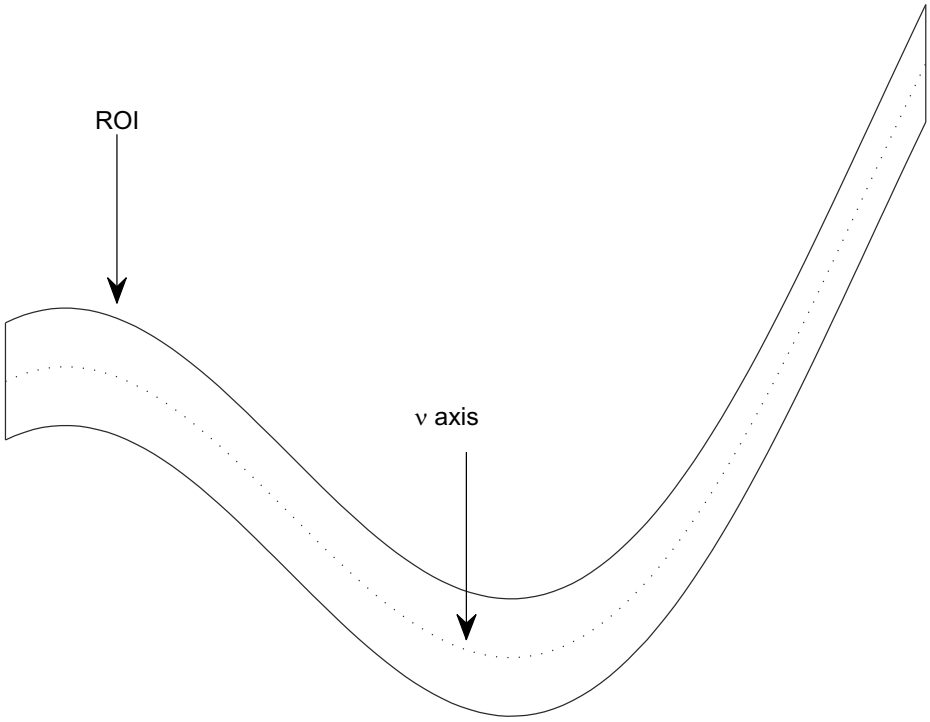

Figure 5.1: Illustration of an arbitrarily defined region-of-interest and the axis ν that passes through it on which the phase gradients of the fields are defined.

angle is larger than 90° or smaller than −90° in this example, then the phase of the initial magnetization is conjugated, with respect to the phase-distribution of the transmission coil. In this study, the flip angle of the second and following pulses will be assumed as 180°. When these refocusing pulses are applied from the two coils in an alternating order, starting with coil b, the magnetization becomes:

$$\begin{aligned}
M_2(a) &= M_1^* e^{j2k_\phi^b} \\
&= -jM_0 e^{-jk_\phi^a + j2k_\phi^b} \\
M_3(a) &= M_2^* e^{j2k_\phi^a} \\
&= jM_0 e^{j3k_\phi^a - j2k_\phi^b} \\
M_4(a) &= -jM_0 e^{-j3k_\phi^a + j4k_\phi^b} \\
&\vdots \\
M_{2n}(a) &= -jM_0 e^{-j(2n-1)k_\phi^a + j(2n)k_\phi^b} \qquad (5.1) \\
M_{2n+1}(a) &= jM_0 e^{j(2n+1)k_\phi^a - j(2n)k_\phi^b} \qquad (5.2)
\end{aligned}$$

where the total time is assumed to be very small compared to the relaxation

time constants. Similarly, by alternating the order of the fields and starting the excitation process with field b, the transverse magnetization becomes

$$\begin{aligned}
M_1(b) &= jM_0e^{jk_\phi^b} \\
M_2(b) &= -jM_0e^{j2k_\phi^a - jk_\phi^b} \\
M_3(b) &= jM_0e^{-j2k_\phi^a + j3k_\phi^b} \\
M_4(b) &= -jM_0e^{j4k_\phi^a - j3k_\phi^b} \\
&\vdots \\
M_{2n}(b) &= -jM_0e^{j(2n)k_\phi^a - j(2n-1)k_\phi^b} \qquad (5.3) \\
M_{2n+1}(b) &= jM_0e^{-j(2n)k_\phi^a + j(2n+1)k_\phi^b} \qquad (5.4)
\end{aligned}$$

In such a pulse sequence, the distance between two closest samples in the k-space is $\pm(k_\phi^a - k_\phi^b)$, depending on which one is positive. It should be noted that, the obtained data can be multiplied with j or $-j$ depending on the signs of the transverse magnetizations given in Eqs. (5.1)-(5.4) at the post-processing stage, such that all magnetizations will be in the form $M_0e^{(\cdot)}$. Therefore, the complex identities will be dropped for the rest of this section. When fields a and b are used for reception, the signal will be multiplied with $e^{-jk_\phi^a}$ and $e^{-jk_\phi^b}$, respectively. This is because the transverse sensitivities are conjugated when the same coil is used for reception instead of transmission and vice versa (Section 2.2).

In order to demonstrate how the k-space is traced along the phase encoding direction the phase gradient of field b is assumed to be $k_\phi^b = -k_\phi^a/2$. Note that, an asymmetric phase distribution is assumed since the symmetric distributions are a subset of the asymmetric ones. In Fig. 5.2, the phase distributions of the two coils are indicated on the left hand-side of the vertical axis, i.e., the square-marker indicates the location of k_ϕ^a and the triangle-marker indicates the position of k_ϕ^b. Note that, the distributions are slightly shifted to the left in order to increase clarity. When the sequence given in Fig. 5.3 is applied, the phase distribution of the first echo, i.e., M_1, is the same phase distribution as that of coil a, which is shown by the first cross-marker on the left in Fig. 5.2(a) where the vertical axis is the k-space and the horizontal axis is the time. However, when coil a is used for reception, the magnetization is multiplied with the sensitivity of the receive coil, which is the conjugate of the transmit sensitivity. Therefore, the

phase of the received signal is zero, as indicated with the first dot-marker on the left in Fig. 5.2(a). When the sequence is applied with the fields in the order "$a-b-a-b-a-$..." and the samples are taken at the echo times shown in Fig. 5.3, the remaining visited k-space locations, which are listed in Eqs. (5.1)-(5.2), are as shown with in Fig. 5.2(a) with respect to time. The cross-markers show the actual visited k-space locations, and the phases of the acquired signals when coil a is used for reception are shown as dot-markers. In Fig. 5.2(b), the k-space locations that are visited when the sequence is applied starting with field b, but coil a is used for reception are shown. Figs. 5.2(c) and (d) show the k-space locations visited by the sequences given in Figs. 5.2(a) and (b) in a vertically aligned fashion, respectively, and Fig.5.2(e) shows all of the visited k-space locations together. It can be seen that, the excitation k-space is traced uniformly using the fields, a and b.

Starting the sequence with field b instead of field a shifts the acquired k-space points by $k_\phi^b - k_\phi^a$. The same shift can be obtained by receiving with field b instead of field a. Hence, if both fields are used for reception, while the sequence is started with field a, the acquired points will be as given in Figs. 5.4(a) and (b). If the sequence starts with field b, then all points will be shifted by $k_\phi^b - k_\phi^a$ which will change only the location of the last sample. Therefore, the number of points obtained in the excitation k-space increases when multiple receive fields are used, which is the same phenomenon that enables receive array methods such as SENSE [86] and SMASH [87].

In Appendix B, various encoding schemes that employ more than two fields for reception and/or transmission are given. The same visualization approach is used in those figures, and therefore, those figures should be analyzed in a similar manner. The effect of using multiple reception or transmission fields are summarized in Appendix B as well. It should be noted that, the approaches can be extended to more receive and transmit fields in a similar manner.

The multi-dimensional pulses provide encoding in the first direction and RF encoding applications listed above provide encoding in the second direction. To encode the data in the third direction, conventional gradient methods can be

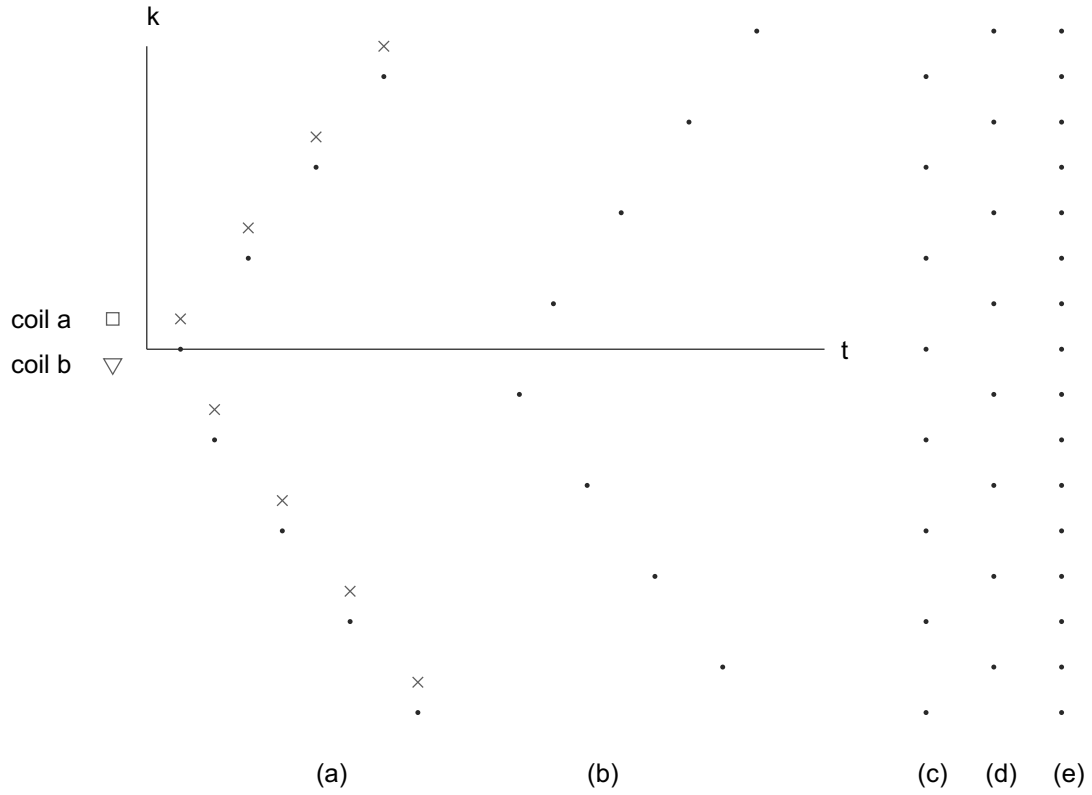

Figure 5.2: Illustration of the acquired k-space points when two transmit and one receive fields are employed. (a),(c) The acquired k-space points when field a is used to start the sequence and for reception. (b),(d) The acquired k-space points when field b is used to start the sequence but field a is used for reception. (e)All acquired k-space points.

employed. Alternatively, by using more than two RF fields, RF encoding can be used for the third direction as well. Although the use of conventional gradient methods is faster, these methods limit the region between two planes orthogonal to the direction of the gradient field. The use of RF encoding in the third direction is slower but the region can have an arbitrary shape in the third direction as well. It should be noted that, the three encoding directions do not have to be linear nor orthogonal. However, the linear independence of the three directions increases the efficiency of the encoding. Still, the sufficient condition is that the three encoding directions should span the ROI.

At the image reconstruction phase, the k-space data may be transformed to images by inverse Fourier transform or by other means. The resulting pixel data

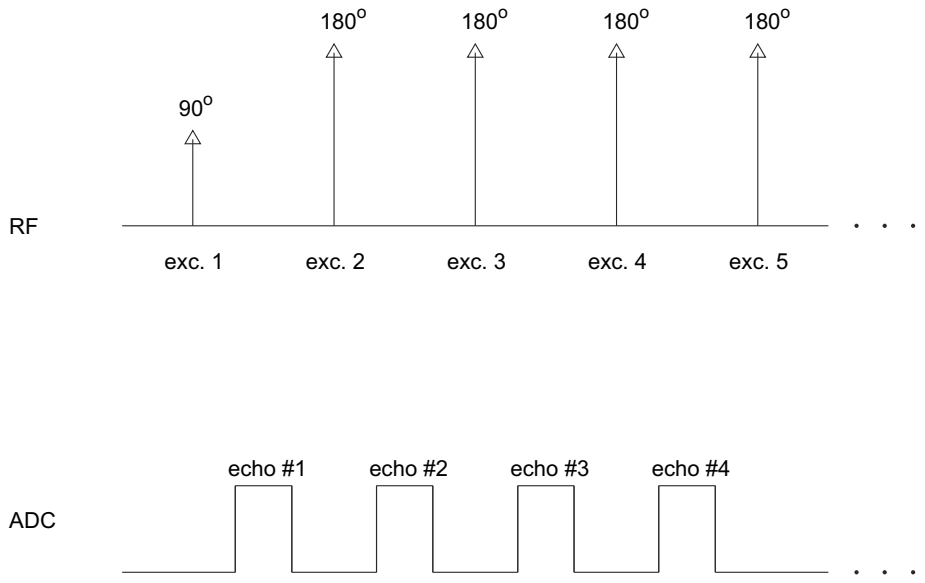

Figure 5.3: Representation of the pulse sequence that is used for RF encoding of the spins.

can be coincided with the data of excited region to give the shape of the ROI to the pixels, similar to unwarping [38]. As the phase gradients of the RF fields are known, the shape information of each pixel can be determined.

5.3 Methods

In order to demonstrate the ideas presented, simulations are performed in Matlab (The Mathworks Inc., Natick, MA, USA). For this purpose, a hypothetical test object is formed (Fig. 5.5). As the reference solution, a Cartesian encoding scheme that employs linear gradient fields is assumed. In this case, the slice selection, the phase encoding and the readout are along the z-, y- and x-directions, respectively. For the proposed method, the phase encoding step is performed using RF encoding along the ϕ-direction whereas the slice selection is performed along the radial direction (Fig. 5.6) using multi-dimensional excitation pulses, and the readout is along the z-direction. For RF encoding, the $m = 1$ (quadrature) and $m = 2$ modes of a birdcage coil are assumed to be used. The magnitude and phase distributions of the coils are given in Fig. 5.7. The fields are assumed

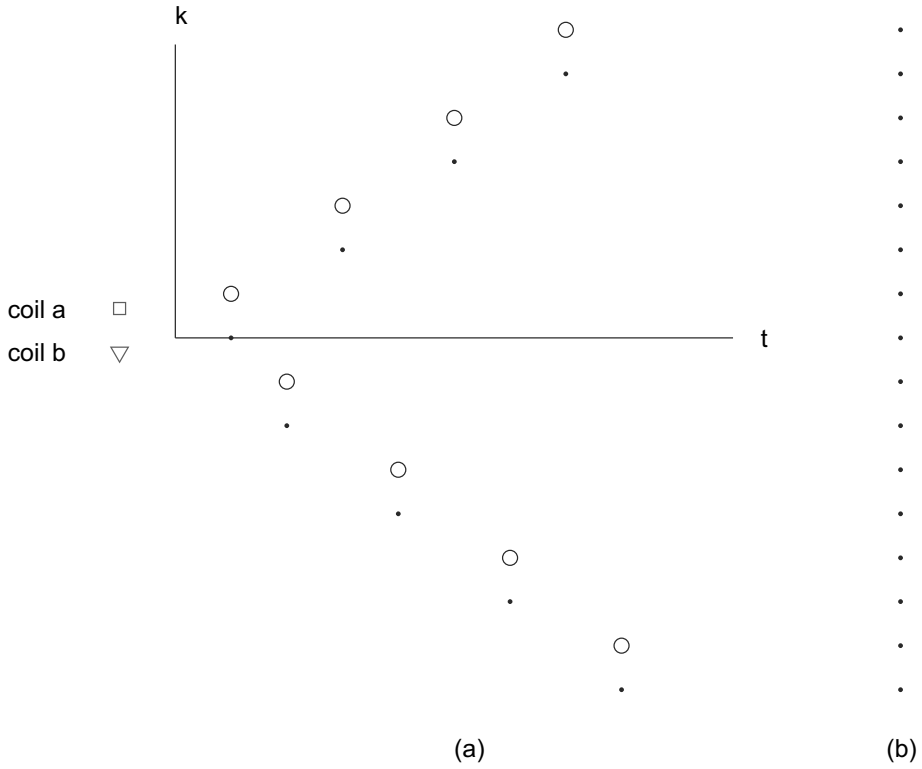

Figure 5.4: Illustration of the acquired samples in the k-space when two transmit and two receive fields are used. (a) The acquired k-space points when field a is used to start the sequence and for reception, circle-markers: actual k-space locations, dot-markers: k-space distribution of the received signal, when coil a is used for reception. (b) The acquired k-space points when field a is used to start the sequence but both fields are used for reception.

to be invariant along the longitudinal direction. Note that, the second-order mode of the birdcage coil has a nonuniform field in the transverse plane. In order to correct for this non-uniformity, adiabatic pulses can be used [88, 89]. Therefore, this non-uniformity is neglected in the simulations. An example RF pulse sequence for the proposed solution is given in Fig. 5.8. Note that, the magnitudes of the RF pulses are normalized to put the emphasis on the pulse sequence. In order to signify the effect of phase encoding on the images, the other two encoding steps are assumed to be perfect for both approaches. For the reference solution, 24 phase encoding steps are assumed to be performed along the y-direction. The Fourier transform of the object is obtained, downsampled, and inverse Fourier transform is applied to observe the effect of undersampling. For the proposed

solution, the object is expressed in terms of the cylindrical coordinates, and then its Fourier transform is obtained (again in cylindrical coordinates) and downsampled to 24 samples in the k_ϕ-direction. By taking the inverse Fourier transform, and mapping back to the Cartesian coordinates, the effect of undersampling is observed. The results will be presented in the next section.

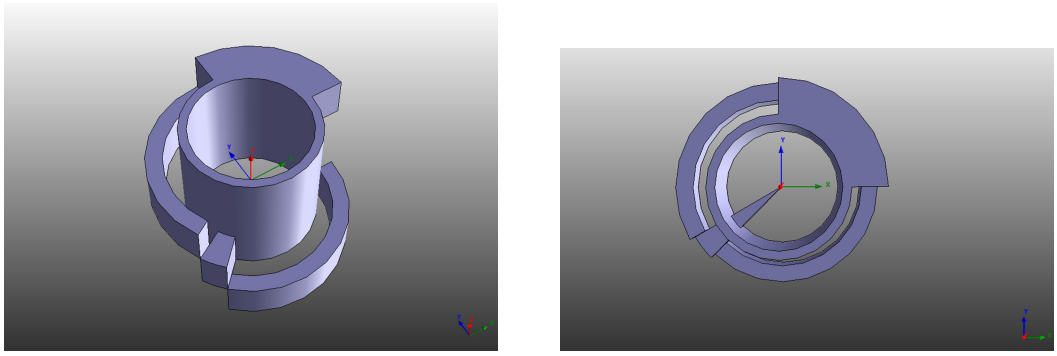

(a) (b)

Figure 5.5: The hypothetical object used for the simulations. **a:** Oblique view. **b:** Top view.

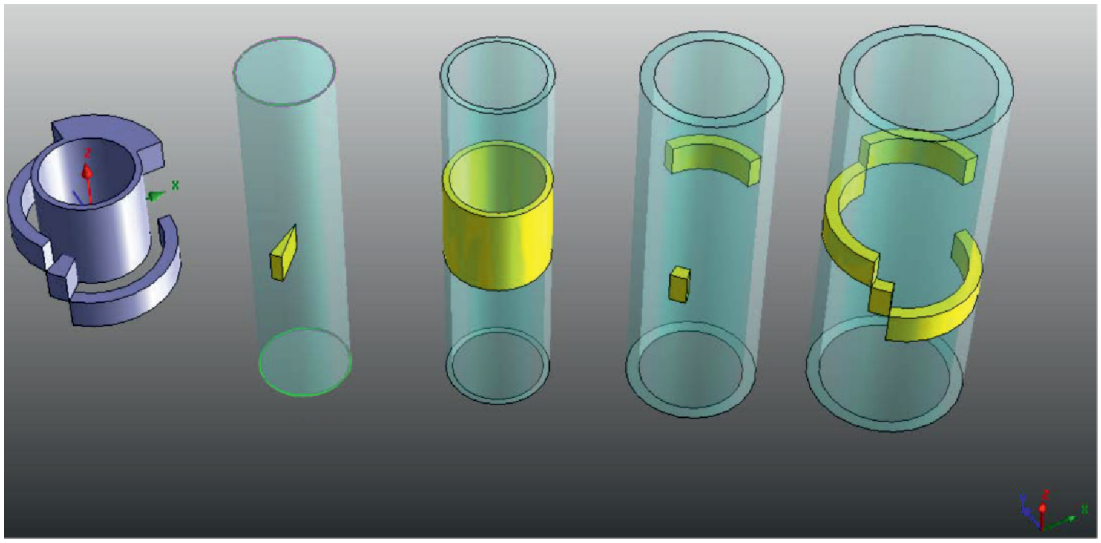

Figure 5.6: The hypothetical object used for simulations (left-most), the radial slices of the proposed solution (highlighted with cyan color), and the portions of the object that fall into the slices (highlighted with yellow color).

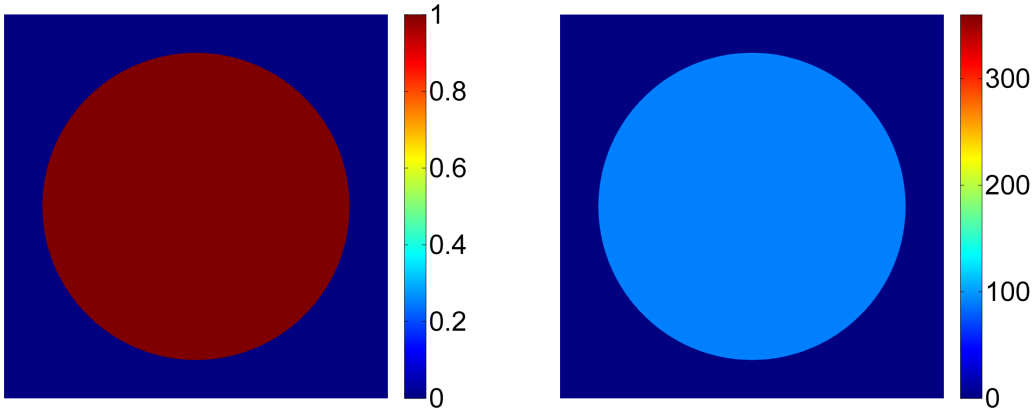

(a) Magnitude (b) Phase

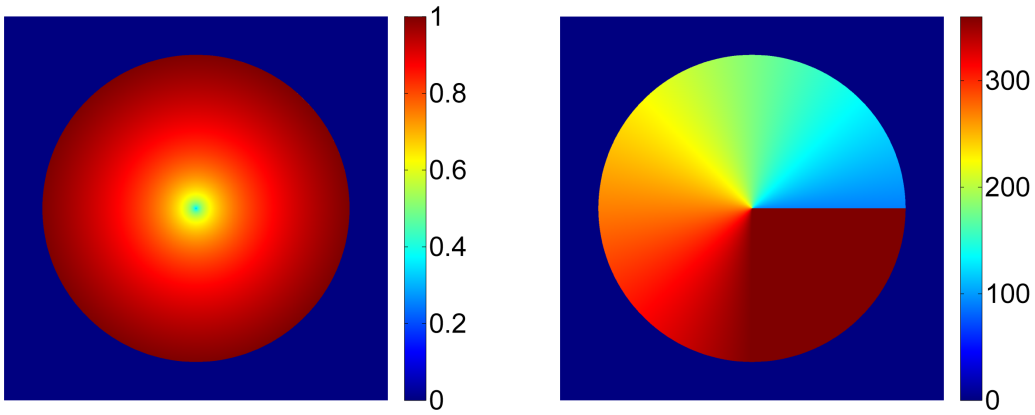

(c) Magnitude (d) Phase

Figure 5.7: Magnitude and phase distributions of the fields used in the simulations. The plots are in the transverse plane. **a-b:** Quadrature birdcage mode ($m = 1$ mode). **c-d:** Second order mode ($m = 2$ mode).

5.4 Results

Fig. 5.9 shows the simulated images obtained using both methods. For both methods, the images are shown on the transverse plane, for different offsets along the longitudinal axis. When the images are compared, it can be seen that the artifacts caused by the finite number of phase encoding steps are significantly different. When the proposed method is used, the artifacts are along the angular

direction whereas for the conventional method, the artifacts are along the vertical axis. Although the extent of the artifacts in terms of the field-of-view, i.e., $\approx 0.8\times$ FOV_y for the conventional method and $\approx 0.8 \times 2\pi$ for the proposed solution, the artifacts cover a larger portion of the images in Fig. 5.9(b), (h) and (k) compared to Fig. 5.9(c), (i) and (l). Furthermore, because the encoding direction of the proposed method suits the shape of the object much better, it can be seen that the edges are represented better [Fig. 5.9(c), (i) and (l)]. For the reference case, the edges are blurred due to the incompatibility between the encoding direction and the object [Fig. 5.9(b), (h) and (k)].

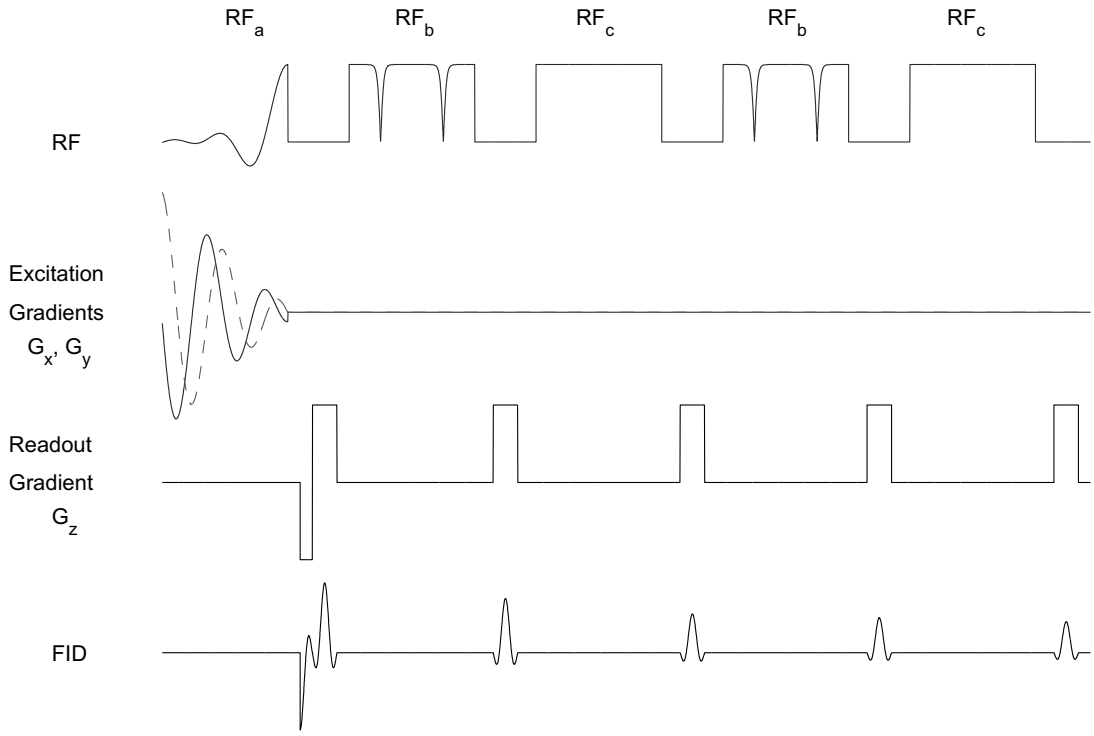

Figure 5.8: Example RF pulse sequence for the proposed imaging algorithm. In cases where the RF field magnitude distribution of a coil is non-uniform, adiabatic pulses can be employed (RF_b), as demonstrated. The RF amplitudes are normalized separately for demonstration purposes. In this example sequence, the gradient fields that correspond to a spiral excitation excitation k-space trajectory are demonstrated. The acquisition windows are indicated with example FIDs. When coil a is used instead of coil c, the sequence summarized in Eqs. (5.1)-(5.2) can be obtained.

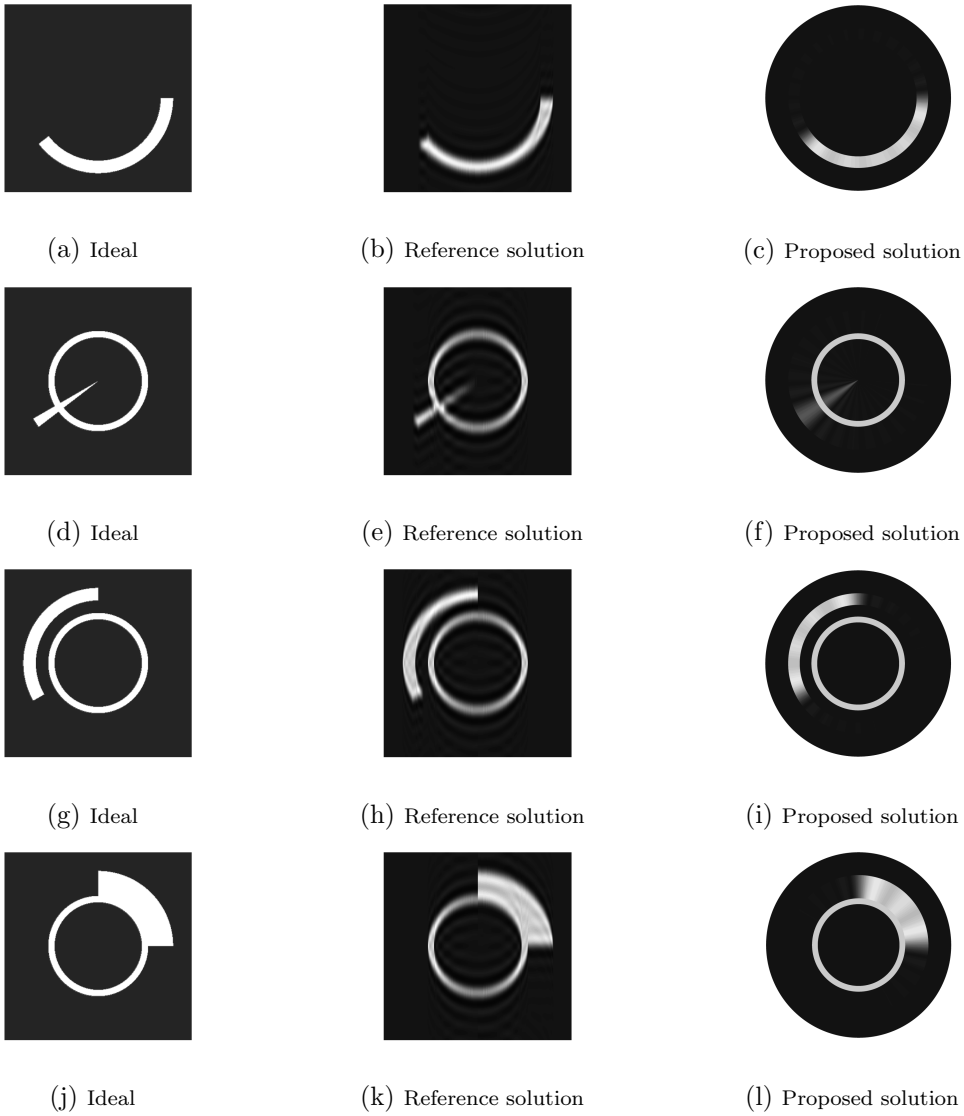

(a) Ideal (b) Reference solution (c) Proposed solution

(d) Ideal (e) Reference solution (f) Proposed solution

(g) Ideal (h) Reference solution (i) Proposed solution

(j) Ideal (k) Reference solution (l) Proposed solution

Figure 5.9: Simulation results comparing the proposed method with the Cartesian encoding scheme and the ideal images. **a-c, d-f, g-i, j-l:** Images of the first, second, third and fourth slice along z-direction, respectively. Note that, for the proposed solution, the images are mapped from the ϕz-plane to the xy-plane. The encoding steps in the slice selection and readout encoding directions are assumed to be perfect for both methods. The effect of finite number of phase encoding steps (along y-axis for the reference solution and along ϕ-axis for the proposed solution) on the images are demonstrated.

5.5 Discussion

In this study, a novel combination of RF encoding and multi-dimensional excitation techniques is proposed. The embodiment proposed in this dissertation uses multi-dimensional pulses in order to excite curved ROIs. Then, RF encoding is used to image the ROI using non-rectangular and nonuniform voxels. Although the SAR of the proposed method is higher than conventional gradient imaging methods because of refocusing pulses, the method localizes the FOV to non-rectangular regions to reduce the total scan time, which may lead to less energy to be absorbed by the sample. The method is demonstrated using computer simulations.

When the simulation results are observed, there are many differences compared to the conventional method that should be noted. First, it can be seen that, the artifacts due to the finite number of phase encoding steps are along the angular direction rather than the y-direction. Second, the extent of the artifacts are much less, since the artifacts cover the whole image for the reference case. Third, because the encoding direction suits the object better, edge voxels are represented better. It should be noted that, the voxel sizes are nonuniform along the radial direction, and the voxel shapes are non-rectangular in the demonstrated example, as suggested by the method. Furthermore, because the FOV does not need to be a rectangular region that encloses the ROI, convex ROIs or ROIs that enclose regions that are not of interest can be imaged much rapidly with the proposed method.

At the operation frequencies of gradient fields, the wavelength is much larger than the size of the MRI scanners. Although nonlinear gradient fields can be realized as mentioned in Chapters 3 and 4, the variation in space that can be achieved with gradient fields is limited. However, the higher frequency of the RF fields allows fields with rapidly varying phase gradients to be generated. The resulting pixel sizes and shapes depend on the phase gradients in the ROI in addition to the shape of the ROI, and can be tailored by designing the ROI and the phase distributions of the fields accordingly. The pixel sizes can be non-uniform if the phase gradients vary nonlinearly in the ROI. Therefore, RF

encoding may provide more efficient voxel shaping in some cases.

RF encoding requires at least one more field than the number of RF encoding directions. In this study, the method is demonstrated for two fields and a single encoding direction. However, the ideas can be extended to more directions. Furthermore, having more fields than required may yield advantages such as increased resolution or FOV, as summarized in Appendix B. Instead of producing separate coils for the transmit fields, transmit arrays can be employed to produce fields with the necessary amplitude and phase distributions among the elements of the array.

During the reception, the field distribution of the RF coil that is used for reception is imposed onto the magnetization data. Therefore, using multiple fields with different field distributions may increase the resolution or the FOV as demonstrated in Appendix B. Instead of using multiple receive coils assigned to distinct receive channels, a receive array can be employed.

In the case that uniform amplitude cannot be obtained for a certain field distribution, adiabatic pulses [88, 89] can be employed to compensate for the effect of the non-uniform amplitude. Furthermore, crusher gradients can be employed to compensate for non-uniformity of field amplitudes inside the sample volume. Alternatively, the refocusing pulses can be applied as multi-dimensional pulses so that only the spins inside the ROI are affected, or receive fields that are not sensitive to the regions in which the transmit field amplitudes are not uniform can be used. It should be noted that these approaches can be combined to increase the efficiency of the compensation against field non-uniformity. An alternative approach is using the non-uniformity of the field amplitudes for encoding the data along the non-uniformity direction as given in detail in [44]

RF encoding requires the application of multiple refocusing pulse. Therefore the SAR may increase significantly. Hence, the applicability of the method at higher field strengths may be limited. However, one of the goals of the proposed method is reducing the total scan time through (*i.*) the reduction of the field-of-view to non-rectangular regions, and (*ii.*) the reduction of total number of encoding steps by actively determining the resolution in space (achieving higher

resolution in certain regions while lowering the resolution in other regions). Because the method uses multi-dimensional excitation pulses, the excitation can be focused in all three directions to fit to the region-of-interest more tightly than shown in the example study. Although such a pulse would have a higher SAR, the total scan time would be reduced further. Therefore, the method may result in a lower energy level that is absorbed by the sample.

5.6 Conclusion

In this study, RF encoding and multi-dimensional excitation pulses are combined for the imaging of curved regions. By using multi-dimensional excitation pulses, arbitrarily shaped regions can be excited. Hence, the excitation region can be tailored to conform to the region-of-interest. Then, by designing the RF encoding fields accordingly, the region-of-interest can be imaged using nonuniform and non-rectangular voxels. With the proposed method, the need to acquire data from outside the region-of-interest is relaxed, since a non-rectangular FOV can be imaged using non-rectangular voxels. Therefore, the total scan time can be reduced.

Chapter 6

Discussion

In this dissertation, several novel techniques are studied, with the goals of (*i.*) reducing the total energy absorbed by the subject, through the reduction of the SAR or the total scan time and (*ii.*) finding the upper limit on the image quality and the lower limit on the power absorbed by the subject.

In the second chapter of this dissertation, analytic expressions for the ultimate intrinsic signal-to-noise ratio (UISNR) and the ultimate intrinsic specific absorption rate (UISAR) are derived. These expressions are valid as long as the distance between the surface and the point of interest is smaller than the wavelength; this condition is referred to as the quasi-static limit. In the derivations, the size and the shape factors of a sample and a coil combination are defined. The shape factor depends on the geometrical shape of the sample, the location and the shape of the region-of-interest inside the sample, and the structure of the coil; it is defined for a unit-sized object that has the same shape as the sample, and therefore, it is independent from the size of the sample. When the maximum value of the shape factor is obtained, the UISNR and UISAR of the sample of interest can be calculated. The size factor on the other hand, shows the dependence of UISNR and UISAR on the physical dimensions of the sample explicitly. Although the dependence on the size factor was previously shown for specific geometries, size and shape factors are defined for an arbitrarily shaped sample for the first time, to the best of the author's knowledge. By factoring out

the shape and the size factors, the dependencies of UISNR and UISAR on the static magnetic field strength and the sample properties including the size, the permittivity, the permeability, the conductivity and the temperature are shown explicitly. In order to obtain numerical values, the shape factor of the coil-subject combination must be determined using simulations, calculations or experiments. The strongest aspect of the expressions given in this dissertation comes into picture when there is a known value for SNR, SAR, ISNR or ISAR, or the ultimate values of these parameters. In this case, these parameters can easily be calculated for a similar sample shape when any affecting parameter is altered. Using the relations between the SNR and the ISNR and those between the SAR and the ISAR that are given, the dependence of the SNR and the ultimate-SNR and that of the SAR and the ultimate-SAR on the shape and size factors and any of the other affecting parameters can be obtained easily. The main limitation of the expressions given in this dissertation is that the samples are assumed to be homogeneous during the derivations, which is generally not the case in real-life scenarios.

In the third chapter, a novel SAR reduction method that employs nonlinear gradient fields (NLGFs) is introduced. The use of NLGFs alters the well-known Fourier transform relationship that exists between the excitation profile and the excitation k-space at the small-tip-angle regime. Therefore, the RF pulse that excites the desired profile is altered when an NLGF is used, leading to a different SAR value. The method is demonstrated using simulations and phantom experiments. In the three case studies given in this dissertation, SAR reductions between 15% - 54% are obtained. The applicability of the proposed excitation method depends on the compatibility of the nonlinear gradient field and the desired excitation profile. Therefore, higher reductions in SAR can be obtained for other application-field combinations. Although replacing a linear gradient field with an NLGF may result in a higher SAR as well, the proposed method can only reduce the SAR, as long as the three conventional LGFs are available together with the NLGFs. As demonstrated, the method is compatible with multidimensional excitation pulses and the variable rate selective excitation algorithm. Although not shown in this dissertation, excitation using NLGFs is compatible

with other excitation approaches such as B_1^+−shimming, and application specific coil design, and can be used for SAR reduction at the large-tip-angle regime in a similar manner as well.

In the fourth chapter, NLGFs are used for reducing the field-of-view. NLGFs were previously used for reduced-FOV imaging by exciting only inner volumes during excitation [34–36] or by dephasing outer volumes [37]. However, the effect of using an NLGF on the aliasing artifacts was not investigated. When NLGFs are used for excitation, and the field-of-view is reduced, the aliasing artifacts may fold into the outer sections of the FOV, depending on the FOV-reduction directions. With a proper selection of the FOV-reduction directions and band-pass filtering at the post-processing stage, these artifacts may be filtered out, leaving an uncorrupted image of the region-of-interest. Although the method may require an increase in the FOV along the readout direction, the FOV reduction in the other two directions may result in a reduction in the overall scan time. The method is demonstrated using an in-vivo experiment, and 60% reduction is obtained compared to the conventional imaging approach. Because there are no refocusing, saturation nor multi-dimensional pulses, and no dephasing gradients, the proposed method can be used for reduced-FOV imaging purposes without increasing the echo-time or the SAR, thereby decreasing the total scan time and the total energy absorbed by the subject.

In the fifth chapter of this dissertation, the RF encoding method is studied, for the purpose of imaging curved regions. It is shown that the encoding of the spatial information can be accomplished by using various RF fields with different field distributions in space. Because the wavelength is much smaller at the operation frequencies of the RF fields, compared to gradient fields, much rapid field variations can be obtained. With the proposed embodiments, imaging of curved regions with nonuniform and non-rectangular voxels can be performed. The method is proposed to be used together with multi-dimensional excitation pulses, in order to localize the excitation region to the region-of-interest. Although such excitation pulses and the multiple refocusing pulses required for RF encoding increase the SAR increases significantly, the FOV can be tailored to fit to the region-of-interest tightly. In this case, the FOV and hence, the required

number of repetitions would decrease, which would reduce the total scan time and possibly reduce the total energy absorbed by the subject.

The topics studied in this dissertation share the same goal, which is decreasing the total energy absorbed by the sample, through the reduction of the SAR, or the total scan time. However, these ideas act on different parts of imaging: the third chapter is based on altering the RF pulse shape; the fourth chapter is based on changing the excitation profile; the fifth chapter acts on the encoding part of an experiment. Therefore, these ideas can be combined as well. The techniques regarding nonlinear gradient fields towards reducing the SAR reduction and the FOV can be combined to find an excitation profile that not only can be excited with lower SAR, but also yields aliasing artifacts that do not corrupt the region-of-interest, thereby enables reduced FOV imaging. Furthermore, these techniques can be combined with the RF encoding technique as well. By using nonlinear gradient fields, multi-dimensional excitation pulses that excite only the region-of-interest with low SAR can be designed. Furthermore, by permitting some extensions from the excitation region, which would alias to the regions outside the region-of-interest when field-of-view is reduced, the SAR can be further reduced. In addition, the same approaches can be implemented with the refocusing pulses as well, in order to lift the necessity of applying adiabatic pulses when the RF field amplitude is nonuniform. By using RF encoding at the encoding stage, the subject can be imaged using non-rectangular voxels, thereby reducing the total scan time. Lastly, the derivations related to the UISNR and the UISAR may be used for evaluating the performance of such imaging approaches in terms of the SNR and the SAR.

Although utilizing linear gradient fields has many advantages in MRI, it also limits imaging capabilities. There are two main advantages to using linear gradient fields: first, the equations governing the excitation and encoding processes are easy to formulate Fourier transforms in Cartesian coordinates; and second, the voxels are perfectly rectangular and uniform. However, these are also limitations in MRI. For example, when the region-of-interest is a curved, small tissue inside the body, either the whole slice needs to be encoded with a uniform resolution, or the SAR intensive sequences are required to reduce the field-of-view.

Nonlinear gradient fields, and RF encoding, in contrast, increase the complexity in the analysis of excitation and encoding processes. The voxels are not uniform nor regularly shaped, and the excitation k-space is no longer the exact Fourier transform of the excitation profile. However, this complexity also broadens the range of possibilities. Nonuniform resolution enables high-resolution imaging of the ROI while the FOV remains unaltered, and the excitation can be focused into curved regions using nonlinear gradient fields. Furthermore, the excitation k-space is altered when nonlinear gradient fields are used, which may only reduce the SAR when compared with using only linear gradient fields.

Imaging with MRI is a complex problem with many design goals, such as reducing the SAR and the scan time, and increasing the resolution, the signal-to-noise ratio and the field homogeneity. When various approaches to solving this problem are combined, such as B_1^+-shimming, multi-dimensional excitation pulses, variable-rate selective excitation, excitation and encoding using nonlinear gradient fields, application specific coil design and RF encoding, significantly different imaging schemes can be designed that not only better suit the desired region-of-interest or the goal of examination, but also increase efficiency in terms of the imaging time, the SAR and the resolution.

Chapter 7

Conclusion

In MRI, three of the most important parameters are the specific absorption rate (SAR), the signal-to-noise ratio (SNR) and the total scan time. Therefore, in this dissertation, various novel techniques are studied with the following goals: finding the limits on the SNR and the SAR; reducing the SAR; and decreasing the total scan time. In the first study of this thesis, the ultimate intrinsic signal-to-noise ratio, and the ultimate intrinsic specific absorption rate, which are the upper limit on the SNR and the lower limit on the SAR, are studied. The dependence of these parameters on the geometrical and electromagnetic properties of the sample are shown explicitly. The intrinsic SAR as well as the shape and the size factors of a sample-coil combination are defined. In order to compare different RF pulse envelopes, the normalized-SAR, which depends only on the shape of the RF envelope, is defined. Another contribution of this dissertation is that a novel SAR reduction method, which employs gradient fields with nonlinear variation in space, is proposed, and the effect of such gradient fields on the pulse design process is formulated. The method is compatible with other excitation techniques such as multi-dimensional excitation pulses, the variable rate selective excitation algorithm, B_1^+-shimming and application specific coil design. In another topic of this study, nonlinear gradient fields are used for excitation with the purpose of reducing the field-of-view and therefore, the total scan time: The method keeps the SAR and the echo-time unaltered, which is its main advantage

compared to other FOV reduction techniques. Finally, RF encoding method has been studied with the purpose of imaging curved regions with nonuniform and non-rectangular voxels. Although RF encoding increases the SAR significantly, significant reductions in FOV and total scan time can be obtained. Because the techniques studied in this dissertation act on different parts of imaging, these techniques can be combined to reduce the total scan time and the SAR simultaneously.

APPENDIX A

Power Calculations in Cylindrical Samples

In this section, the rotating magnetic field-per-square-root-power for a cylindrical sample will be found using cylindrical basis functions. The reasons for the choice of basis functions are two-fold. First, the accuracy increases because the functions are more suitable to the geometry of interest (as mentioned in the Introduction). Second, it is shown that starting with a full-wave solution and then making a quasi-static assumption leads to the same dependence on sample properties as starting with the quasi-static assumption and using the corresponding basis functions.

A.1 Electric Field Expressions inside the Sample

Consider a circularly cylindrically shaped, isotropic and homogeneous sample with the complex propagation constant $k = \sqrt{-j\omega_0\mu(\sigma + j\omega_0\epsilon)}$. The z-components of the electric and magnetic fields inside this sample can be found by solving the source-free Helmholtz Equation, yielding the following equations

[59]:

$$E_z(\rho,\phi,z) = \sum_{m=-\infty}^{\infty}\sum_{n=-\infty}^{\infty} A_{mn}J_m(k_\rho\rho)e^{jm\phi}e^{-j\frac{2\pi n}{L}z} \quad (A.1)$$

$$H_z(\rho,\phi,z) = \sum_{m=-\infty}^{\infty}\sum_{n=-\infty}^{\infty} -jB_{mn}J_m(k_\rho\rho)e^{jm\phi}e^{-j\frac{2\pi n}{L}z} \quad (A.2)$$

where m and n are the rotational and longitudinal mode numbers, respectively, L is the sample length, $k_\rho = \sqrt{k^2-(2\pi n/L)^2}$ is the radial propagation constant, and the $J_m(k_\rho\rho)$ terms are cylindrical Bessel functions of the first kind and order m with A_{mn} and B_{mn} being the corresponding field coefficients. $Y_m(k_\rho\rho)$ terms (Bessel functions of the second kind and order m), which are also solutions to the Helmholtz equation, cannot be included because the region-of-interest in this study includes $\rho = 0$ and $Y_m(0) \to \infty$. Using Eqs. (A.1)-(A.2) and applying Maxwell's equations as given in reference [60], the transverse field components can be obtained and the whole electric field expression can be put into a matrix form:

$$\mathbf{E}(\rho,\phi,z) = \sum_{m=-\infty}^{\infty}\sum_{n=-\infty}^{\infty}\left[\begin{array}{ccc}\hat{\rho} & \hat{\phi} & \hat{z}\end{array}\right]_{1\times 3}\mathbf{E}_{mn}\mathbf{a}_{mn}e^{jm\phi}e^{-j\frac{2\pi n}{L}z} \quad (A.3)$$

where

$$\mathbf{E}_{mn}(\rho,\phi,z) = \left[\begin{array}{cc} -\frac{j2\pi n}{Lk_\rho}J'_m(k_\rho\rho) & \frac{mk^2}{\sigma'\rho k_\rho^2}J_m(k_\rho\rho) \\ \frac{2\pi nm}{L\rho k_\rho^2}J_m(k_\rho\rho) & \frac{jk^2}{k_\rho\sigma'}J'_m(k_\rho\rho) \\ J_m(k_\rho\rho) & 0 \end{array}\right]_{3\times 2} \quad (A.4)$$

$$\mathbf{a}_{mn} = \left[\begin{array}{c} A_{mn} \\ B_{mn}\end{array}\right]_{2\times 1}$$

and $\sigma' = \sigma + j\omega_0\epsilon$. In (A.3), $\mathbf{E}_{mn}$ contains the cylindrical expansion functions for the electric field in ρ,ϕ,z directions for modes (m,n), and $\mathbf{a}_{mn}$ contains the corresponding coefficients.

Implementing the magnetic field components derived using Maxwell's Equations from Eq. (A.2) into (2.5), the total forward-polarized magnetic field (in

reception) can be found:

$$\begin{aligned} H_{\mathrm{f}}^{\mathrm{r}}(\rho,\phi,z) &= \sum_{n=-\infty}^{\infty}\sum_{m=-\infty}^{\infty}\frac{1}{\sqrt{2}k_\rho}\left(j\sigma' A_{mn}+\frac{2\pi n}{L}B_{mn}\right) \\ &\quad\times J_{m+1}(k_\rho\rho)e^{j(m+1)\phi}e^{-j\frac{2\pi n}{L}z} \qquad (A.5) \\ &= \sum_{n=-\infty}^{\infty}\sum_{m=-\infty}^{\infty}\mathbf{b}_{mn}\mathbf{a}_{mn} \end{aligned}$$

where

$$\mathbf{b}_{mn} = \frac{1}{\sqrt{2}k_\rho}\left[\begin{array}{cc} j\sigma' & \frac{2\pi n}{L}\end{array}\right]_{1\times 2} J_{m+1}(k_\rho\rho)e^{j(m+1)\phi}e^{-j\frac{2\pi n}{L}z} \qquad (A.6)$$

are the rotating magnetic field expansion functions. Similarly, the forward-polarized rotating magnetic field in transmission can be obtained as follows:

$$\begin{aligned} H_{\mathrm{f}}^{\mathrm{t}}(\rho,\phi,z) &= \sum_{n=-\infty}^{\infty}\sum_{m=-\infty}^{\infty}\frac{1}{\sqrt{2}k_\rho}\left(j\sigma' A_{mn}-\frac{2\pi n}{L}B_{mn}\right) \\ &\quad\times J_{m-1}(k_\rho\rho)e^{j(m-1)\phi}e^{-j\frac{2\pi n}{L}z}\,. \qquad (A.7) \end{aligned}$$

A.2 Power Definition

Using Eq. (A.3) in Eq. (2.13), the absorbed power in a uniform cylindrical sample becomes the following:

$$P = \int_{-L/2}^{L/2}\int_{0}^{2\pi}\int_{0}^{R_0}\sigma\mathbf{E}^H(\rho,\phi,z)\cdot\mathbf{E}(\rho,\phi,z)\,\rho\,\mathrm{d}\rho\,\mathrm{d}\phi\,\mathrm{d}z \qquad (A.8)$$

where superscript H denotes the Hermitian (i.e., complex conjugate transpose) operator and "$\cdot$" is the standard dot product [57]. In Eq. (A.8), there are four summations, namely over m, n, m' and n' such that cross-correlation terms can be calculated. However, due to the exponential functions along z- and ϕ-directions in Eq. (A.3), the correlation of two electric field modes (m,n) and (m',n') is zero, unless $m=m'$ and $n=n'$, which leads to $k_\rho=k'_\rho$. Thus, the summations over m and n are sufficient. Furthermore, the exponential terms cancel out due to the Hermitian operation. The integrals can be interchanged with the summations

over the modes and after making some algebraic manipulations the absorbed power is expressed as the following:

$$\begin{aligned} P &= \sum_{n=-\infty}^{\infty}\sum_{m=-\infty}^{\infty}\int_{-L/2}^{L/2}\int_{0}^{2\pi}\int_{0}^{R_0}\left(\mathbf{a}_{mn}^{H}\mathbf{E}_{mn}^{H}\mathbf{E}_{mn}\mathbf{a}_{mn}\right)\sigma\rho\,\mathrm{d}\rho\,\mathrm{d}\phi\,\mathrm{d}z \\ &= \sum_{n=-\infty}^{\infty}\sum_{m=-\infty}^{\infty}\mathbf{a}_{mn}^{H}\mathbf{R}_{mn}\mathbf{a}_{mn} \end{aligned} \tag{A.9}$$

where $\mathbf{R}_{mn}$ is a 2×2 matrix and is given by the expression:

$$\begin{aligned} \mathbf{R}_{mn} &= \int_{-L/2}^{L/2}\int_{0}^{2\pi}\int_{0}^{R_0}\mathbf{E}_{mn}^{H}\mathbf{E}_{mn}\sigma\rho\,\mathrm{d}\rho\,\mathrm{d}\phi\,\mathrm{d}z. \\ &= 2\pi\sigma L\int_{0}^{R_0}\mathbf{E}_{mn}^{H}\mathbf{E}_{mn}\rho\,\mathrm{d}\rho. \end{aligned} \tag{A.10}$$

To maximize SNR and/or minimize SAR, $\xi = |H_{\mathrm{f}}^{\mathrm{r}}|/\sqrt{P}$ should be maximized. Thus, either the absorbed power should be minimized, or the signal (i.e., the rotating magnetic field $H_{\mathrm{f}}^{\mathrm{r}}$) should be maximized. In this study, the magnetic field at the POI is fixed, and the minimum possible power is found with the Lagrange Multipliers Method [61] using the same approach that was previously employed in references [3, 5]. The resulting expression for the minimum absorbed power is as follows:

$$P_{min} = \left[\sum_{n=-\infty}^{\infty}\sum_{m=-\infty}^{\infty}\mathbf{b}_{mn}\mathbf{R}_{mn}^{-1}\mathbf{b}_{mn}^{H}\right]^{-1}|H_{\mathrm{f}}^{\mathrm{r}}|^{2}. \tag{A.11}$$

Implementing $\mathbf{E}_{mn}(\rho,\phi,z)$ from Eq. (A.4) into (A.10) and using the resulting expression with b_{mn} from (A.6) in (A.11), the minimum absorbed power can be expressed as the following:

$$P_{min} = \left[\sum_{n=-\infty}^{\infty}\sum_{m=-\infty}^{\infty}\frac{|J_{m+1}(k_\rho\rho)|^{2}}{4\pi\sigma L\,|k_\rho|^{2}}\frac{G_{\mathrm{num}}(m,n)}{G_{\mathrm{den}}(m,n)}\right]^{-1}|H_{\mathrm{f}}^{\mathrm{r}}|^{2} \tag{A.12}$$

where

$$
\begin{aligned}
G_{\text{num}}(m,n) &= \frac{1}{2}Q(m-1,n)\left[|k|^4+\left(\frac{2\pi n}{L}\right)^4+2\left(\frac{2\pi n}{L}\right)^2\Re\left\{k^2\right\}\right] \\
&\quad +\frac{1}{2}Q(m+1,n)\left[|k|^4+\left(\frac{2\pi n}{L}\right)^4-2\left(\frac{2\pi n}{L}\right)^2\Re\left\{k^2\right\}\right] \\
&\quad +Q(m,n)\left|\frac{2\pi n k_\rho}{L}\right|^2 \qquad \text{(A.13)} \\
G_{\text{den}}(m,n) &= \frac{1}{2}(\omega_0\mu)^2\Big[Q(m,n)\,Q(m-1,n)+Q(m,n)\,Q(m+1,n) \\
&\quad +2Q(m-1,n)\,Q(m+1,n)\Big] \qquad \text{(A.14)}
\end{aligned}
$$

and

$$
Q(m,n) = \int_0^{R_0}\left|J_m(k_\rho\rho)\right|^2\rho\,\mathrm{d}\rho, \qquad \text{(A.15)}
$$

with $\Re\{k^2\}$ being the real part of k^2. Using the following identity (given in [90]):

$$
\begin{aligned}
\int_0^{R_0} J_m(k_\rho\rho)J_m^*(k_\rho\rho)\rho\,\mathrm{d}\rho &= \frac{\rho}{k_\rho^2-k_\rho^{*2}}\Big[k_\rho J_m(k_\rho^*\rho)J_{m+1}(k_\rho\rho) \\
&\quad -k_\rho^* J_m(k_\rho\rho)J_{m+1}(k_\rho^*\rho)\Big]\Big|_0^{R_0} \qquad \text{(A.16)}
\end{aligned}
$$

$Q(m,n)$ is found in closed-form as the following:

$$
\begin{aligned}
Q(m,n) &= \frac{R_0}{4j\ \Re\{k_\rho\}\,\Im\{k_\rho\}} \\
&\quad \times\left[k_\rho J_m(k_\rho^*R_0)J_{m+1}(k_\rho R_0)-k_\rho^* J_m(k_\rho R_0)J_{m+1}(k_\rho^*R_0)\right]
\end{aligned}
$$

where $\Im\{k_\rho\}$ is the imaginary part of k_ρ. Performing a series expansion for each Bessel function and making some algebraic manipulations, $Q(m,n)$ can be expressed as follows:

$$
\begin{aligned}
Q(m,n) &= R_0^2\frac{1}{2}\sum_{a=0}^{\infty}\sum_{b=0}^{\infty}\left|\frac{k_\rho R_0}{2}\right|^{4b+2a+2|m|} \\
&\quad \times\frac{(a+1)^2}{(b)!\,(b+|m|)!\,(b+a+1)!\,(b+a+1+|m|)!}. \qquad \text{(A.17)}
\end{aligned}
$$

It should be kept in mind that k_ρ is a function of n in (A.17). If the object is smaller than the wavelength ($L \ll \lambda$), the conductivity is not very high (a valid assumption for samples that are imaged using MRI, [1, 62]) and $n \neq 0$, then the longitudinal propagation constant $2\pi n/L$ becomes very large in magnitude compared to the wavenumber k. Hence, the approximation $k_\rho \simeq -j2\pi n/L$ can be made. To guarantee that the electromagnetic field decays as it propagates in the transverse plane away from the axis of the sample, the negative branch of the square root is chosen. On the other hand, when $n = 0$, the field propagates only radially, yielding $k_\rho = k$. In this case (i.e., $n = 0$), due to the assumptions that $R_0 \ll L \ll \lambda$ and $|k_\rho R_0| \ll 1$, retaining only the first terms of the summations (a=b=0) in (A.17) yields converged results. Expressing L/R_0 as ζ, $Q(m,n)$ is obtained as:

$$Q(m,n) = \begin{cases} R_0^2 f(m,n) & \text{if } n \neq 0 \\ R_0^{2+2|m|} \frac{1}{2} \left|\frac{k}{2}\right|^{2|m|} \frac{1}{(|m|)!(1+|m|)!} & \text{if } n = 0 \end{cases} \quad \text{(A.18)}$$

where

$$f(m,n) = \frac{1}{2} \sum_{a=0}^{\infty} \sum_{b=0}^{\infty} \left(\frac{\pi n}{\zeta}\right)^{4b+2a+2|m|} \times \frac{(a+1)^2}{(b)!\,(b+|m|)!\,(b+a+1)!\,(b+a+1+|m|)!}. \quad \text{(A.19)}$$

In most applications, the region-of-interest in MRI imaging includes the axis of the object to be imaged. Furthermore, it was previously shown that for external coils, UISNR is lowest on the axis [5]. To find the lowest upper bound on the ISNR, the POI is selected to be on the axis of the sample. On the axis of the object to be imaged, all rotational modes of $H_{\mathrm{f}}^{\mathrm{r}}$ (given by Eqs. (A.5)-(A.6) in Appendix A.1), except $m = -1$, contribute to the noise (Appendix A.2, Eqs. (A.9)-(A.10)) but not to the signal. Thus, when the optimum field coefficients for the maximum SNR on the axis are calculated, only the $m = -1$ mode has a non-zero coefficient. Using this fact, the infinite summation over m can be avoided by retaining only $m = -1$. As a result, the minimum absorbed power on the axis ($\rho = 0$) can be expressed as follows:

$$P_{\mathrm{min,axis}} = \sigma (\omega_0 \mu)^2 R_0^5 \frac{1}{\sum_{n=-\infty}^{\infty} h(-1,n)} |H_{\mathrm{f}}^{\mathrm{r}}|^2 \quad \text{(A.20)}$$

where

$$h\left(-1,n\right)=\frac{1}{\pi\zeta}\begin{cases}\left(\frac{\pi n}{\zeta}\right)^{2}\frac{\left(f(0,n)+f(-2,n)+2f(-1,n)\right)}{\left(f(-1,n)f(0,n)+f(-1,n)f(-2,n)+2f(0,n)f(-2,n)\right)} & \text{, if } n\neq 0\\ 2^{2} & \text{, if } n=0.\end{cases} \tag{A.21}$$

For a lossy medium (i.e., $\sigma \neq 0$), the electromagnetic field decays as it propagates. For the range of conductivity values that are encountered in MRI [1, 62], the length at which the electromagnetic field decays to negligible levels is found to be $L > 4R_0$. Hence, if this condition is met, the sample's length does not affect the absorbed power and, hence, the SNR. Furthermore, due to the factorial functions in the denominator of Eq. (A.19) and the order of the denominator of Eq. (A.21) being higher than the numerator, the infinite summation over the longitudinal mode number n that appears in the denominator of (A.20) converges rapidly to a constant with a finite number of longitudinal modes. The authors observed that the necessary number of modes is approximately 25 when the POI is on the axis, which can increase to above 200 when the POI approaches the surface. Furthermore, when the POI moves away from the origin, the required number of circumferential modes increases to approximately 250 when the surface is approached. When the POI is very close to the surface, numerical error is introduced into the calculations because the expansion is for cylindrical structures, and the effective medium seen is a semi-infinite plane (which is addressed in Section 2.8). Even if the condition $L > 4R_0$ fails, the error it introduces remains below 5%. Replacing the summation in Eq. (A.20) by the obtained constant value, the minimum absorbed power expression given by (A.20) can be expressed as follows:

$$P_{\text{min,axis}} \;=\; 0.9332\sigma\left(\omega_0\mu\right)^2 R_0^5\left|H_{\text{f}}^{\text{r}}\right|^2. \tag{A.22}$$

Then, the rotating magnetic field magnitude per square-root of total absorbed power at the POI, which was defined in Eq. (2.14), can be expressed as the following:

$$\xi=\frac{1}{\sqrt{0.9332\sigma\left(\omega_0\mu\right)^2 R_0^5}}=\mathcal{S}_{\max}\frac{1}{\omega_0\mu\sqrt{\sigma}}R_0^{-2.5} \tag{A.23}$$

where the shape factor is $\mathcal{S}_{\max} = 1.035$, and the size factor is the radius of the cylinder.

APPENDIX B

RF Encoding Approaches using Multiple Fields

In this chapter, possible encoding schemes that use more than two different RF fields for reception and/or transmission are demonstrated, and the effect of such encoding schemes on the resolution and the FOV are summarized. Note that, these possible applications can be easily extended to more receive and transmit fields in a similar manner.

Figures B.1(a)-(b) show the obtained k-space points, when a third field u_1 with a phase gradient $k_\phi^{u_1} = (k_\phi^a + k_\phi^b)/2$ is used in addition to fields a and b, and the sequence starts with field a. By using the conjugates of the obtained samples [Fig. B.1(c)], the gaps in the k-space can be filled [Fig. B.1(d)]. Instead of using post-processing to calculate the complex conjugates, the sequence can be run twice starting with fields a and b. Figures B.2(a)-(b) show the obtained samples when the sequence is run starting with fields a and b, respectively, and fields a, b and u_1 are used for reception. Figs. B.2(c), (d), and (e) show the obtained samples in the first and the second run, as well as all of the obtained samples, respectively. Alternatively, the same sampling rate given in Fig. B.2 can be achieved if 4 receive fields are employed. If the fields have phase gradients $k_\phi^{u_1} = (k_\phi^a + k_\phi^b)/2$ and $k_\phi^{u_2} = (3k_\phi^b - k_\phi^a)/2$ (or alternatively, $k_\phi^{u_2} = (3k_\phi^a - k_\phi^b)/2$,

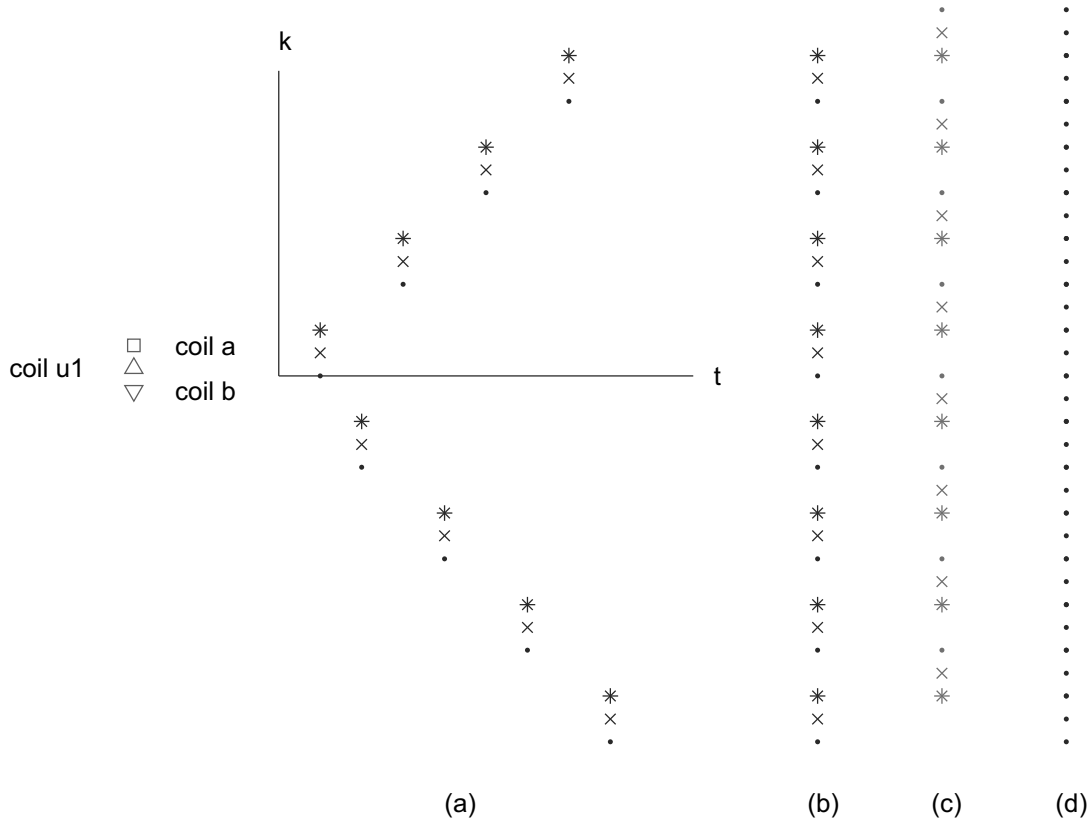

Figure B.1: Acquired k-space points when two fields are used for transmission and three fields are used for reception, in order to increase the FOV. **a:** Coil a is used to start the sequence, asterisk-marker: reception using coil b, cross-marker: reception using coil u_1, dot-marker: reception using coil a. **b:** The k-space points acquired in (a), demonstrated in a vertically aligned fashion. **c:** Conjugates of the k-space points obtained in (a). **d:** All k-space points obtained in (b) and (c).

not shown), then the phase distributions of the four fields (and hence the samples in the k-space) are distributed with equal distances in between. Figs. B.3(b)-(e) show the samples obtained with the individual fields a, b, u_1 and u_2, respectively. It should be noted that, in both cases (Figures B.1-B.3), the sampling rate is doubled with respect to the sequence in Fig. 5.2, and hence, the FOV is doubled.

Fig. B.4 shows the k-space when the third and fourth fields (denoted by c_1 and c_2) have gradients that lie far away from the fields a and b on the k-space axis and are used at the same time in order to obtain far away points simultaneously.

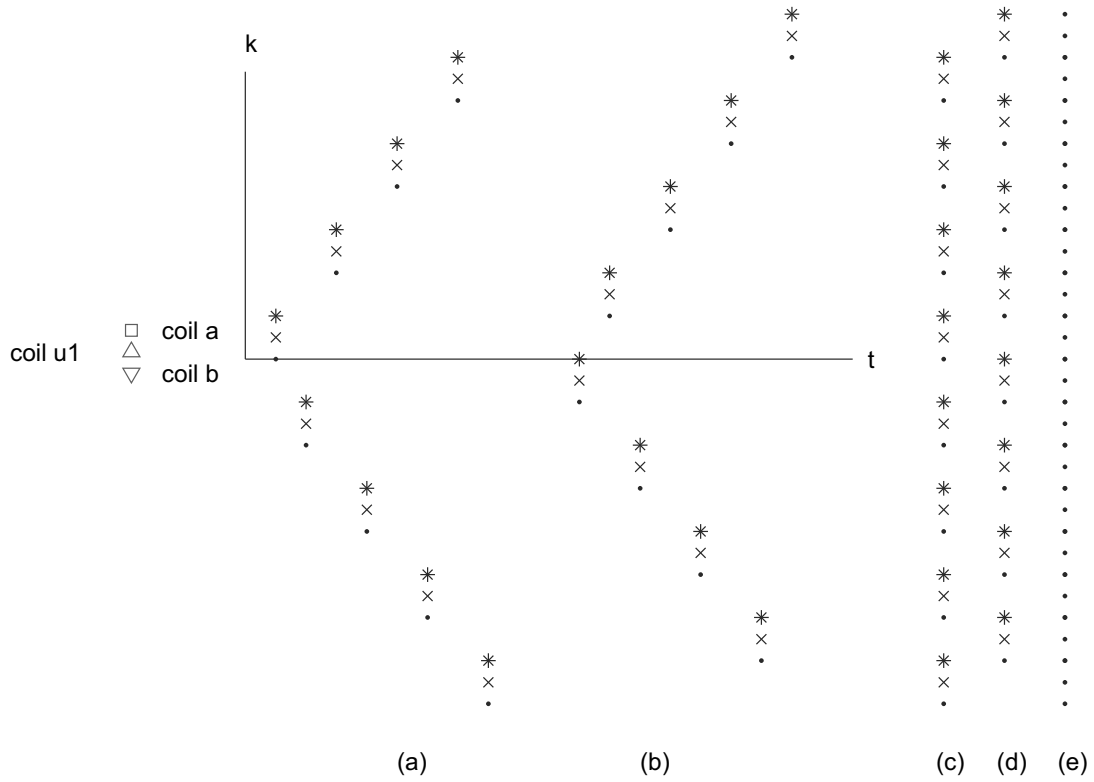

Figure B.2: Acquired k-space points when two fields are used for transmission and three fields are used for reception, in order to increase the FOV. The sequence is run twice to fill the gaps in the k-space. **a:** Coil a is used to start the sequence, asterisk-marker: reception using coil b, cross-marker: reception using coil u_1, dot-marker: reception using coil a. **b:** Coil b is used to start the sequence, asterisk-marker: reception using coil b, cross-marker: reception using coil u_1, dot-marker: reception using coil a. **c:** The k-space points acquired in (a), demonstrated in a vertically aligned fashion. **d:** The k-space points acquired in (b), demonstrated in a vertically aligned fashion. **e:** All k-space points obtained in (c) and (d).

If the fields have $k_\phi^{c_1} = k_\phi^a - 2n(k_\phi^a - k_\phi^b)$ and $k_\phi^{c_2} = k_\phi^b - 2n(k_\phi^a - k_\phi^b)$, the points shown in Figs. B.4(b)-(e) can be obtained simultaneously by using the fields a, b, c_1 and c_2 for reception, respectively. Note that, the figure shows the case where "$n-1$" refocusing (180°) pulses are applied in the first run. If $k_\phi^{c_1} = k_\phi^a + 2n(k_\phi^a - k_\phi^b)$ and $k_\phi^{c_2} = k_\phi^b + 2n(k_\phi^a - k_\phi^b)$, then the samples obtained using fields c_1 and c_2 will be in the lower portion of the k-space rather than in the higher portion (similar

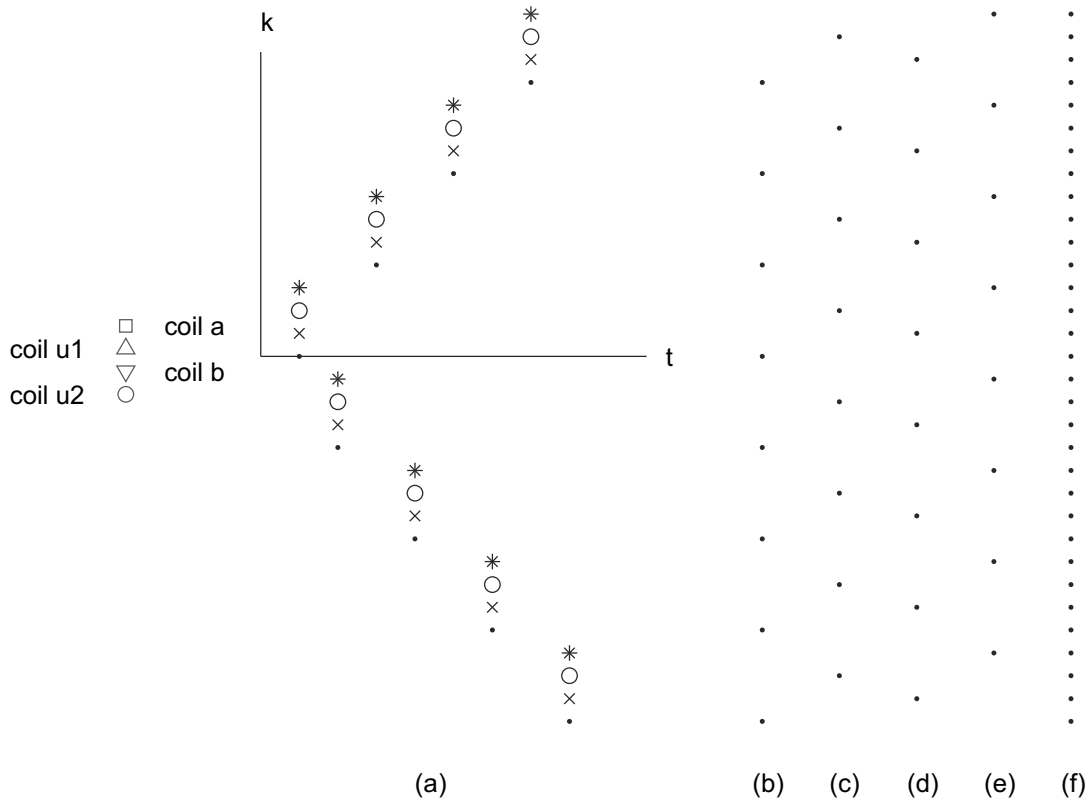

Figure B.3: Acquired k-space points when two fields are used for transmission and four fields are used for reception, in order to increase the FOV. **a:** Coil a is used to start the sequence, asterisk-marker: reception using coil u_2, circle-marker: reception using coil b, triangle-marker: reception using coil u_1, dot-marker: reception using coil a. **b-e:** The k-space points acquired in (a) using coils a, b, u_1, u_2, respectively, demonstrated in a vertically aligned fashion. **f:** All k-space points obtained in (b)-(e).

to the samples in Fig. B.4(e)-(f)). Such an approach increases the extent of the obtained k-space, hence increase the resolution in the image without any increase in the total experiment duration.

In some applications, all the k-space samples may not be obtained in a single run due to spin relaxation effects. In this case, the use of a third field with a specifically designed phase distribution can be used for starting the second run from the next point that was to be acquired in the first run. If a sequence that

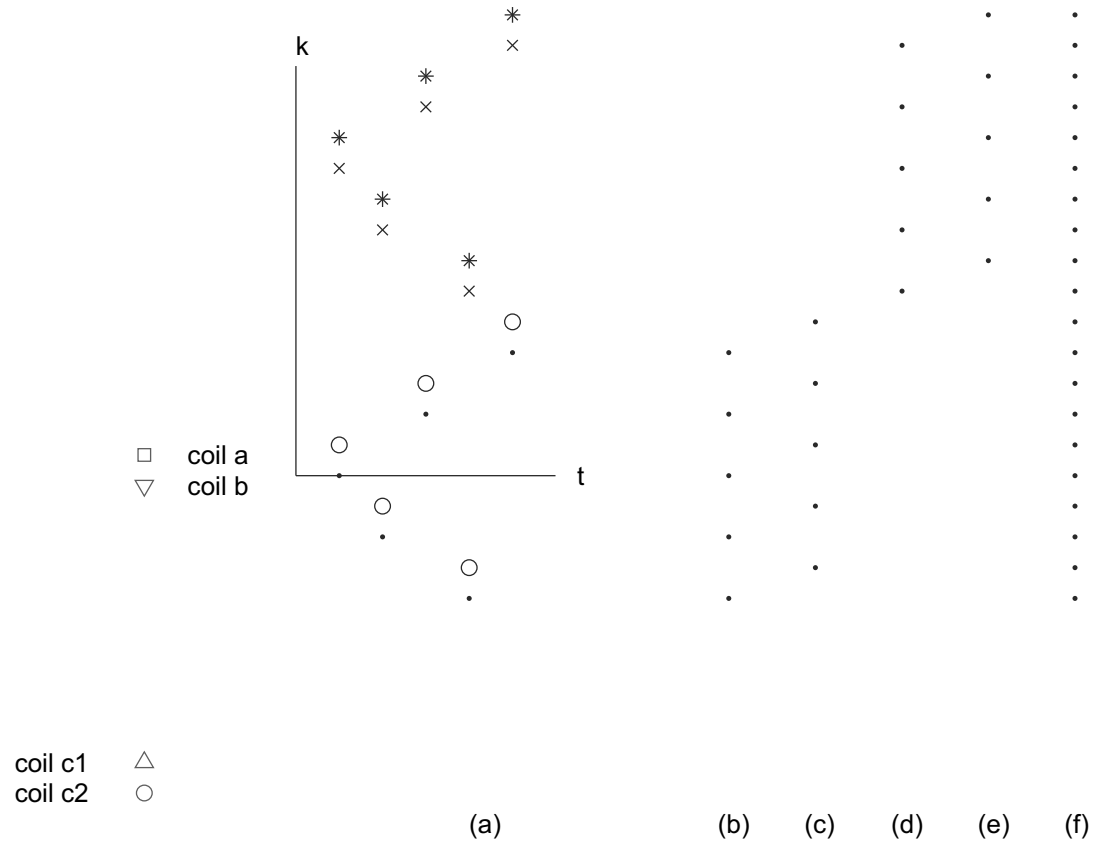

Figure B.4: Acquired k-space points when two fields are used for transmission and four fields are used for reception, in order to increase the resolution. **a:** Coil a is used to start the sequence, asterisk-marker: reception using coil c_2, cross-marker: reception using coil c_1, circle-marker: reception using coil b, dot-marker: reception using coil a. **b-e:** The k-space points acquired in (a) using coils a, b, c_1, c_2, respectively, demonstrated in a vertically aligned fashion. **f:** All k-space points obtained in (b)-(e).

starts with field a and that has "$n-1$" 180° pulses is applied in the first run, then the phase gradient of field c should be $k_\phi^c = (-1)^n \left[(n+1)k_\phi^a - nk_\phi^b\right]$. When the second run starts with field c and continues with the last field at the previous run, the next points in the k-space can be obtained, as shown in Fig. B.5(c). In Fig. B.5(a), the points marked with asterisks show the second run. Such applications enable getting data from farther regions of the k-space, allowing higher resolution in the image.

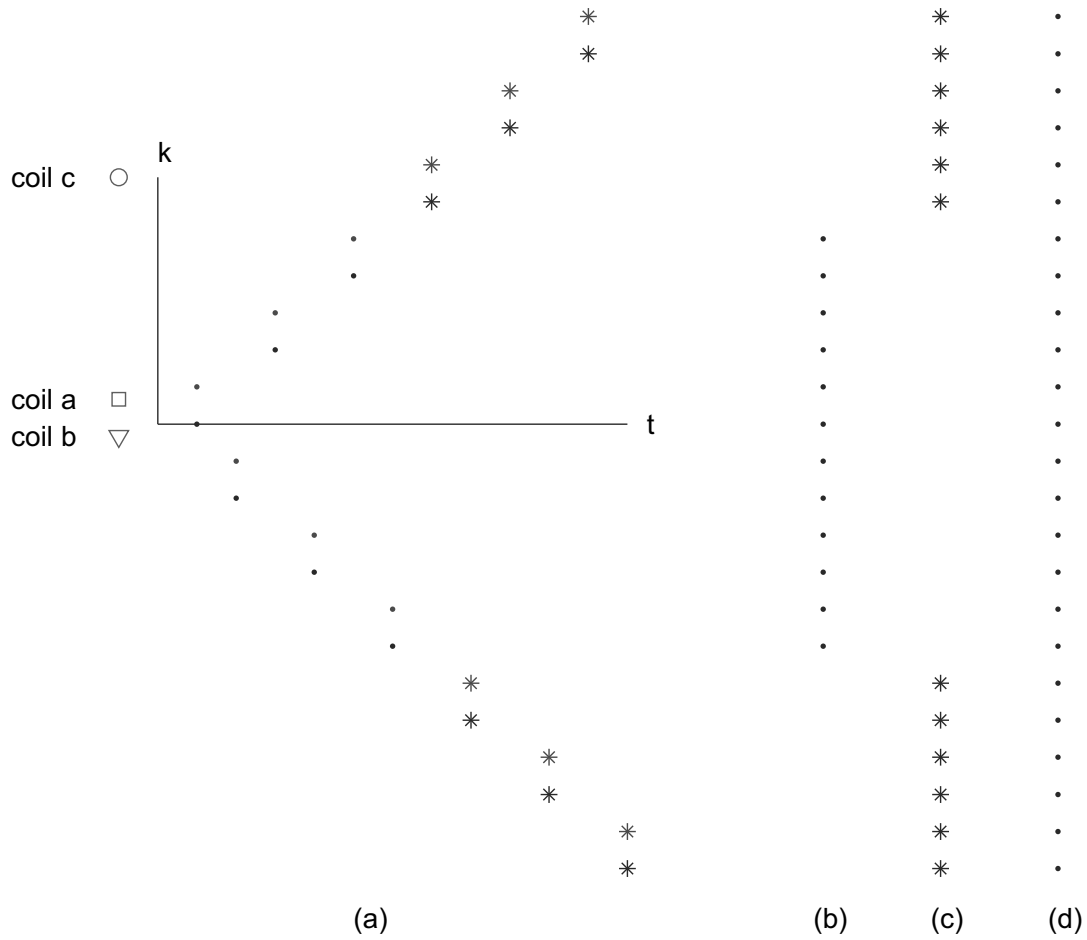

Figure B.5: Acquired k-space points when three fields are used for transmission and two fields are used for reception, in order to increase the resolution. **a:** In the first run, coil a is used to start the sequence, dot-markers: reception using coils a and b. In the second run, coil c is used to start the sequence, asterisk-markers: reception using coils a and b. **b:** The k-space points acquired during the first run of the sequence in (a), demonstrated in a vertically aligned fashion. **c:** The k-space points acquired during the second run of the sequence in (a), demonstrated in a vertically aligned fashion. **d:** All k-space points obtained in (b)-(c).

When a third transmit field c with a phase gradient $k_\phi^c = (k_\phi^a + k_\phi^b)$ is used in addition to the fields a and b, and when only the fields a and b are used as receive fields, the sampling rate in the k-space can be increased by applying the first sequence in the order "$a-b-a-b-a-$..." and the second sequence in the

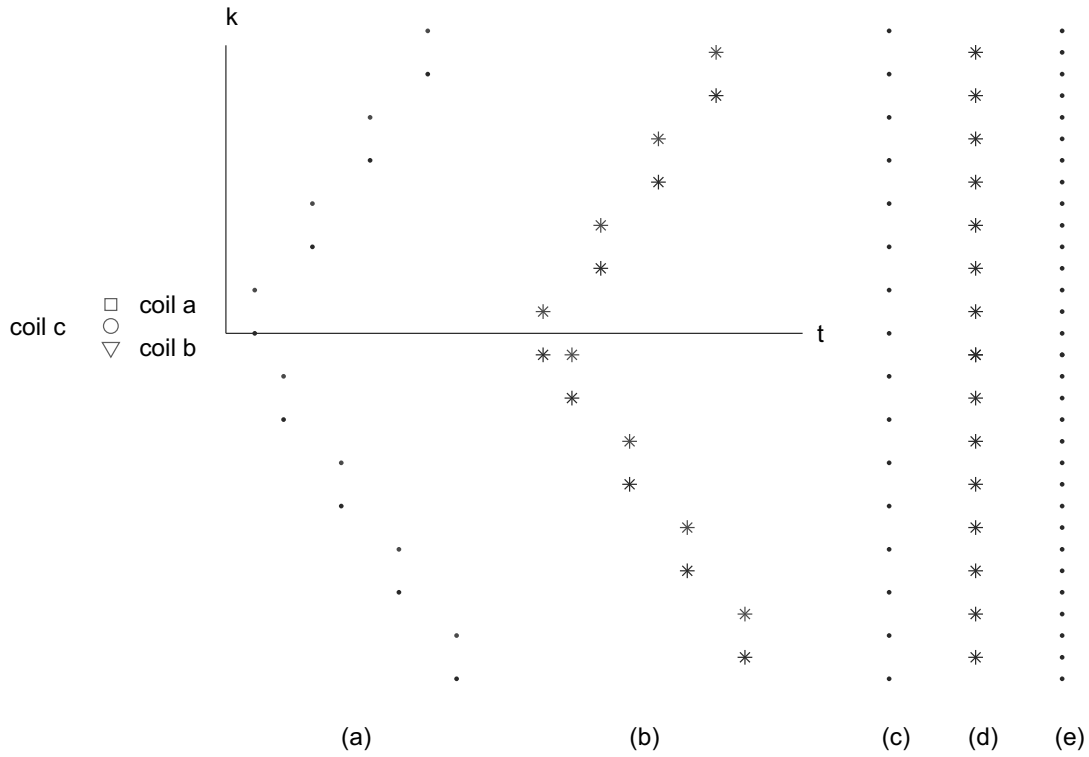

Figure B.6: Acquired k-space points when three fields are used for transmission and two fields are used for reception, in order to increase the FOV. **a:** In the first run, coil a is used to start the sequence, dot-markers: reception using coils a and b. **b:** In the second run, coil c is used to start the sequence, asterisk-markers: reception using coils a and b. **c:** The k-space points acquired in (a), demonstrated in a vertically aligned fashion. **d:** The k-space points acquired in (b), demonstrated in a vertically aligned fashion. **e:** All k-space points obtained in (c)-(d).

order "$c-b-a-b-a-$...". In this case, the intermediate points can be obtained as given in Figs. 5.2(a)-(e). The points with asterisks indicate the second run. The sampling rate, hence the FOV will be doubled compared to the sequence given in Fig. 5.2.

Fig. B.7 demonstrate an excitation approach that employs four RF fields where fields c_1 and c_2 have the following phase gradients: $k_\phi^{c_1} = k_\phi^a - 2n(k_\phi^a - k_\phi^b)$; $k_\phi^{c_2} = k_\phi^b - 2n(k_\phi^a - k_\phi^b)$. Figs. B.7(a,c-d) show the k-space points acquired when fields a and b are used for excitation and reception, and "$n-1$" 180° pulses are applied after starting with field a. Figs. B.7(b,e-f) show the k-space points

acquired when fields c_1 and c_2 are used for excitation and fields a and b are used for reception, and "$n-1$" 180° pulses are applied in the order "$c_2 - c_1 - c_2 - c_1 -$..." after starting the sequence with field c_1. It should be noted that because $k_\phi^{c_1} - k_\phi^{c_2} = k_\phi^a - k_\phi^b$, the sampling rate is the same. If the phase gradients were $k_\phi^{c_1} = k_\phi^a - 2n(k_\phi^a - k_\phi^b)$ and $k_\phi^{c_2} = k_\phi^b - 2n(k_\phi^a - k_\phi^b)$, then the samples obtained in the second run will be in the higher portion of the k-space rather than in the lower portion $\big($similar to the samples in Fig. B.4(d)-(e)$\big)$. Alternatively, the second sequence can be run with fields a and b and fields c_1 and c_2 can be used for reception. Such applications increase the extent of the obtained k-space, hence increase the resolution in the image.

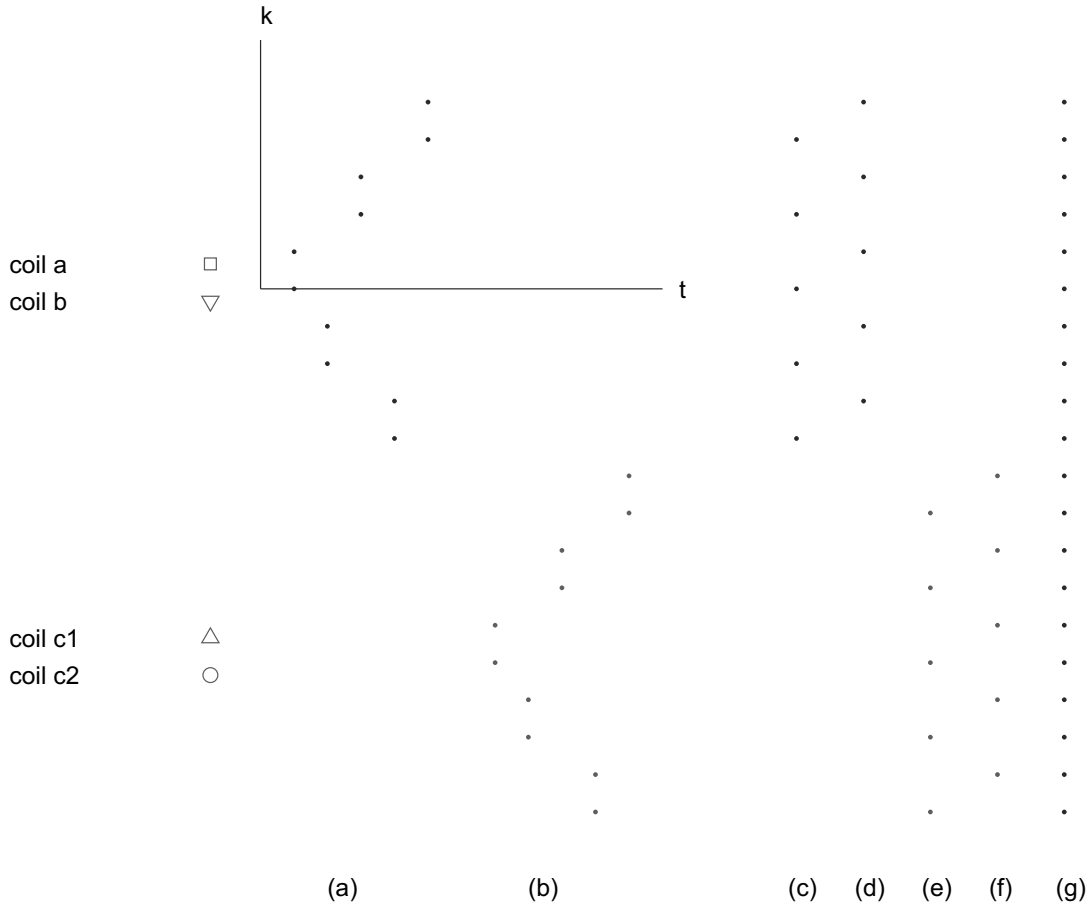

Figure B.7: Acquired k-space points when four fields are used for transmission and two fields are used for reception, in order to increase the resolution. **a:** In the first run, coil a is used to start the sequence, which is run in the order: "$a - b - a - b - a - \ldots$", dot-markers: reception using coils a and b. **b:** In the second run, coil c_1 is used to start the sequence, which is run in the order: "$c_1 - c_2 - c_1 - c_2 - c_1 - \ldots$", asterisk-markers: reception using coils a and b. **c-d:** The k-space points acquired in (a) using coils a, and b, respectively, demonstrated in a vertically aligned fashion. **e-f:** The k-space points acquired in (b) using coils a, and b, respectively, demonstrated in a vertically aligned fashion. **g:** All k-space points obtained in (c)-(f).

Bibliography

[1] S. Gabriel, R. W. Lau, and C. Gabriel, "The dielectric properties of biological tissues: II. Measurements in the frequency range 10 Hz to 20 GHz.," *Phys Med Biol*, vol. 41, pp. 2251–2269, 1996.

[2] W. A. Edelstein, G. H. Glover, C. J. Hardy, and R. W. Redington, "The intrinsic signal-to-noise ratio in NMR imaging.," *Magn Reson Med*, vol. 3, pp. 604–618, Aug 1986.

[3] O. Ocali and E. Atalar, "Ultimate intrinsic signal-to-noise ratio in MRI.," *Magn Reson Med*, vol. 39, pp. 462–473, Mar 1998.

[4] R. Lattanzi, A. K. Grant, M. A. Ohliger, and D. K. Sodickson, "Measuring practical coil array performance with respect to ultimate intrinsic SNR: a tool for array design and assessment.," in *Proc. Intl. Soc. Mag. Reson. Med. 14, Seattle, Washington, USA, p424*, 2006.

[5] H. Celik, Y. Eryaman, A. Altintas, I. A. Abdel-Hafez, and E. Atalar, "Evaluation of internal MRI coils using ultimate intrinsic SNR.," *Magn Reson Med*, vol. 52, pp. 640–649, Sep 2004.

[6] H. Vesselle and R. E. Collin, "The signal-to-noise ratio of nuclear magnetic resonance surface coils and application to a lossy dielectric cylinder model. I. Theory," vol. 42, no. 5, pp. 497–506, 1995.

[7] M. A. Ohliger, A. K. Grant, and D. K. Sodickson, "Ultimate intrinsic signal-to-noise ratio for parallel MRI: electromagnetic field considerations.," *Magn Reson Med*, vol. 50, pp. 1018–1030, Nov 2003.

[8] F. Wiesinger, N. de Zanche, and K. P. Pruessmann, "Approaching ultimate SNR with finite coil arrays," in *Proc. Intl. Soc. Mag. Reson. Med. 13, Miami Beach, Florida, USA, p672*, 2005.

[9] F. Wiesinger, P. Boesiger, and K. P. Pruessmann, "Electrodynamics and ultimate SNR in parallel MR imaging.," *Magn Reson Med*, vol. 52, pp. 376–390, Aug 2004.

[10] W. Schnell, W. Renz, M. Vester, and H. Ermert, "Ultimate signal-to-noise-ratio of surface and body antennas for magnetic resonance imaging," vol. 48, no. 3, pp. 418–428, 2000.

[11] R. Lattanzi, A. K. Grant, and D. K. Sodickson, "Approaching ultimate SNR and ideal current patterns with finite surface coil arrays on a dielectric cylinder.," in *Proc. Intl. Soc. Mag. Reson. Med. 16, Toronto, Ontario, Canada, p1074*, 2008.

[12] R. Lattanzi and D. K. Sodickson, "Dyadic Greens functions for electrodynamic calculations of ideal current patterns for optimal SNR and SAR.," in *Proc. Intl. Soc. Mag. Reson. Med. 16, Toronto, Ontario, Canada, p78*, 2008.

[13] R. Lattanzi, A. K. Grant, J. R. Polimeni, M. A. Ohliger, G. C. Wiggins, L. L. Wald, and D. K. Sodickson, "Performance evaluation of a 32-element head array with respect to the ultimate intrinsic SNR.," *NMR Biomed*, vol. 23, pp. 142–151, Feb 2010.

[14] J. Wang, A. Reykowski, and J. Dickas, "Calculation of the signal-to-noise ratio for simple surface coils and arrays of coils [magnetic resonance imaging]," vol. 42, no. 9, pp. 908–917, 1995.

[15] D. I. Hoult and P. C. Lauterbur, "The sensitivity of the zeugmatographic experiment involving human samples.," *J Magn Reson*, vol. 34, pp. 425–433, 1979.

[16] A. Reykowski and S. M. Wright, "The SNR of the idealized birdcage resonators and the SNR limit for infinite cylinder arrays.," in *Proc. Intl. Soc. Mag. Reson. Med. 3, Nice, France, p974*, 1995.

[17] A. Reykowski, *Theory and design of synthesis array coils for magnetic resonance imaging.* PhD thesis, Texas A&M University, 1996.

[18] "Guidance for the Submission Of Premarket Notifications for Magnetic Resonance Diagnostic Devices," tech. rep., Food and Drug Administration, 1998.

[19] I. E. Commission, "Medical electrical equipment. Part 2. Particular requirements for the safety of magnetic resonance equipment for medical diagnosis," *International Standard*, vol. 60601, pp. 2–33, 2002.

[20] D. Yang, M. C. Converse, D. M. Mahvi, and J. G. Webster, "Expanding the bioheat equation to include tissue internal water evaporation during heating.," *IEEE Trans Biomed Eng*, vol. 54, pp. 1382–1388, Aug 2007.

[21] R. Lattanzi, D. K. Sodickson, A. K. Grant, and Y. Zhu, "Electrodynamic constraints on homogeneity and radiofrequency power deposition in multiple coil excitations.," *Magn Reson Med*, vol. 61, pp. 315–334, Feb 2009.

[22] Y. Eryaman, C. A. Tunc, and E. Atalar, "Minimum SAR for RF shimming by allowing spatial phase variation.," in *Proc. Intl. Soc. Mag. Reson. Med. 17, Honolulu, Hawaii, USA, p4777*, 2009.

[23] J. Pauly, D. Nishimura, and A. Macovski, "A k-space analysis of small-tip-angle excitation," *J Magn Reson*, vol. 81, pp. 43–56, Dec 1989.

[24] J. Pauly, D. Nishimura, and A. Macovski, "A Linear Class of Large-Tip-Angle Selective Excitation Pulses," *J Magn Reson*, vol. 82, pp. 571–587, 1989.

[25] G. J. Metzger, C. Snyder, C. Akgun, T. Vaughan, K. Ugurbil, and P.-F. V. de Moortele, "Local B1+ shimming for prostate imaging with transceiver arrays at 7T based on subject-dependent transmit phase measurements.," *Magn Reson Med*, vol. 59, pp. 396–409, Feb 2008.

[26] B. A. Poser, P. J. Koopmans, T. Witzel, L. L. Wald, and M. Barth, "Three dimensional echo-planar imaging at 7 Tesla.," *Neuroimage*, vol. 51, pp. 261–266, May 2010.

[27] A. C. Zelinski, L. L. Wald, K. Setsompop, V. K. Goyal, and E. Adalsteinsson, "Sparsity-enforced slice-selective MRI RF excitation pulse design.," *IEEE Trans Med Imaging*, vol. 27, pp. 1213–1229, Sep 2008.

[28] A. C. Zelinski, L. L. Wald, K. Setsompop, V. Alagappan, B. A. Gagoski, V. K. Goyal, and E. Adalsteinsson, "Fast slice-selective radio-frequency excitation pulses for mitigating B+1 inhomogeneity in the human brain at 7 Tesla.," *Magn Reson Med*, vol. 59, pp. 1355–1364, Jun 2008.

[29] K. Setsompop, V. Alagappan, B. Gagoski, T. Witzel, J. Polimeni, A. Potthast, F. Hebrank, U. Fontius, F. Schmitt, L. L. Wald, and E. Adalsteinsson, "Slice-selective RF pulses for in vivo B1+ inhomogeneity mitigation at 7 tesla using parallel RF excitation with a 16-element coil.," *Magn Reson Med*, vol. 60, pp. 1422–1432, Dec 2008.

[30] C. Yang, W. Deng, V. Alagappan, L. L. Wald, and V. A. Stenger, "Four-dimensional spectral-spatial RF pulses for simultaneous correction of B1+ inhomogeneity and susceptibility artifacts in T2*-weighted MRI.," *Magn Reson Med*, vol. 64, pp. 1–8, Jul 2010.

[31] S. Conolly, D. Nishimura, A. Macovski, and G. Glover, "Variable-Rate Selective Excitation," *J Magn Reson*, vol. 78, pp. 440–458, JUL 1988.

[32] M. Bernstein, K. F. King, and X. J. Zhou, *Handbook of MRI Pulse Sequences*. Elsevier Academic Press, 2004.

[33] P. A. Bottomley and C. J. Hardy, "Two-dimensional spatially selective spin inversion and spin-echo refocusing with a single nuclear magnetic resonance pulse," *J Appl Phys*, vol. 62, pp. 4284–4290, 1987.

[34] S. Y. Lee and Z. H. Cho, "Localized volume selection technique using an additional radial gradient coil.," *Magn Reson Med*, vol. 12, pp. 56–63, Oct 1989.

[35] C. H. Oh, S. K. Hilal, Z. H. Cho, and I. K. Mun, "New spatial localization method using pulsed high-order field gradients (SHOT: Selection with High-Order gradienT).," *Magn Reson Med*, vol. 18, pp. 63–70, Mar 1991.

[36] E. X. Wu, G. Johnson, S. K. Hilal, and Z. H. Cho, "A new 3D localization technique using quadratic field gradients.," *Magn Reson Med*, vol. 32, pp. 242–245, Aug 1994.

[37] D. G. Wiesler, H. Wen, S. D. Wolff, and R. S. Balaban, "Reduction of field of view in MRI using a surface-spoiling local gradient insert.," *J Magn Reson Imaging*, vol. 8, no. 4, pp. 981–988, 1998.

[38] J. Hennig, A. M. Welz, G. Schultz, J. Korvink, Z. Liu, O. Speck, and M. Zaitsev, "Parallel imaging in non-bijective, curvilinear magnetic field gradients: a concept study.," *MAGMA*, vol. 21, pp. 5–14, Mar 2008.

[39] G. Schultz, P. Ullmann, H. Lehr, A. M. Welz, J. Hennig, and M. Zaitsev, "Reconstruction of MRI data encoded with arbitrarily shaped, curvilinear, nonbijective magnetic fields.," *Magn Reson Med*, vol. 64, pp. 1390–1403, Nov 2010.

[40] D. Gallichan, C. A. Cocosco, A. Dewdney, G. Schultz, A. Welz, J. Hennig, and M. Zaitsev, "Simultaneously driven linear and nonlinear spatial encoding fields in MRI.," *Magn Reson Med*, vol. 65, pp. 702–714, Mar 2011.

[41] M. Haas, P. Ullmann, J. T. Schneider, W. Ruhm, J. Hennig, and M. Zaitsev, "Large Tip Angle Parallel Excitation Using Nonlinear Non-Bijective PatLoc Encoding Fields," in *Proc. Intl. Soc. Mag. Reson. Med. 18, Stockholm, Sweden, p4929*, 2010.

[42] J. P. Stockmann, P. A. Ciris, G. Galiana, L. Tam, and R. T. Constable, "O-space imaging: Highly efficient parallel imaging using second-order nonlinear fields as encoding gradients with no phase encoding.," *Magn Reson Med*, vol. 64, pp. 447–456, Aug 2010.

[43] A. A. Maudsley, "Fourier imaging using RF phase encoding.," *Magn Reson Med*, vol. 3, pp. 768–777, Oct 1986.

[44] E. Atalar and O. Ocali, "Method of magnetic resonance analysis employing cylindrical coordinates and an associated apparatus," 2000.

[45] E. Kopanoglu, V. Erturk, and E. Atalar, "A Closed-Form Expression for Ultimate Intrinsic Signal-to-Noise Ratio in MRI," in *Proc. Intl. Soc. Mag. Reson. Med. 19, Honolulu, HI, USA, p2975*, 2009.

[46] E. Kopanoglu, V. Erturk, and E. Atalar, "A closed form expression for radial dependence of the ultimate intrinsic signal-to-noise ratio in MRI," in *Proc. Eur. Soc. Magn. Reson. Med. Biol. 26, Antalya, Turkey, p481*, 2009.

[47] E. Kopanoglu, V. B. Erturk, and E. Atalar, "Analytic expressions for the ultimate intrinsic signal-to-noise ratio and ultimate intrinsic specific absorption rate in MRI.," *Magn Reson Med*, vol. 66, pp. 846–858, Sep 2011.

[48] J. L. Prince and J. M. Links, *Medical imaging signals and systems*. Pearson Prentice Hall, 2006.

[49] O. M. Mueller, "Unconditionally stable ultra low noise RF preamplifier," 1989.

[50] H. C. Seton, J. M. S. Hutchison, and D. M. Bussell, "A 4.2 K receiver coil and SQUID amplifier used to improve the SNR of low-field magnetic resonance images of the human arm," *Meas Sci Tech*, vol. 8, pp. 198–207, 1997.

[51] A. C. Wright, H. K. Song, and F. W. Wehrli, "In vivo MR micro imaging with conventional radiofrequency coils cooled to 77 degrees K.," *Magn Reson Med*, vol. 43, pp. 163–169, Feb 2000.

[52] R. D. Black, T. A. Early, P. B. Roemer, O. M. Mueller, A. Mogro-Campero, L. G. Turner, and G. A. Johnson, "A high-temperature superconducting receiver for nuclear magnetic resonance microscopy.," *Science*, vol. 259, pp. 793–795, Feb 1993.

[53] D. I. Hoult and R. E. Richards, "The signal-to-noise ratio of the nuclear magnetic resonance experiment.," *J Magn Reson*, vol. 24, pp. 71–85, Dec 1976.

[54] D. I. Hoult, "The principle of reciprocity in signal strength calculations - a mathematical guide," *Concepts Magn Reson*, vol. 12, pp. 173–187, 2000.

[55] H. Celik, A. Uluturk, T. Tali, and E. Atalar, "A catheter tracking method using reverse polarization for MR-guided interventions.," *Magn Reson Med*, vol. 58, pp. 1224–1231, Dec 2007.

[56] S. M. Wright and L. L. Wald, "Theory and application of array coils in MR spectroscopy.," *NMR Biomed*, vol. 10, pp. 394–410, Dec 1997.

[57] D. K. Cheng, *Fundamentals of Engineering Electromagnetics.* Pearson Addison Wesley, 1993.

[58] C. A. Balanis, *Antenna Theory and Design.* Wiley, 2005.

[59] S. A. Schelkunoff, *Electromagnetic Waves.* Bell Telephone Labs Series, 1943.

[60] D. M. Pozar, *Microwave engineering.* Wiley, 2005.

[61] G. B. J. Thomas and R. L. Finney, *Calculus and analytic geometry.* Addison Wesley, 1998.

[62] L. A. Geddes and L. E. Baker, "The specific resistance of biological material–a compendium of data for the biomedical engineer and physiologist.," *Med Biol Eng*, vol. 5, pp. 271–293, May 1967.

[63] A. Macovski, "Noise in MRI.," *Magn Reson Med*, vol. 36, pp. 494–497, Sep 1996.

[64] E. Kopanoglu, B. Akin, V. Erturk, and E. Atalar, "SAR Reduction using Nonlinear Gradients," in *Proc. Intl. Soc. Mag. Reson. Med. 19, Montreal, Canada, p1848*, 2011.

[65] E. Kopanoglu, Y. Gokhalk, U. Yilmaz, V. Acikel, and E. Atalar, "Decreasing SAR of a multi-dimensional central brightening inhomogeneity correction pulse using nonlinear gradient fields and VERSE," in *Proc. Intl. Soc. Mag. Reson. Med. 20, Melbourne, Australia, p3470*, 2012.

[66] E. Kopanoglu, V. Erturk, and E. Atalar, "Reducing SAR using nonlinear gradient fields: application to B1 inhomogeneity correction with multi-dimensional excitation pulses," in *Proc. Eur. Soc. Magn. Reson. Med. Biol. 28, Leipzig, Germany, p54*, 2011.

[67] E. Kopanoglu, U. Yilmaz, Y. Gokhalk, V. Acikel, and E. Atalar, "Dogrusal olmayan gradyan manyetik alanlar kullanilarak cok boyutlu uyari sinyallerinin Ozgul Sogurum Hizinin dusurulmesi," in *Turk Manyetik Rezonans Dernegi 17nci Yillik Toplantisi, Ankara, Turkey*, 2012.

[68] E. Kopanoglu, U. Yilmaz, Y. Gokhalk, and E. Atalar, "SAR Reduction using Nonlinear Gradient Fields," *Magn Reson Med*, in production.

[69] P. A. Bottomley, H. C. Charles, P. B. Roemer, D. Flamig, H. Engeseth, W. A. Edelstein, and O. M. Mueller, "Human in vivo phosphate metabolite imaging with 31P NMR.," *Magn Reson Med*, vol. 7, pp. 319–336, Jul 1988.

[70] B. J. Wilm, C. Barmet, M. Pavan, and K. P. Pruessmann, "Higher order reconstruction for MRI in the presence of spatiotemporal field perturbations.," *Magn Reson Med*, vol. 65, pp. 1690–1701, Jun 2011.

[71] J. T. Schneider, M. Haas, W. Ruhm, J. Hennig, and P. Ullmann, "Robust spatially selective excitation using radiofrequency pulses adapted to the effective spatially encoding magnetic fields.," *Magn Reson Med*, vol. 65, pp. 409–421, 2011.

[72] H. Weber, D. Gallichan, G. Schultz, W. R. Witschey, A. M. Welz, C. A. Cocosco, J. Hennig, and M. Zaitsev, "ExLoc: Excitation and Encoding of Curved Slices," in *Proc. Intl. Soc. Mag. Reson. Med. 19, Montreal, Canada, p2806*, 2011.

[73] K. I. Marro, D. Lee, and O. M. Hyyti, "Nonlinear magnetic field gradients can reduce SAR in flow-driven arterial spin labeling measurements.," *J Magn Reson*, vol. 185, pp. 94–102, Mar 2007.

[74] R. Turner, "A target field approach to optimal coil design," *J Phys D: Appl Phys*, vol. 19, pp. 147–151, 1986.

[75] R. Bowtell and P. Mansfield, "Gradient coil design using active magnetic screening.," *Magn Reson Med*, vol. 17, pp. 15–9; discussion 19–21, Jan 1991.

[76] C. A. Cocosco, D. Gallichan, A. J. Dewdney, G. Schultz, A. M. Welz, W. R. Witschey, H. Weber, J. Hennig, and M. Zaitsev, "First In-vivo Results with

a PatLoc Gradient Insert Coil for Human Head Imaging," in *Proc. Intl. Soc. Mag. Reson. Med. 18, Stockholm, Sweden, p4929*, 2010.

[77] E. Kopanoglu, U. Yilmaz, B. Akin, V. Acikel, and E. Atalar, "Localizing the excitation to reduce scan time using nonlinear gradient fields," in *Proc. Intl. Soc. Mag. Reson. Med. 20, Melbourne, Australia, p3471*, 2012.

[78] E. Kopanoglu, U. Yilmaz, B. Akin, V. Acikel, and E. Atalar, "Manyetik rezonansla goruntulemede dogrusal olmayan gradyan manyetik alanlar kullanilarak goruntuleme suresinin dusurulmesi," in *Turk Manyetik Rezonans Dernegi 17nci Yillik Toplantisi, Ankara, Turkey*, 2012.

[79] A. Buecker, G. Adam, J. M. Neuerburg, A. Glowinski, J. J. van Vaals, and R. W. Guenther, "MR-guided biopsy using a T2-weighted single-shot zoom imaging sequence (Local Look technique).," *J Magn Reson Imaging*, vol. 8, no. 4, pp. 955–959, 1998.

[80] C. Juchem, T. W. Nixon, S. McIntyre, D. L. Rothman, and R. A. de Graaf, "Magnetic field modeling with a set of individual localized coils.," *J Magn Reson*, vol. 204, pp. 281–289, Jun 2010.

[81] E. Kopanoglu, A. F. Yilmaz, T. Demir, V. Erturk, and E. Atalar, "A New Class of Encoding Techniques using a Transmit Array: Illustration with Cylindrical Encoding," in *Proc. Intl. Soc. Mag. Reson. Med. 18, Stockholm, Sweden, p4912*, 2010.

[82] S. King, D. Yin, S. Thingvold, J. Sharp, and B. Tomanek, "Transmit Array Spatial Encoding (TRASE): A New Data Acquisition Method in MRI," in *Proc. Intl. Soc. Mag. Reson. Med. 14, Seattle, WA, USA, p2628*, 2006.

[83] J. Sharp, S. King, D. Yin, V. Volotovskyy, and B. Tomanek, "High Resolution 2D Imaging without Gradients with Accelerated TRASE," in *Proc. Intl. Soc. Mag. Reson. Med. 16, Toronto, Ontario, Canada, p829*, 2008.

[84] S. King, P. Latta, V. Volotovskyy, J. Sharp, and B. Tomanek, "Phase Encoding without Gradients at High Field: TRASE RF MRI at 3T," in *Proc. Intl. Soc. Mag. Reson. Med. 17, Honolulu, HI, USA, p2673*, 2009.

[85] J. C. Sharp and S. B. King, "MRI using radiofrequency magnetic field phase gradients.," *Magn Reson Med*, vol. 63, pp. 151–161, Jan 2010.

[86] K. P. Pruessmann, M. Weiger, M. B. Scheidegger, and P. Boesiger, "SENSE: sensitivity encoding for fast MRI.," *Magn Reson Med*, vol. 42, pp. 952–962, Nov 1999.

[87] D. K. Sodickson and W. J. Manning, "Simultaneous acquisition of spatial harmonics (SMASH): fast imaging with radiofrequency coil arrays.," *Magn Reson Med*, vol. 38, pp. 591–603, Oct 1997.

[88] C. J. Hardy, W. A. Edelstein, and D. Vatis, "Efficient Adiabatic Fast Passage for NMR Population Inversion in the Presence of Radiofrequency Field Inhomogeneity and Frequency Offsets," *J Magn Reson*, vol. 66, pp. 470–482, 1986.

[89] R. S. Staewen, A. J. Johnson, B. D. Ross, T. Parrish, H. Merkle, and M. Garwood, "3-D FLASH imaging using a single surface coil and a new adiabatic pulse, BIR-4.," *Invest Radiol*, vol. 25, pp. 559–567, May 1990.

[90] N. W. McLachlan, *Bessel functions for engineers.* The Clarendon Press, 1955.